



저작자표시-비영리-동일조건변경허락 2.0 대한민국

이용자는 아래의 조건을 따르는 경우에 한하여 자유롭게

- 이 저작물을 복제, 배포, 전송, 전시, 공연 및 방송할 수 있습니다.
- 이차적 저작물을 작성할 수 있습니다.

다음과 같은 조건을 따라야 합니다:



저작자표시. 귀하는 원저작자를 표시하여야 합니다.



비영리. 귀하는 이 저작물을 영리 목적으로 이용할 수 없습니다.



동일조건변경허락. 귀하가 이 저작물을 개작, 변형 또는 가공했을 경우에는, 이 저작물과 동일한 이용허락조건하에서만 배포할 수 있습니다.

- 귀하는, 이 저작물의 재이용이나 배포의 경우, 이 저작물에 적용된 이용허락조건을 명확하게 나타내어야 합니다.
- 저작권자로부터 별도의 허가를 받으면 이러한 조건들은 적용되지 않습니다.

저작권법에 따른 이용자의 권리는 위의 내용에 의하여 영향을 받지 않습니다.

이것은 [이용허락규약\(Legal Code\)](#)을 이해하기 쉽게 요약한 것입니다.

[Disclaimer](#)

공학박사학위논문

**Fabrication and Rheological Analysis of
Microfluidic Systems with Nanostructured
Surfaces**

나노구조 미세유체 시스템의 제작과
유변학적 해석

서울대학교 대학원

재료공학부

이 두 진

Fabrication and Rheological Analysis of Microfluidic
Systems with Nanostructured Surfaces

나노구조 미세유체 시스템의 제작과 유변학적 해석

지도교수 윤 재 룬

이 논문을 공학박사 학위논문으로 제출함
2012년 12월

서울대학교 대학원

재료공학부

이 두 진

이 두 진의 공학박사 학위논문을 인준함
2012년 12월

위원장	_____	인
부위원장	_____	인
위원	_____	인
위원	_____	인
위원	_____	인

**Fabrication and Rheological Analysis of
Microfluidic Systems with Nanostructured
Surfaces**

Advisor : Jae Ryoun Youn

by

Doo Jin Lee

2013

School of Materials Science and Engineering

Graduate School

Seoul National University

Abstract

We explored a liquid slip, referred to as the Navier slip, at liquid-solid interface. While the liquid slip has been observed experimentally at micro and nanoscale, its fundamental mechanism is still controversial and has yet to be fully understood. In general, it is known that liquid molecules are capable of slipping at liquid-solid interface when the liquid possesses a low wettability due to superhydrophobicity, thus resulting in drag reduction. This is the so called Navier slip for a Newtonian liquid.

Such a slip is provoked by the physicochemical features of the liquid-solid system. The goal of this study was to investigate the effect of a nanoengineered surface structure on liquid slip by fabricating the self-assembly structure of nano Zinc Oxide (*n-ZnO*). We have also examined how the liquid-solid surface interaction controlled by hydrophobic chemical treatment affects the liquid slip. The findings showed that liquid slip increases with decreasing the characteristic length scales (e.g., channel height and depth), resulting in drag reduction. It was also found that dewetted (Cassie) state due to the generation of air gap developed by *n-ZnO* was more critical for the liquid slip than the minimization of interface interaction. The linear and non-linear Navier slip models showed that liquid slip behavior is more obvious when increasing the non-linearity. This study will contribute to understanding of the underlying physics behind fluid slip phenomena, such as the Navier slip for Newtonian liquids and Maxwell's slip for Newtonian gases.

In chapter 2, superhydrophobicity of multi-scale hierarchical structures and bouncing phenomenon of a water droplet on the superhydrophobic surface were studied. Superhydrophobicity is a unique characteristic of surface structure provoking extreme water repellency and a contact angle (CA) over 150°. For these reasons many researchers have produced biomimetic superhydrophobic surfaces with extremely high water repellency for industrial applications such as self-cleaning windows, windshield, exterior paints, antifouling, roof tiles, and textiles. Theoretically, the surface roughness

morphology of multi-scale nanostructures is desired not only to maximize CA but also to minimize the free energy barrier. Additionally, it guarantees the superhydrophobic state more stable and thus incurs larger self-cleaning effect, higher dynamic bouncing behavior, lower CAH, and smaller sliding angle. The dynamic bouncing effect is determined by the droplet velocity, surface roughness, and liquid properties. Compared with references related to the CA, a limited number of studies on the bouncing effect were reported so far. Therefore, the present study is meaningful to investigate physical insight for the bouncing phenomenon. To do this, the multi-scale hierarchical structures of carbon nanotube/ZnO and ZnO/carbon nanofiber were produced by the hydrothermal method. The multi-scale hierarchical structure showed superhydrophobicity with a static contact angle (CA) larger than 160° due to increased air pockets in the Cassie-Baxter state. Water bouncing effect observed on the multi-scale hierarchical nanostructure was explained by the free energy barrier (FEB) analysis and finite element simulation. The multi-scale hierarchical nanostructure showed low FEBs which provoke high CA and bouncing phenomenon due to small energy dissipation towards receding and advancing directions.

In chapter 3, we investigated a novel concept for the separation of particles using the incorporation of elasto-inertial effect and dean effect termed as “Dean-coupled Elasto-inertial effect”. Under laminar flow regime, when viscoelastic fluid is used as a medium particles experience the “Elasto-inertial force” and are focused at the center. In this study an additional secondary force caused by a curved geometry, the dean drag force, is exerted on the particles and the concept of “Dean-coupled Elasto-inertial force” is proposed. Theoretical analysis indicates that a particle focusing band with respect to channel aspect ratios exists due to the two main forces. It is revealed that the competition of the dean drag force and the elastic force affects the lateral displacement of suspended particles depending on the particle sizes. The elastic force is induced by the nature of a viscoelastic medium and the dean drag force is contributed by the curved channel geometry. The cooperation of the two forces produces an extraordinary particle focusing region. Numerical analysis of viscoelastic fluid was employed in order to explain theoretical background and a mechanism for the

lateral migration which follows the relationship between the elastic and dean drag forces with respect to particle size. It was demonstrated that this platform is very promising to achieve the multiplex particle focusing at the equilibrium position of the particle which is determined by the incorporation of the rheological properties of the fluid and the channel geometry.

Keywords: liquid slip, nanostructure, cassie surface, superhydrophobic surface, superhydrophobicity, water bouncing, hierarchical nanostructures, thermodynamical analysis, droplet deformation, Particle focusing, microfluidics, inertial force, dean force, separation, viscoelastic fluid, particle migration, interfacial effect, finite element analysis

Student Number: 2009-30896

Contents

Abstract	i
List of Figures	ix
List of Tables	xiii
I. Introduction	1
1.1. Physics at the micrometric scale	1
1.1.1. Surface Wetting State	1
1.1.2. Liquid Slip and Superhydrophobicity	4
1.2. Microfluidic System	6
1.2.1. Fabrication technique	9
1.2.2. Particle dynamics in a microchannel	13
1.3. Objectives of Present Work	15
1.4. References	16
II. Liquid Slip Phenomenon on a Nanostructured Surface	19
2.1. Introduction	19
2.2. Theoretical Background	21
2.2.1. Analytical Prediction	21
2.2.2. Thermodynamical Approach	24
2.3. Experimental Section	27
2.3.1. Rheological Characterization	27
2.3.2. Self-assembly of Zinc Oxide	27
2.4. Results and Discussion	37
2.4.1. Determination of Surface Condition	37
2.4.2. Liquid Slip Phenomenon	38
2.5. Summary	47
2.6. Supplementary Information	49
2.7. References	53

III. Superhydrophobicity and Water Droplet Bouncing Phenomena on a Multi-scale Nanostructured Surface

3.1. Introduction	56
3.2. Theoretical Background	58
3.2.1. Thermodynamical Approach	58
3.2.2. Numerical Simulation	59
3.3. Experimental Section	60
3.3.1. Fabrication of CNT/Polymer Nanocomposites	60
3.3.2. Self-assembly of Single-scale Nanostructures	64
3.3.3. Self-assembly of Multi-scale Nanostructures	64
3.3.4. CA and CAH measurements	65
3.4. Results and Discussion	70
3.4.1. Superhydrophobicity on Various Structures	70
3.4.2. Water Droplet Bouncing Phenomenon	75
3.5. Summary	83
3.6. References	86

IV. Multiplex Particle Focusing Phenomenon via the Dean-coupled Elasto-inertial Effect of Viscoelastic Fluid

4.1. Introduction	90
4.2. Theoretical Background	92
4.2.1. Elasto-inertial Particle Focusing	92
4.2.2. Dean Flow Induced Particle Migration	94
4.2.3. Dean-coupled Elasto-inertial Particle Separation	96
4.3. Results and Discussion	103
4.3.1. 3D Simulation Results of Elastic and Dean Forces	103
4.3.2. Continuous Single-line Particle Focusing	108
4.3.3. Size-selective Multiplex Particle Focusing	114
4.3.4. Particle Migration with a Wall Slip System	122

4.4. Summary	127
4.5. References	127
V. Concluding Remarks	131
Korean Abstract	134

List of Figures

- Figure 1.1.** A classification of surface energy and surface structure.
- Figure 1.2.** Size characteristics of microfluidic devices.
- Figure 1.3.** A schematic representation of photolithography process: (a) coating photoresist, (b) photolithography, and (c) developing photoresist.
- Figure 1.4.** A schematic representation of soft lithography.
- Figure 2.1.** Schematic diagram of a parallel-disk rheometer with liquid wall slip at angular velocity.
- Figure 2.2.** normalized Free energy (FE) with contact angle of both Wenzel and Cassie surfaces.
- Figure 2.3.** Normalized Free energy barrier (FEB) with contact angle of Cassie surface.
- Figure 2.4.** Schematics of self-assembling method of Zinc Oxide on a glass substrate.
- Figure 2.5.** SEM image of n-ZnO nanostructured surface and magnified view of the n-ZnO hexagonal pillars.
- Figure 2.6.** Contact angle measurements at five positions on an n-ZnO nanostructured glass substrate. (a) Schematic representation of the glass substrate, (b) Contact angles of a sessile water droplet on the glass substrate before the self-assembly of Zinc Oxide, (c) Zinc oxide self-assembled glass substrate after 4 hours, and (d) 1 day.
- Figure 2.7.** Shear stress as a function of shear rate measured for different surfaces.
- Figure 2.8.** Dynamic viscosity measured by the steady shear experiment for various channel heights: (a) smooth surface, (b) hydrophobic surface, and (c) n-ZnO Cassie surface.
- Figure 2.9.** (a) Velocity profiles with the linear and non-linear Navier slip exponents. An inset graph shows a height dependence on slip velocity, (b) integral constant C_1 and slip length with the linear and non-linear Navier slip exponents.

- Figure 2.10.** (a) Dynamic viscosity and (b) wall slip length measured by the steady shear experiment at 40 μm channel height for smooth, hydrophobic, and n-ZnO Cassie surfaces.
- Figure 2.11.** Wall slip length measured with respect to the channel height for different surface features.
- Figure 2.12.** Schematics of Superhydrophobicity and liquid slip phenomena caused by the surface free energy.
- Figure 2.13.** Oscillatory data of storage modulus (G'), loss modulus (G''), and complex viscosity (n^*) in frequency sweep modes: (a) ~ (c) smooth surface, (d) ~ (f) hydrophobic surface, and (g) ~(i) n-ZnO Cassie surface.
- Figure 2.14.** Shear stress VS shear rate with respect to the channel height: (a) 500 μm , (b) 200 μm , (C) 80 μm , and (d) 60 μm .
- Figure 3.1.** Fabrication of CNT/Polymer nanocomposites. (a) pure PLA, (b) 1wt % filled composite, (c) 3wt % filled composite, and (d) a magnified view of (c).
- Figure 3.2.** Single-scale surface morphology of (a) CNF forest, (b) CNT forest, (c) ZnO nano-pillars, and (d) enlarged view of the ZnO nano-pillars.
- Figure 3.3.** Multi-scale hierarchical nanostructure: (a) ZnO/CNF hierarchical nanostructure showing superhydrophobicity with the contact angle of 162° , (b) enlarged view of the ZnO/CNF in which ZnO nano-pillars are successfully grown onto the CNF, (c) CNT/ZnO hierarchical nanostructure showing higher superhydrophobicity with the contact angle of 167.5° , and (d) enlarged view of the CNT/ZnO in which CNTs are well networked with ZnO.
- Figure 3.4.** (a) Schematic illustration of the multi-scale hierarchical system prepared in this study and (b) Schematic cross-sectional configuration of a liquid droplet on the system.
- Figure 3.5.** (a) Normalized Free Energy (FE) of the single-scale and dual-scale structures. The enlarged graphs show the variation in the local energy barriers indicating metastable and unstable regions. (b) Normalized

receding and advancing Free Energy Barriers (FEB) of the single-scale and dual-scale structures. The insets are the enlarged normalized free energy barriers (FEB).

Figure 3.6. Contact angle as a function of the ratio between micro-pillar size and nano-pillar size and the density of nano-pillars on the micro-pillar. The region between the two dashed lines represents ECAs obtainable in this system.

Figure 3.7. Normalized FEB as a function of system sizes; a:b:d = 80:200:1000 nm (1A and 1R), 40:100:500 nm (2A and 2R), 20:50:250 nm (3A and 3R), and 10:25:125 nm (4A and 4R). The shaded regions in the inset graph indicate the CAH index proposed in this study.

Figure 3.8. Simulation results of distinct dynamic phenomena of a water droplet with different velocity: (a) inlet velocity is 1.25 m/s and (b) inlet velocity is 2.5 m/s.

Figure 3.9. Experimental and simulation results of distinct dynamic phenomena of a water droplet: (a) sticking of the droplet on the CNF forest, (b) sticking of the droplet on the CNT forest, (c) simulation results of the sticking droplet with a CA of 120° , (d) bouncing of the droplet over the ZnO/CNF multi-scale hierarchical nanostructure, (e) bouncing of the droplet over the CNT/ZnO multi-scale hierarchical nanostructure, and (f) simulation results of the bouncing droplet with a CA of 165° .

Figure 3.10. Contact angle (CA), Contact angle Hysteresis (CAH), and sliding angle (α) of single-scale and dual-scale nanostructures before and after SAM treatment.

Figure 3.11. Schematics of Superhydrophobicity and water droplet bouncing phenomena caused by the surface free energy.

Figure 4.1. Dean flow and velocity profile with respect to channel aspect ratio in a curved spiral channel.

Figure 4.2. Schematic diagram of the “Dean-coupled Elasto-inertial focusing” proposed in this system.

Figure 4.3. The effect of dean drag force with respect to the Dean number in a curved

channel.

Figure 4.4. The first normal stress differences depending on the Weissenberg number in a square channel.

Figure 4.5. The distribution of the first normal stress difference with respect to the Weissenberg number along the horizontal direction in a square channel.

Figure 4.6. The first normal stress difference with respect to the Weissenberg number in a curved spiral channel.

Figure 4.7. The distribution of the first normal stress difference with respect to the Weissenberg number along the horizontal direction in a curved spiral channel.

Figure 4.8. A schematic representation of size-dependent particle migration due to the competition of the dean drag force and the elastic force.

Figure 4.9. Particle dynamics in both of the Newtonian and viscoelastic fluids. The snapshots show the tenth turn of the spiral channel with (a) 1.5 μm PS, (b) 5 μm PS, and (c) 10 μm PS.

Figure 4.10. Particle migration with respect to the Newtonian and viscoelastic fluids: (a) No focusing of the particles, (b) probability distribution function of 1 μm PS, (c) 10 μm PS in the Newtonian fluid. (d) Focusing of the particles, (e) probability distribution function of 1 μm PS, and (f) 10 μm PS in the viscoelastic fluid.

Figure 4.11. Size-selective multiplex particle focusing with the diameter of 1.5 μm and 10 μm Polystyrene particles: (a) parallel entrained particles at the bifurcation, (b) at an outlet, (c) at an upper outlet, (d) at a lower outlet, and (e) probability distribution function.

Figure 4.12. Focusing Band Ratio (FBR) with respect to the channel aspect ratio.

Figure 4.13. The behavior of particle migration with the diameter of 1.5 μm in the (a) Newtonian flow and (b) viscoelastic fluid.

Figure 4.14. The behavior of particle migration with the diameter of 5 μm in the (a) Newtonian flow and (b) viscoelastic fluid.

Figure 4.15. The behavior of particle migration with the diameter of 10 μm in the (a)

Newtonian flow and (b) viscoelastic fluid.

Figure 4.16. First normal stress difference and velocity field with estimated particle focusing regions under no-slip condition.

Figure 4.17. First normal stress difference and velocity field with estimated particle focusing regions under partial slip condition of $V_{slip} / V_{inlet} \sim 0.4$.

Figure 4.18. First normal stress difference and velocity field with estimated particle focusing regions under partial slip condition of $V_{slip} / V_{inlet} \sim 1$.

List of Tables

Table 2.1. Characteristics of a sessile water droplet on the glass substrate before the self-assembly of Zinc Oxide.

Table 2.2. Characteristics of a sessile water droplet on the Zinc oxide self-assembled glass substrate after 4 hours.

Table 2.3. Characteristics of a sessile water droplet on the Zinc oxide self-assembled glass substrate after 1 day.

I. Introduction

1.1. Physics at the micrometric scale

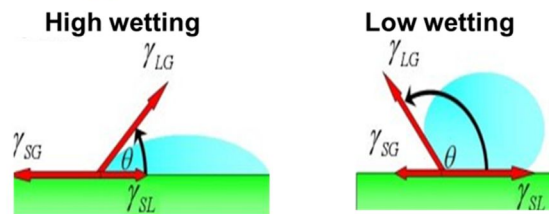
In our macroscopic world, we are accustomed to the omnipresence and the importance of gravitational force [1]. However, at micrometric scales gravitational force becomes negligible and surface forces such as capillarity, wetting, and adhesion become important resulting in surprising physical phenomena. Therefore, it is necessary to rationalize a counterintuitive world and to understand microsystems in order to know whether it will be advantageous to miniaturize. As systems are miniaturized, surface wetting and adhesion caused by surface energy become significant so that it is important to investigate physical phenomena that happen in the microscopic world not yet fully understood.

1.1.1. Surface Wetting State

Wetting is the ability of a liquid droplet to maintain contact with a solid surface, resulting from intermolecular interactions between them. It is well known that low surface energy and surface roughness can enhance contact angle and superhydrophobicity. Typically, solid surfaces show either high-energy or low-energy states which determine the wettability and contact angle. When a surface shows little wetting a liquid droplet on the surface has high contact angle. Surface structures are classified into three categories: Young state, Wenzel (wetting) state, and Cassie (dewetting) state (Figure. 1.1). The Young state refers to an ideal surface, but real surfaces do not have perfect smoothness like the ideal surface. The Wenzel state describes the homogeneous wetting in that a liquid penetrates into pillars on a solid surface. The Cassie state is dealing with a heterogeneous surface and a liquid does

not penetrate into the pillars. Typically, The Cassie state is more favored to show superhydrophobicity and liquid slip since the interface between liquid and solid consists of air and solid so that friction is decreased between them.

1. Surface energy



2. Surface structure

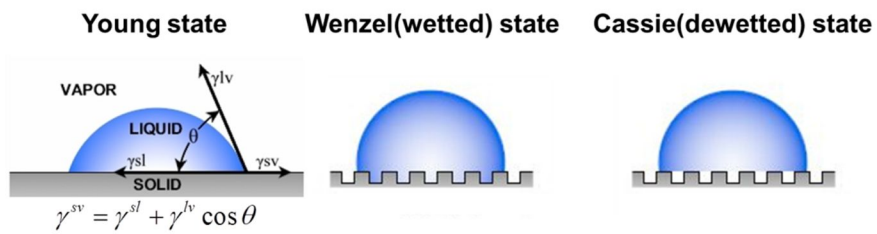


Figure 1.1. A classification of surface energy and surface structure.

1.1.2. Liquid Slip and Superhydrophobicity

At the macroscopic level, no-slip boundary condition is well accepted, i.e., the fluid velocity adjacent to the wall is the same with the velocity of the solid boundary [1]. While the no-slip boundary condition has been proven to be accurate for a number of macroscopic flows, it sometimes fails to prove experimental results especially in microscopic flows and concentrated suspensions. Recently, several researchers have suggested that the no-slip boundary condition is not suitable for the flow over hydrophobic boundaries, e.g., with hot-film anemometry apparent fluid slip at the wall of a strongly hydrophobic duct or pipe was observed [2,3]. Slip velocities on both hydrophobic and hydrophilic surfaces have been extensively studied using various experimental techniques. It has been reported slip lengths are ranging from 20 nm to 1 μm which is comparatively small value since the liquid-solid interaction only affects the slip behavior in these cases [4-6]. Nanoscale structures can mimic the transport owing to liquid slip, resulting in almost frictionless interface, e.g., four to five orders of magnitude faster than conventional fluid flow through pores of 7 nm carbon nanotube diameter. However, the giant slip in a carbon nanotube is an extraordinary case because the liquid molecules are not perfectly filled into the inner space of the nanotube, which breaks continuum theory and causes absolute large liquid slip. Therefore, a deliberate effort to design a low-friction surface is of importance to make a large liquid slip. In order to maintain a large liquid slip in most real practices, the surface should guarantee the Cassie (dewetted) state even under pressured or drag flow conditions.

True superhydrophobic materials have a variety of distinct features such as water contact angle higher than 150° , low contact angle hysteresis, low roll-off angle, and extreme water repellency. Superhydrophobic surfaces have been fabricated generally in two ways. The first involves the formation of a rough surface and the second is to alter a surface chemistry using low surface free energy materials. The first method consists of lithography, crystallization, oxidation, vacuum-assisted deposition, phase separation, and sol-gel method [7-12]. A variety of superhydrophobic surfaces exist in nature, e.g., many superhydrophobic surfaces mimicking a lotus leaf have been

made. Such surfaces require both of appropriate surface roughness and low surface energy. To design and fabricate durable superhydrophobic surfaces the effects of surface geometry, surface free energy, surface states, droplet size, and external environment should be considered [13].

1.2. Microfluidic System

In recent years, considerable progress has been made in the field of microfluidics owing to MEMS technologies. The term of “Microfluidics” is defined in a book as “the science and engineering of systems in which fluid behavior differs from conventional flow theory primarily due to the small length scale of the system” [14]. The main advantages of microfluidics are utilizing the microscopic amount of fluid and the material of which the device is made so that the system can be miniaturized. The miniaturization of the whole system is beneficial in many fundamental studies for chemistry, biology, biophysics, biochemistry, neuroscience, and multidisciplinary courses at which the miniaturized sizes become advantageous. Microfluidic devices have proven ideal tools to accurately handle small volumes of samples, such as proteins or DNA solutions, as well as cell suspensions. Furthermore, it has a great advantage in portable systems for point-of-care or in-the-field detection [15]. An entire analytical procedure can be performed such as pre-treatment, labeling, reaction, detection, separation and mixing using micro total analysis systems called as micro-TAS. Some interesting features in a fluid system are only possible in micro-TAS and microscale regime. In this regard, a concept of the micro-TAS has been constructed by integrating microfluidic components into one automated format.

For the MEMS the device size should be smaller than a millimeter. However, the entire length is not required to be shorter than millimeter for the microfluidic system. The important length scale is not the entire system but rather the length in regard to flow behavior occurred. Though the commercial benefit of microfluidics is still in an early stage, the effort in microfluidic research is consistently growing because the researches of miniaturized systems such as micro-scale and nano-scaled systems promise future trends in nature and science. Fluid mechanics researchers are especially interested in a new era of the fluids phenomena possible at the microscale. Additionally, scientists in almost fields as well as fluid mechanics researchers have begun pursuing microfluidics research since the microfluidic system is applicable to develop new devices in their own fields, e.g., different types of single-walled carbon

nanotubes with semiconducting and metallic characteristics were separated using an active microfluidic platform, which was traditionally conducted by applying electrical charge in a bulk solution. A number of microfluidic devices such as micro-valves, pumps, sensors, mixers, needles, and separators were developed and investigated. It is worthy to note that the microfluidic devices are dealing with the sample volumes from picoliter to hundreds of microliter as shown in figure 1.2.

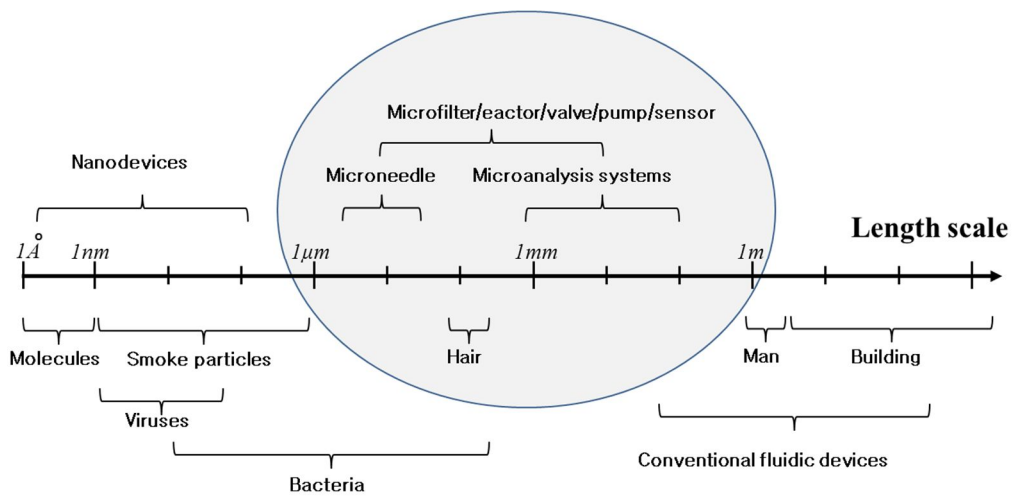


Figure 1.2. Size characteristics of microfluidic devices [1].

1.2.1. Fabrication Technique

Lithography is the most essential technique for fabricating microscale structures. There are some lithography techniques depending on the types of energy beam such as photolithography, electron lithography, X-ray lithography, and ion lithography [1]. The most well-known technique for the fabrication of microfluidic system is photolithography. However, the lithography process is limited to two-dimensional lateral structures. This technique usually utilizes a photosensitive emulsion polymer called as photoresist, which transfers a desired pattern from a mask to a substrate after exposing process. The most famous photoresist polymer commercially used is SU-8. The process of photolithography consists of three steps [1]:

- Positioning process: aligning of the mask and the substrate.
- Exposure process: UV exposure to the photoresist layer.
- Development process: Dissolution or etching of the resist pattern.

Firstly, masks are often made using electron beams with the order of hundreds of nanometer. If sub-micrometric precision is not required, high-quality printout on a glass substrate, called FCG (Film Combine Glass) mask, is often used. In our experiments the FCG mask was used because the process is low-cost, expeditious, accurate, and simple. The substrate is spin-coated with the photoresist polymer and baked. After that, the substrate is aligned with the prepared mask and exposed to light. There are two types of resists, positive and negative, which determine final patterns. The last step consists of immersing the system in a solvent. A typical pattern transfer with lift-off technique is shown in figure 1.3.

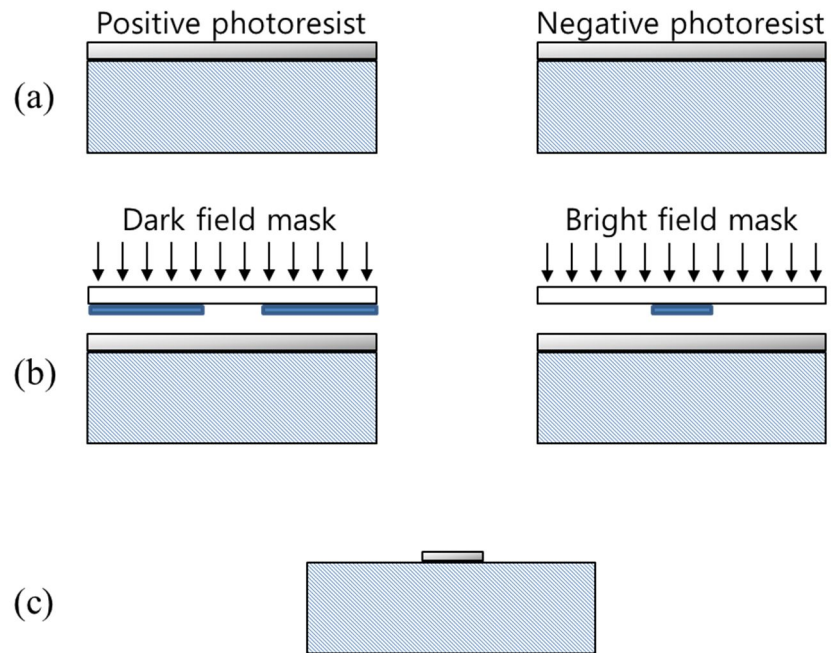


Figure 1.3. A schematic representation of photolithography process: (a) coating photoresist, (b) photolithography, and (c) developing photoresist.

Soft lithography is one of the microcasting methods, which is a direct transfer technique. The term “soft” refers to an elastomeric stamp that Polymethylsiloxane (PDMS) is usually used as PDMS shows good detachability, durability, transparency, and thermal resistance. However, PDMS also have a number of drawbacks such as deformation, volumetric shrinkage after detachment and curing. Therefore, the design of a PDMS part should consider the shrinking effect. There are still some problems remained after producing a microchannel. The attachment with the PDMS and glass cover uses O₂ plasma, in which a temporary –OH groups are formed on both of the PDMS and the glass cover that makes permanent bonding. However, the bonding is susceptible to high pressure and leakage problem often happens, e.g., the width and height of a microchannel is tens of micrometers to hundreds of micrometers, which causes high pressure on the wall of the microchannel.

This process utilizes a photoresist pattern as a master explained previously in figure 1.2. (c). The PDMS is poured on the master pattern and cured at 60 ~ 70 °C. The PDMS layer is then peeled off and bonded to a glass cover after oxidizing their surfaces with oxygen plasma (Figure 1.3). Fluidic interconnects such as inlet and outlet sockets are embedded into a created fluidic channel. Designing of the microchannel is important because too low or high aspect ratio is not desirable and even it fails to operate due to pairing or a sagging of the structure. The recommended range of aspect ratios are from 0.2 to 2 [16].

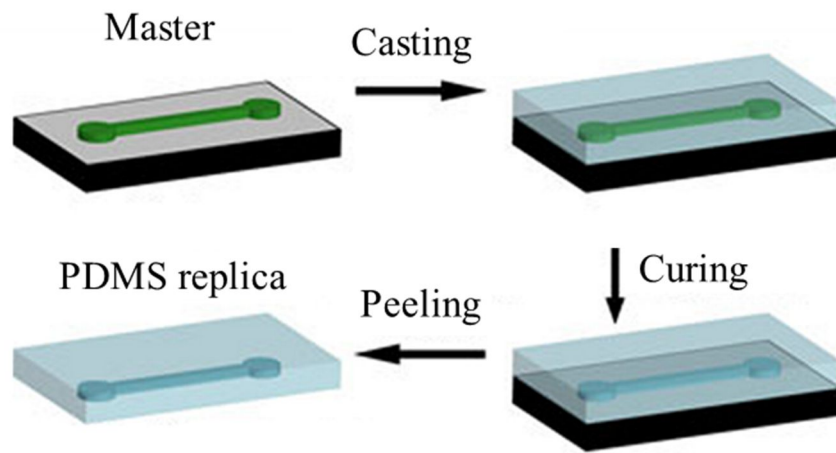


Figure 1.4. A schematic representation of soft lithography.

1.2.2. Particle dynamics in a microchannel

In recent years, there have been significant advances in detection techniques in a microfluidic system with various applications in chemistry, biology, engineering, and drug delivery. The detection system aims to sort or focus interested objects from unsorted and contaminated samples. To achieve the purpose successfully, there has to be a large demand for the development of microfilters for an on-chip separation of the samples with a simple, expeditious, robust, and inexpensive implementation [17]. A detection technique is closely associated with particle dynamics which is a deterministic factor for manipulating suspended objects in a fluid, resulting in high enrichment ratio of the detection. To do the successful detection particle focusing in a single-line or separation depending on different features have to be preceded. The technique is now being used in flow cytometry. To develop an efficient separator on the microfluidic platform, various methods have been executed such as centrifugation, geometrical obstruction, magnetophoresis, electrophoresis, flow bifurcation, membrane integration, ultrasound, gravitation, optical manipulation, and microfiltration. Active methods using external forces to collect and separate objects provide good separation accuracy, however, they are normally limited to low throughput and require accurate instrument for the external energy. Passive methods need no external forces and use the intrinsic properties of fluids and channel geometry. It directly uses hydrodynamic effects that are driven by the geometrical features of microchannels. Passive methods have received significant attention with the aim of the discoveries of many interesting fluid dynamic phenomena in microfluidics [18]. This enables the passive methods to draw attentions to many scientists. In this regard, particle dynamics becomes more significant to understand the particle behavior in the passive-method based microfluidic channels.

In a microchannel, flows are often assumed to be a laminar flow which is associated with negligible inertia. That is, the inertial term in the Navier-Stokes equation becomes zero since the Reynolds number, describing the ratio between inertial force and viscous force, is very small due to small microchannel dimensions.

However, for many cases for the microfluidic platform fluid velocity is not slow to assume the Stokes flow ($Re \sim 0$) [19]. Fluid inertia has been used to manipulate the transverse position of particles in pressure flow. Lee *et al.* reported self-assembly into uniformly spaced flowing lattices with no external force fields that the repulsion force and attractive force are created in inertial flow [20]. The inertial flow system provides an easy way to produce passive particle control in a microchannel platform.

Recently, researches for the particle manipulation are actively investigated with the aid of the development of microfluidics, which is deeply associated with inertial microfluidics in that the combination of shear-gradient lift force, F_{LW} , and wall-repulsion lift force, F_{LS} . It is discussed that two forces act to yield an equilibrium position between the channel wall and centerline in a particle suspended. The wall-induced lift force makes a particle move from the wall towards the channel centerline. And the shear-gradient lift force acts down the gradient in shear rate of the flow. The wall-induced lift force becomes significant in the thin layers near the walls so that particles are not positioned near the wall. Feng *et al.* numerically analyzed the hydrodynamic forces which manipulates the suspended particles and identified two major lateral forces of F_{LW} and F_{LS} [21, 22]. In an axisymmetric Poiseuille pipe flow, the equilibrium position appears as a ring shape called Segré and Silberberg effect. On the contrary, the flows in a square channel exhibit quite different equilibrium positions. The particles are known to be aligned near the centers of each face of the channel rather than a ring shape as the channel Reynolds number increases [23, 24]. The detailed mechanism was also investigated that the formation of the *pseudo* Segré and Silberberg annulus at the inertial migration and the cross-lateral focusing of particles toward the four equilibrium positions [25].

1.3. Objectives of Present Work

As systems are miniaturized, surprising physical phenomena often happen. The present study is dealing with comprehensive information for physical phenomena in a micro-scale system such as liquid slip, superhydrophobicity, and a focusing of confined particles. The extraordinary features of the three phenomena are closely connected with each other, e.g., superhydrophobicity on account of the nanostructured surface induces liquid slip, which in turn resulting in significant drag reduction in a microfluidic system. It is obvious that we should understand the physics behind the micrometric scale and integrate the knowledge among them. Therefore, there are three major topics carried out in this study.

The first, liquid slip behavior is analyzed quantitatively depending on surface wetting condition and surface structure. For the intensive study, the linear and non-linear slip laws are modeled. Goal of the study is to investigate the effect of a nanoengineered surface structure on liquid slip by fabricating the self-assembly structure of nano Zinc Oxide (*n-ZnO*). Our results suggest that liquid slip is affected more greatly by the characteristic length scale (e.g., channel depth and height) and the superhydrophobicity induced by a nanostructure than by the liquid-solid interaction.

The second, multi-scale structures are fabricated to investigate the superhydrophobicity and water bouncing phenomenon. For more detailed investigation, the multi-scale nanostructures are modeled theoretically to predict the CA and CAH through the thermodynamic approach using surface free energy. The numerical results are compared with the experimental results. The multi-scale hierarchical nanostructure shows low FEBs which provoke high CA and bouncing phenomenon due to small energy dissipation towards receding and advancing directions. We elucidates the underlying physics behind the bouncing phenomenon of a water droplet induced by the multi-scale nanostructure with robust theoretical tools such as the free energy barrier (FEB) analysis and the level-set method.

The third, we present a novel concept for the separation of particles using the

incorporation of elasto-inertial effect and dean effect termed as “Dean-coupled Elasto-inertial effect”. The elastic force is induced by the nature of a viscoelastic medium and the dean drag force is contributed by the curved channel geometry. The cooperation of the two forces produces an extraordinary particle focusing region. Numerical analysis of viscoelastic fluid is carried out in order to explain theoretical background and a mechanism for the lateral migration. We believe this platform is very promising to achieve the multiplex particle focusing which is determined by the incorporation of the rheological properties of the fluid and the channel geometry.

1.4. References

- [1] Nguyen NT, Wereley, S. T., *Fundamentals and Applications of Microfluidics*. 2nd ed: ARTECH HOUSE; 2006.
- [2] Watanabe K, Yanuar, Mizunuma H. Slip of Newtonian fluids at solid boundary. *Jsm Int J B-Fluid T*. 1998;41:525-9.
- [3] Watanabe K, Yanuar, Udagawa H. Drag reduction of Newtonian fluid in a circular pipe with a highly water-repellent wall. *J Fluid Mech*. 1999;381:225-38.
- [4] Ruckenstein E, Rajora P. On the No-Slip Boundary-Condition of Hydrodynamics. *J Colloid Interf Sci*. 1983;96:488-91.
- [5] Churaev NV, Sobolev VD, Somov AN. Slippage of Liquids over Lyophobic Solid-Surfaces. *J Colloid Interf Sci*. 1984;97:574-81.
- [6] Pit R, Hervet H, Leger L. Direct experimental evidence of slip in hexadecane: Solid interfaces. *Phys Rev Lett*. 2000;85:980-3.
- [7] Choi SJ, Suh KY, Lee HH. A geometry controllable approach for the fabrication of biomimetic hierarchical structure and its superhydrophobicity with near-zero sliding angle. *Nanotechnology*. 2008;19.
- [8] Miller JD, Veeramasuneni S, Drelich J, Yalamanchili MR, Yamauchi G. Effect of roughness as determined by atomic force microscopy on the wetting properties of PTFE thin films. *Polym Eng Sci*. 1996;36:1849-55.

- [9] Nakajima A, Abe K, Hashimoto K, Watanabe T. Preparation of hard superhydrophobic films with visible light transmission. *Thin Solid Films*. 2000;376:140-3.
- [10] Nakajima A, Fujishima A, Hashimoto K, Watanabe T. Preparation of transparent superhydrophobic boehmite and silica films by sublimation of aluminum acetylacetonate. *Adv Mater*. 1999;11:1365-8.
- [11] Onda T, Shibuichi S, Satoh N, Tsujii K. Super-water-repellent fractal surfaces. *Langmuir*. 1996;12:2125-7.
- [12] Shibuichi S, Onda T, Satoh N, Tsujii K. Super water-repellent surfaces resulting from fractal structure. *J Phys Chem-US*. 1996;100:19512-7.
- [13] Li W, Amirfazli A. Microtextured superhydrophobic surfaces: A thermodynamic analysis. *Adv Colloid Interfac*. 2007;132:51-68.
- [14] Tabeling P. *Introduction to Microfluidics*: OXFORD 2005.
- [15] Pamme N. Continuous flow separations in microfluidic devices. *Lab Chip*. 2007;7:1644-59.
- [16] Xia YN, Whitesides GM. Soft lithography. *Angew Chem Int Edit*. 1998;37:551-75.
- [17] Crowley TA, Pizziconi V. Isolation of plasma from whole blood using planar microfilters for lab-on-a-chip applications. *Lab Chip*. 2005;5:922-9.
- [18] Sim TS, Kwon K, Park JC, Lee JG, Jung HI. Multistage-multiorifice flow fractionation (MS-MOFF): continuous size-based separation of microspheres using multiple series of contraction/expansion microchannels. *Lab Chip*. 2011;11:93-9.
- [19] Di Carlo D. Inertial microfluidics. *Lab Chip*. 2009;9:3038-46.
- [20] Lee W, Amini H, Stone HA, Di Carlo D. Dynamic self-assembly and control of microfluidic particle crystals. *P Natl Acad Sci USA*. 2010;107:22413-8.
- [21] Feng J, Hu HH, Joseph DD. Direct Simulation of Initial-Value Problems for the Motion of Solid Bodies in a Newtonian Fluid .2. Couette and Poiseuille Flows. *J Fluid Mech*. 1994;277:271-301.
- [22] Feng J, Hu HH, Joseph DD. Direct Simulation of Initial-Value Problems for the Motion of Solid Bodies in a Newtonian Fluid .1. Sedimentation. *J Fluid Mech*. 1994;261:95-134.
- [23] Di Carlo D, Edd JF, Humphry KJ, Stone HA, Toner M. Particle Segregation and

Dynamics in Confined Flows. Phys Rev Lett. 2009;102.

[24] Di Carlo D, Irimia D, Tompkins RG, Toner M. Continuous inertial focusing, ordering, and separation of particles in microchannels. P Natl Acad Sci USA. 2007;104:18892-7.

[25] Choi YS, Seo KW, Lee SJ. Lateral and cross-lateral focusing of spherical particles in a square microchannel. Lab Chip. 2011;11:460-5.

II. Liquid Slip Phenomenon on a Nanostructured Surface

2.1. Introduction

Although the no-slip boundary condition has been widely applied to scientific and engineering problems, liquid slip is also a generally accepted phenomenon that occurs when a viscous fluid is moving adjacent to a solid boundary [1, 2]. In particular, the slip phenomenon draws big interest as precision systems are fabricated at micrometer or nanometer scale and adopted in a variety of applications such as microfluidics, MEMS, sensors, friction systems, and biophysics [3, 4]. For instance, it is reported that extraordinarily fast flow is generated in nanoscale structures, which would have a wide range of potential applications for transdermal drug and selective chemical sensing in biological channels [5].

While the liquid slip has been observed experimentally at micro and nanoscale, its fundamental mechanism is still controversial and has yet to be fully understood [6-10]. In general, it is known that liquid molecules are capable of slipping at liquid-solid interface when the liquid possesses a low wettability due to superhydrophobicity, thus resulting in drag reduction. This is the so called Navier slip for a Newtonian liquid (similarly Maxwell's slip for a Newtonian gas). The Navier slip still remains as a gold standard of liquid slip. For some cases, the simple linear Navier slip law may fail to describe the slip behavior well, thus the non-linear Navier slip law is proposed that the slip length is a function of the shear stress [12].

On the other hand, slip flow regimes have been classified by using the Knudsen number and the classical Navier-Stokes equation was modified by adding a new velocity concept [13, 14]. It has been proven that hydrophobic coating induces an increase in slip velocity due to minimized surface energy in microchannels [9]. The

small slip length in hydrophilic channels and the large slip length in hydrophobic channels have been calculated analytically by using the excessive flow rate of the Poiseuille flow for the applied pressure drop [15]. The findings from nanoscale hydrodynamic experiments and molecular dynamic simulations indicate that the slip length may be gigantic compared with the dimension of the observing system. For example, pressure driven flow rates through an aligned MWCNT membrane with pores of 7 nm diameter are four to five orders of magnitude higher than those predicted by the conventional fluid flow [5, 16].

Liquid slip depends on various parameters such as nonlinear relationship between slip length and local shear rate [17, 18], inherent properties of suspended liquid [19], fluid-surface interaction [20-22], and friction reduction by surface structures [23-27]. It has been reported that fluid-solid molecular interactions have more critical effects on the slip length than the type of flow [20]. Also, low free surface energy reduces the molecular attraction between liquid and surface [21]. Thermodynamically stable nanostructures have been fabricated to maximize the slip length [23-27]. The liquid-solid contact area was significantly minimized by superhydrophobic nanoturf surface [23] so that air pockets below the liquid supported the flow, resulting in a very large slip length of about 50 μm . A giant slip length as large as 185 μm was achieved by developing almost perfectly structured surfaces [24] with control of the pitch and height of the pillars, which delayed the transition from the dewetted (Cassie) state to the wetted (Wenzel) state under pressurized flow conditions. The scaling law approach was also employed for generic geometries to predict the effective slip length and to quantify their superlubricating potential [25]. Large slip effects may be interpreted by considering the contact angle (CA) according to the dewetting behavior between the fluid and solid surfaces [26, 27].

Liquid slip, indeed, is not only an important phenomenon occurring especially at micro and nanoscale but also a complicated phenomenon whose physics and chemistry need to be understood. In this study, the liquid slip behavior is analyzed quantitatively with respect to surface interaction and surface structure. And the linear and non-linear slip laws are modeled to investigate the liquid slip behavior in regard to the non-

linearity. Our results suggest that liquid slip is affected more greatly by the characteristic length scale (e.g., channel depth and height) and the superhydrophobicity induced by a nanostructure than by the liquid-solid interaction.

2.2. Theoretical Background

2.2.1. Analytical Prediction

Fig. 2.1 shows a rheometric measurement system with two parallel disks, where the upper disk rotates at the angular velocity of ω . The fine and bold lines are the velocity distributions without and with wall slip, respectively. When the upper disk rotates at a velocity of $\omega \cdot r$ where r is the radius, the fluid velocity adjacent to the upper disk decreases due to the slip at the wall. Assuming steady, laminar, and isothermal flow, the momentum balance of the fluid is expressed in the cylindrical coordinate system as follows (body force and cylindrical edge effect are neglected).

$$\frac{\partial \tau_{\theta z}}{\partial z} = 0 \quad (1)$$

For the slip system shown in Fig. 2.1, the boundary conditions are given by the following equations.

$$v_{\theta}(z=0) = \delta_1 \left(\frac{\partial v_{\theta}}{\partial z} \right)^m, \quad v_{\theta}(z=h) = \omega \cdot r - \delta_2 \left(\frac{\partial v_{\theta}}{\partial z} \right)^m \quad (2)$$

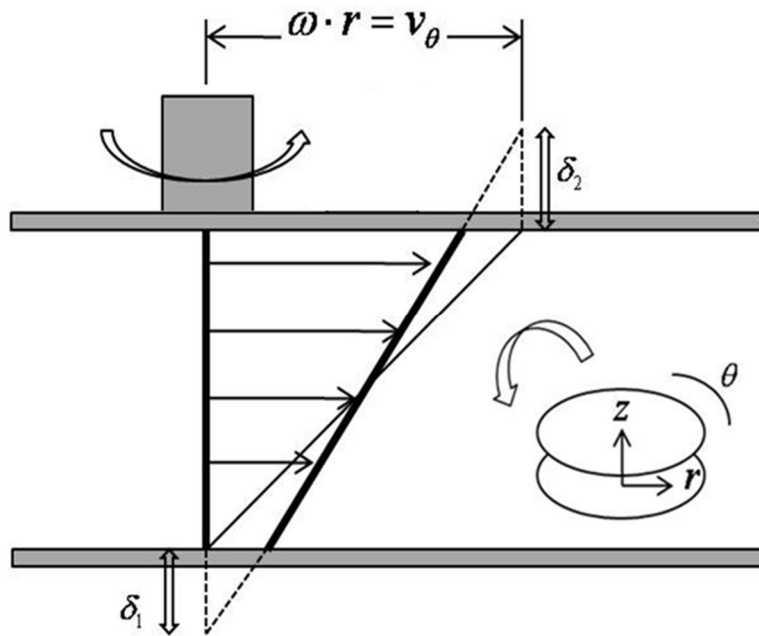


Figure 2.1. Schematic diagram of a parallel-disk rheometer with liquid wall slip at angular velocity.

where h is the gap between the two disks, v_θ is the velocity in θ direction, and δ_1 and δ_2 are the slip lengths over the lower disk and upper disk, respectively. The two slip lengths are assumed equal for simplicity. The exponent m stands for the non-linearity of the slip law. The linear Navier slip law is recovered when the exponent is equal to unity. The momentum balance and boundary condition are then translated into two universal forms as below.

$$v_\theta(r, z) = C_1(z + \delta C_1^{m-1}) \quad (3)$$

$$C_1^m + (h/2\delta)C_1 - (\omega \cdot r / 2\delta) = 0 \quad (4)$$

And rotational torque (T) is derived as below.

$$T = \int_0^R (2\pi r^2 \tau_{\theta z}) dr = 2\pi\mu \int_0^R r^2 \cdot C_1 dr \quad (5)$$

The rotational torque is simply derived for the linear Navier slip model. On the other hand, the non-linear Navier slip models show semi-analytical equations that are numerically solvable. For the linear Navier slip model, the following analytical equation is obtained.

$$h + 2\delta = \pi \frac{\mu\omega}{2T} R^4 \quad (6)$$

The torque applied to the rotating disk is measured for various shear rates and angular frequencies. At each shear rate and angular velocity, the torque is recorded after the rotating disk reaches steady state with less than 3% deviation. The slip lengths are calculated using the angular velocity, measured torque, and measured viscosity.

2.2.2. Thermodynamical Approach

The $n\text{-ZnO}$ surface is involved in either a non-composite Wenzel state or a composite Cassie state[28]. The free energy of a surface determines the state and that the state shows sticky or slippery condition. The energy is primarily governed by the surface geometry, which is calculated by coupling both of geometrical constitution and free energy transition [29]. For the non-composite state the thermodynamic expressions are as below.

$$\theta_i \frac{L_i^2}{\sin^2 \theta_i} - L_i^2 \cot \theta_i = \theta_j \frac{L_j^2}{\sin^2 \theta_j} - L_j^2 \cot \theta_j \quad (7)$$

$$F_{i \rightarrow j} / \gamma^{la} = \left(\theta_j \frac{L_j}{\sin \theta_j} - \theta_i \frac{L_i}{\sin \theta_i} \right) + a \cos \theta_Y \quad (8)$$

$$\theta_j \frac{L_j^2}{\sin^2 \theta_j} - L_j^2 \cot \theta_j + 2bh = \theta_k \frac{L_k^2}{\sin^2 \theta_k} - L_k^2 \cot \theta_k \quad (9)$$

$$F_{j \rightarrow k} / \gamma^{la} = \left(\theta_j \frac{L_j}{\sin \theta_j} - \theta_k \frac{L_k}{\sin \theta_k} \right) - (b + 2h) \cos \theta_Y \quad (10)$$

When a system is the composite state, the term $2bh$ in eq. 9 and $2h \cos \theta_Y$ in eq. 10 corresponding to the effect of pillar height vanishes and $-b$ in eq. 10 turns to $+b$. In our system, a and h are the width and height of $n\text{-ZnO}$ pillar and d is the spacing between two pillars. The values are 20 nm, 200 nm, and 100 nm, respectively. An initial condition is that the contact angle of a flat ZnO surface [30] is 100° and the diameter of a droplet is 10^{-2} m. The normalized free energy shows that the Wenzel surface and Cassie surface have the minimum free energies at the angle of 138° and 149° (Fig. 2.2 and 2.3). This theoretical result implies that the $n\text{-ZnO}$ surface with the contact angle of 152° is the Cassie surface.

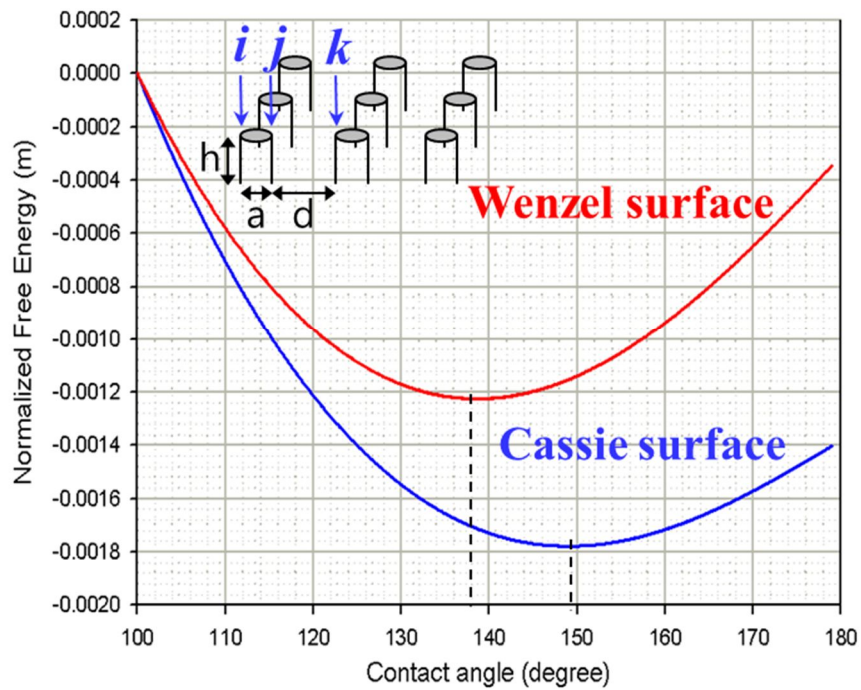


Figure 2.2. normalized Free energy (FE) with contact angle of both Wenzel and Cassie surfaces.

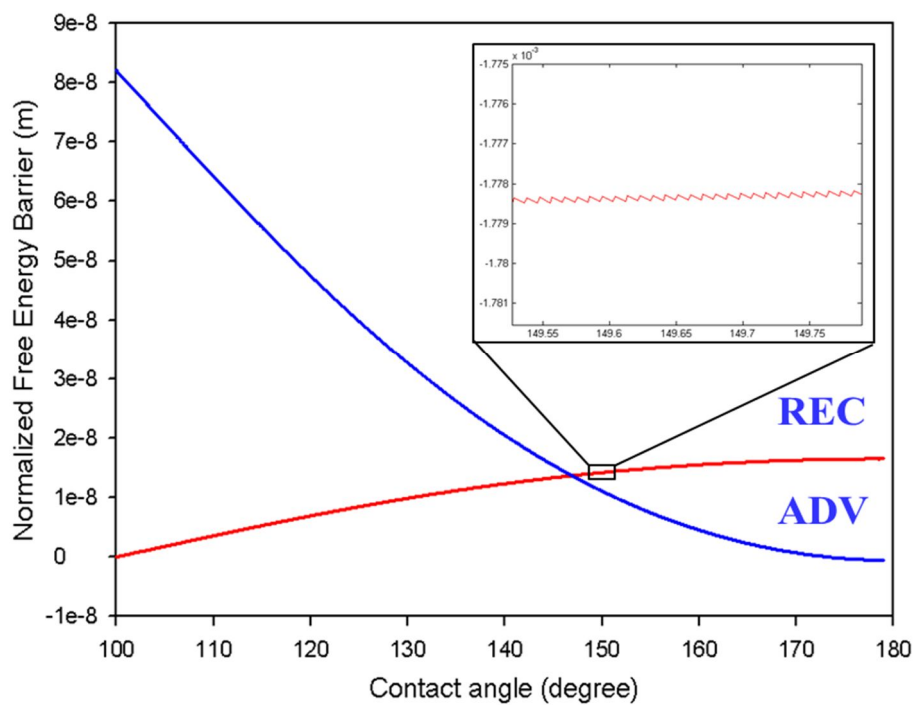


Figure 2.3. Normalized Free energy barrier (FEB) with contact angle of Cassie surface.

2.3. Experimental Section

2.3.1. Rheological Characterization

Silicone oil with the viscosity of 1 Pa·s was employed to measure the wall slip over smooth, hydrophobic, and *n-ZnO* nanostructured surfaces. Rheological properties of the fluid were measured with the parallel disk rheometer (AR-2000, TA Instrument, U.S.A.).

The gaps between the two disks of the rheometer were varied to 1000, 500, 200, 100, 80, 60, and 40 μm to investigate the scale dependency of the liquid slip behavior. Experimental data on the rotating velocity, torque, and viscosity were acquired in a steady shear rate mode at the angular velocity ranging from 0.1 to 300 rad/s. Oscillatory experiments were also carried out to verify the drag reduction in the steady shear rate mode

2.3.2. Self-assembly of Zinc Oxide

As the smooth surface, a steel disk was finely polished to minimize surface roughness. As the hydrophobic surface, Trichloro (1*H*,1*H*,2*H*,2*H*-perfluorooctyl) silane was spin coated onto the smooth surface. *n-ZnO* nanostructure was constructed onto a glass substrate by the self-assembling method[31] in a bid to generate superhydrophobicity. To grow the *n-ZnO* on the glass, the glass substrate was washed in a cleaning solution ($\text{H}_2\text{SO}_4:\text{H}_2\text{O}_2 = 4:1$) at 110 °C for 15 min and then deionized with water for 5 min. *ZnO* nuclei were prepared by using 30 mM zinc acetate [$\text{Zn}(\text{C}_2\text{H}_3\text{O}_2)_2$] solution in ethanol at 90 °C for 15 min. The seed solution was spin-coated onto the glass substrate at 1500 rpm for 60 s. After then, the seed coated substrates were thermally annealed at 100 °C for 5 min to remove the residual solvent. The glass substrates were immersed in an aqueous solution consisting of 25 mM zinc nitrate hexahydrate [$\text{Zn}(\text{NO}_3)_2 \cdot 6\text{H}_2\text{O}$], 25 mM hexamethylenetetramine [$\text{C}_6\text{H}_{12}\text{N}_4$] (HMT) and

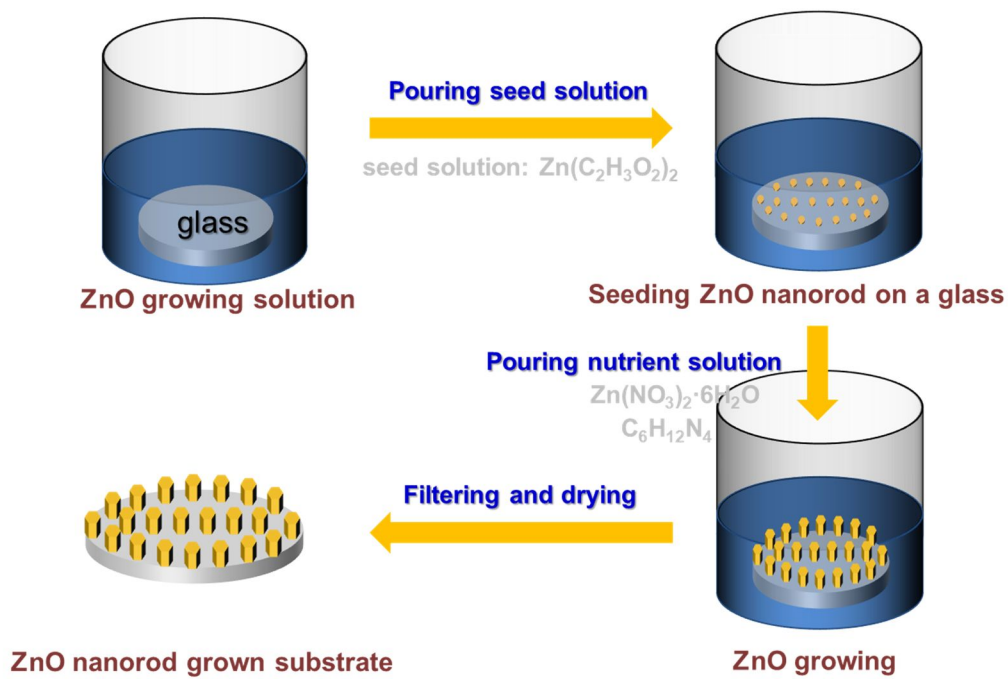


Figure 2.4. Schematics of self-assembling method of Zinc Oxide on a glass substrate.

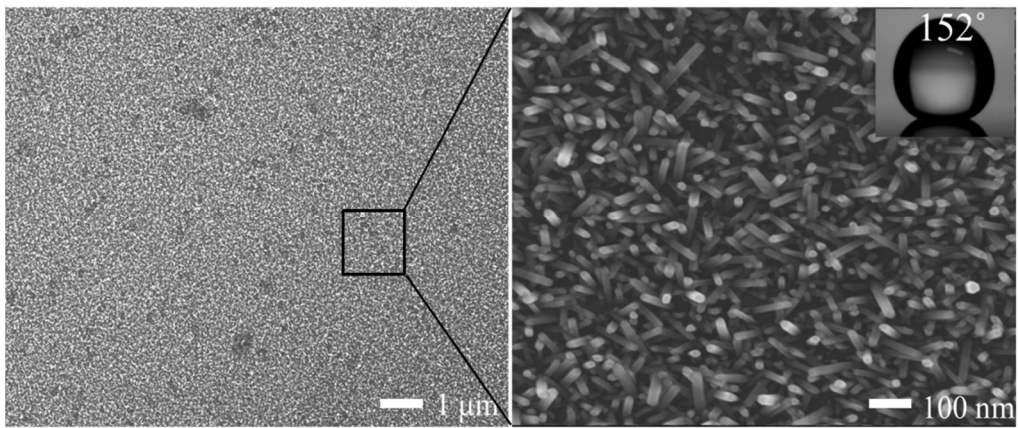


Figure 2.5. SEM image of *n-ZnO* nanostructured surface and magnified view of the *n-ZnO* hexagonal pillars.

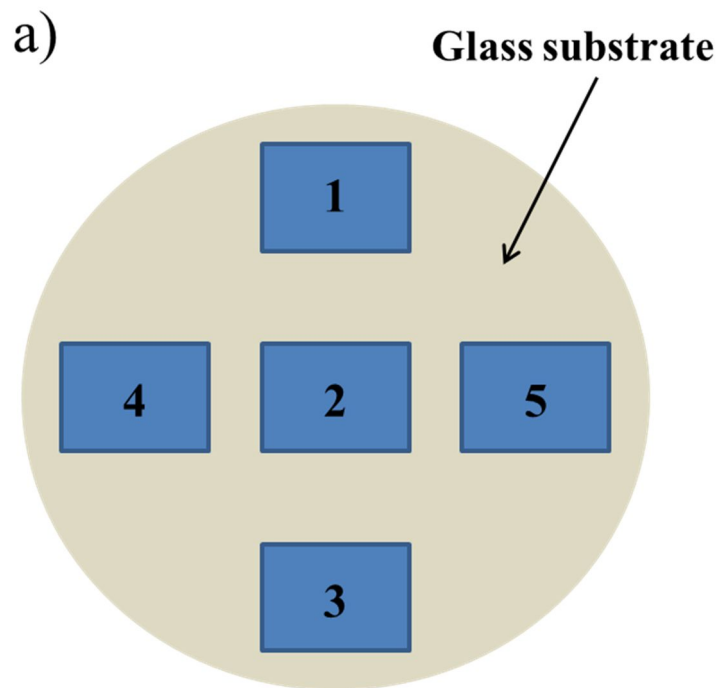


Figure 2.6. Contact angle measurements at five positions on an *n-ZnO* nanostructured glass substrate. (a) Schematic representation of the glass substrate, (b) Contact angles of a sessile water droplet on the glass substrate before the self-assembly of Zinc Oxide, (c) Zinc oxide self-assembled glass substrate after 4 hours, and (d) 1 day.

b)

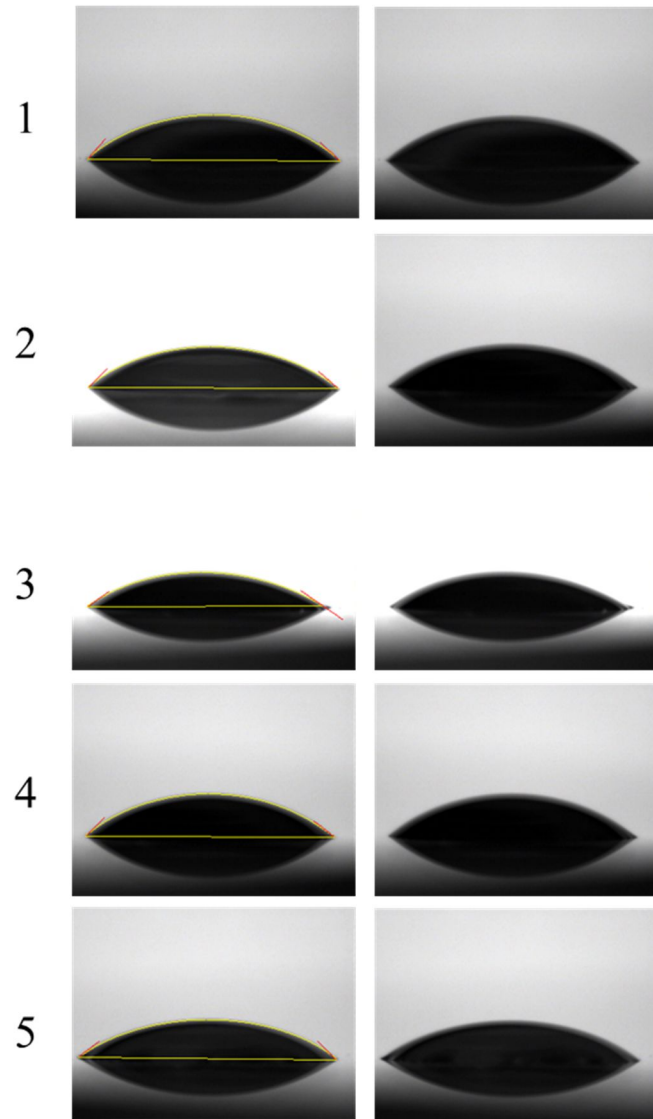


Figure 2.6. (Continued.)

c)

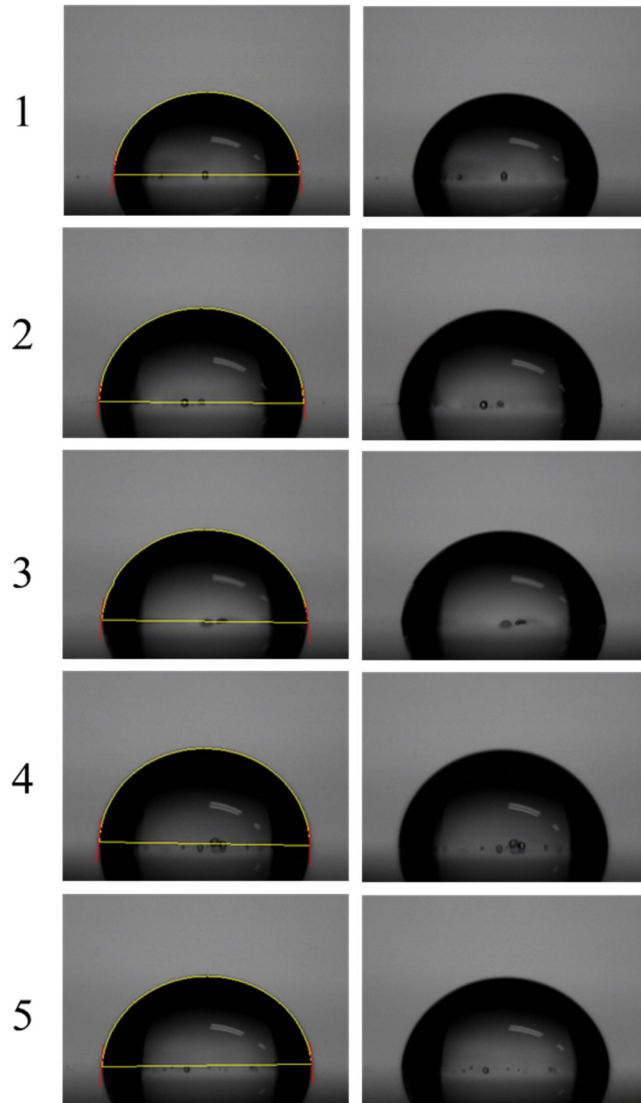


Figure 2.6. (Continued.)

d)

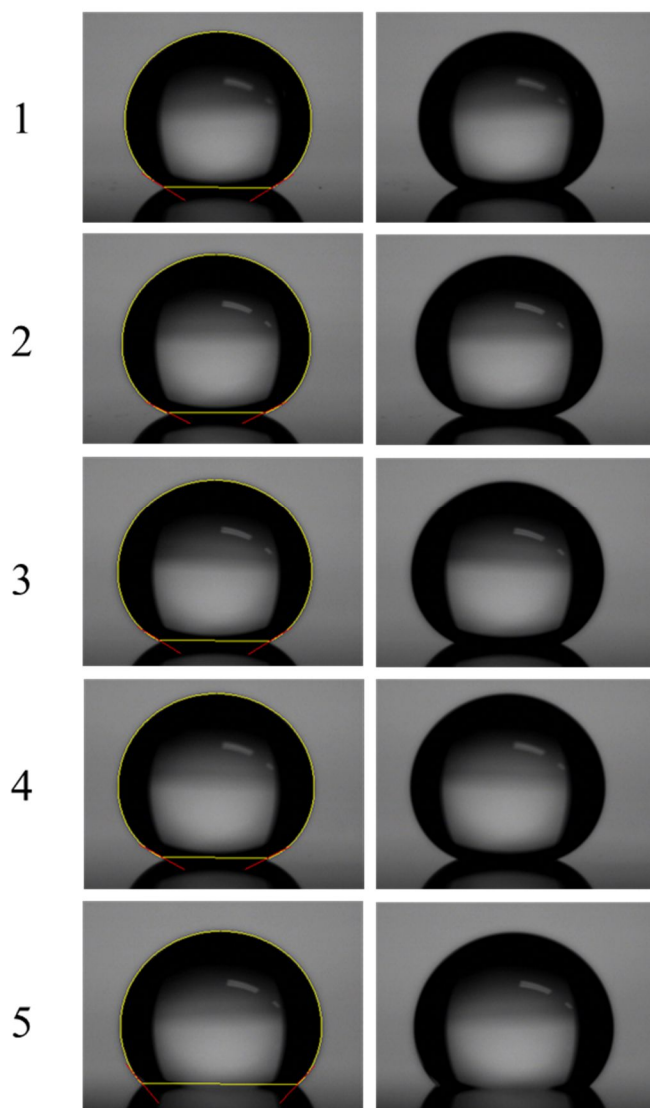


Figure 2.6. (Continued.)

Table 2.1. Characteristics of a sessile water droplet on the glass substrate before the self-assembly of Zinc Oxide.

Index	Contact angle	Left angle	Right angle
1	45.24152	48.53985	41.94318
2	42.3041	44.15513	40.45307
3	34.91747	34.4856	35.34933
4	40.90481	44.15585	37.65376
5	40.97693	38.59256	43.3613

Index	Drop volume	Wetting energy	Spreading Coefficient	Work of Adhesion
1	15.63743	51.25994	21.54007	124.0599
2	13.33239	53.84164	18.95836	126.6416
3	7.648155	59.69437	13.10564	132.4944
4	12.36968	55.02214	17.77786	127.8221
5	13.78618	54.96209	17.83791	127.7621

Table 2.2. Characteristics of a sessile water droplet on the Zinc oxide self-assembled glass substrate after 4 hours.

Index	Contact angle	Left angle	Right angle
1	83.36293	83.36293	83.36293
2	84.52522	85.02344	84.02702
3	84.36244	86.10601	82.61887
4	85.56422	84.33395	86.79449
5	85.36195	84.63055	86.09335

Index	Drop volume	Wetting energy	Spreading Coefficient	Work of Adhesion
1	18.43234	8.414233	64.38577	81.21423
2	25.12862	6.945693	65.85431	79.7457
3	25.38177	7.151549	65.64845	79.95155
4	27.69792	5.630489	67.16951	78.4305
5	27.23792	5.886689	66.91331	78.68669

Table 2.3. Characteristics of a sessile water droplet on the Zinc oxide self-assembled glass substrate after 1 day.

Index	Contact angle	Left angle	Right angle
1	148.1285	147.8668	148.3901
2	153.5844	153.5844	153.5844
3	148.8017	149.0193	148.5842
4	151.9185	151.5574	152.2796
5	131.757	130.8071	132.7068

Index	Drop volume	Wetting energy	Spreading Coefficient	Work of Adhesion
1	8.246064	-61.82422	134.3242	10.97578
2	6.079693	-65.19899	137.999	7.601013
3	8.883532	-62.27165	135.0717	10.5285
4	7.803516	-64.2299	137.0299	8.570104
5	21.45021	-48.48278	121.2828	24.61722

deionized (DI) water. The main growth of ZnO nanopillars was carried out at 90°C for 60 min.

2.4. Results and Discussion

2.4.1. Determination of Surface Condition

Surface properties strongly affect flow resistance through a channel, especially through microchannels or nanochannels with a large surface-to-volume ratio. Surface friction may be decreased as the corresponding surface roughness is increased, which is contrary to the common knowledge [32]. Several possible reasons have been suggested for such a reduction of the surface friction, e.g., molecular slip [6] at the solid-liquid interface due to the low interaction energy and the existence of nanobubbles [8-10] at the solid-liquid interface. Micro and nanoengineered structures are of great importance for fabrication of a fluidic device that maintains the dewetted (Cassie) state in which air penetration is impeded. These structures can allow very large effective liquid slip [23]. In this study, an *n-ZnO* nanostructure was self-assembled on the glass substrate to generate the dewetted state during steady and oscillatory motion (Fig. 2.4 and 2.5). It is shown in Fig. 2.5 that the *n-ZnO* pillars were uniformly grown over the entire surface. The *n-ZnO* nanostructure consisting of 20 nm diameter hexagonal pillars created an air-trapping system, in which liquid could not penetrate readily into the interspace between pillars [33]. Choi and Kim [23] suggested the critical pitch and height of the uniform structure from the calculation of geometrical constitution such that the pitch should be less than 1 μm and the height should be larger than 0.2 μm . Since the liquid is silicone oil ($\sigma \sim 0.02 \text{ N/m}$) and ΔP is assumed to be 0.1 MPa ($\sim 1 \text{ atm}$) in this study, the critical pitch and height are around 0.3 μm and 55 nm, respectively, which are suitable for the Cassie state of the *n-ZnO* nanostructure. The pillars have very narrow pitches and an average height of 200 nm, which satisfy the dewetted (Cassie) surface condition [23].

2.4.2. Liquid Slip Phenomenon

Effective shear stress is obtained from the measured torque and plotted with respect to the shear rate as shown in Fig. 2.7. When the channel height is 1000 μm , the slope of the curve for the smooth surface shows the dynamic viscosity of silicone oil ($\approx 1 \text{ Pa}\cdot\text{s}$) under the assumption that the oil is a Newtonian fluid and the shear stress follows $\tau = \mu\dot{\gamma}$ (where μ = dynamic viscosity and $\dot{\gamma}$ = shear rate). The slope decreases with decreasing the channel height from 1000 to 40 μm (Fig. 2.7 and Fig. 2.14). During the steady shear experiments, dynamic viscosities for the smooth, hydrophobic, and *n-ZnO* Cassie surfaces decrease significantly with respect to the channel height (Fig. 2.8 and Fig. 2.13). It shows that the liquid slip is clearly dependent on the characteristic length scale. For the *n-ZnO* nanostructured surface, the viscosity decreasing rate is larger than that of the smooth surface or the hydrophobic surface, which can be explained by the reduction of solid-liquid friction due to trapped air in the dewetted (Cassie) state.

A linear relationship between slip velocity and shear rate at the wall called the linear Navier slip law is invited often to bridge between theory and experimental data. For some cases, the non-linear Navier slip law can provide better results for describing the slip phenomenon [12, 17]. In our case, liquid slip is increasing with the non-linearity as shown in Fig. 2.9. Interestingly, the slip is also increasing when the channel height is decreasing (see an inset figure). Fig. 2.9b obviously demonstrates that the constant C_l (meaning shear rate at the wall) is drastically decreasing with the non-linearity at the same slip length.

When the channel height is 40 μm , dynamic viscosity and liquid slip length of the smooth surface are largely different from those of the hydrophobic or *n-ZnO* Cassie surfaces (Fig. 2.10a and 2.10b). When the surface is coated with a hydrophobic solution, liquid-solid surface interaction is decreased because the low free surface energy reduces the molecular attraction between the liquid and the surface, resulting in a larger slip length than that of the smooth surface. In the case of the *n-ZnO* nanostructure, the

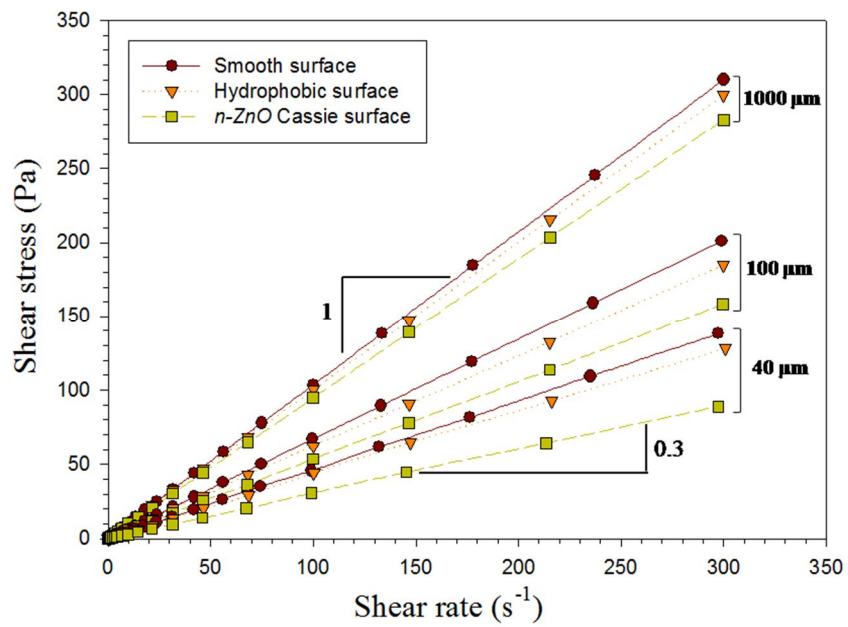


Figure 2.7. Shear stress as a function of shear rate measured for different surfaces.

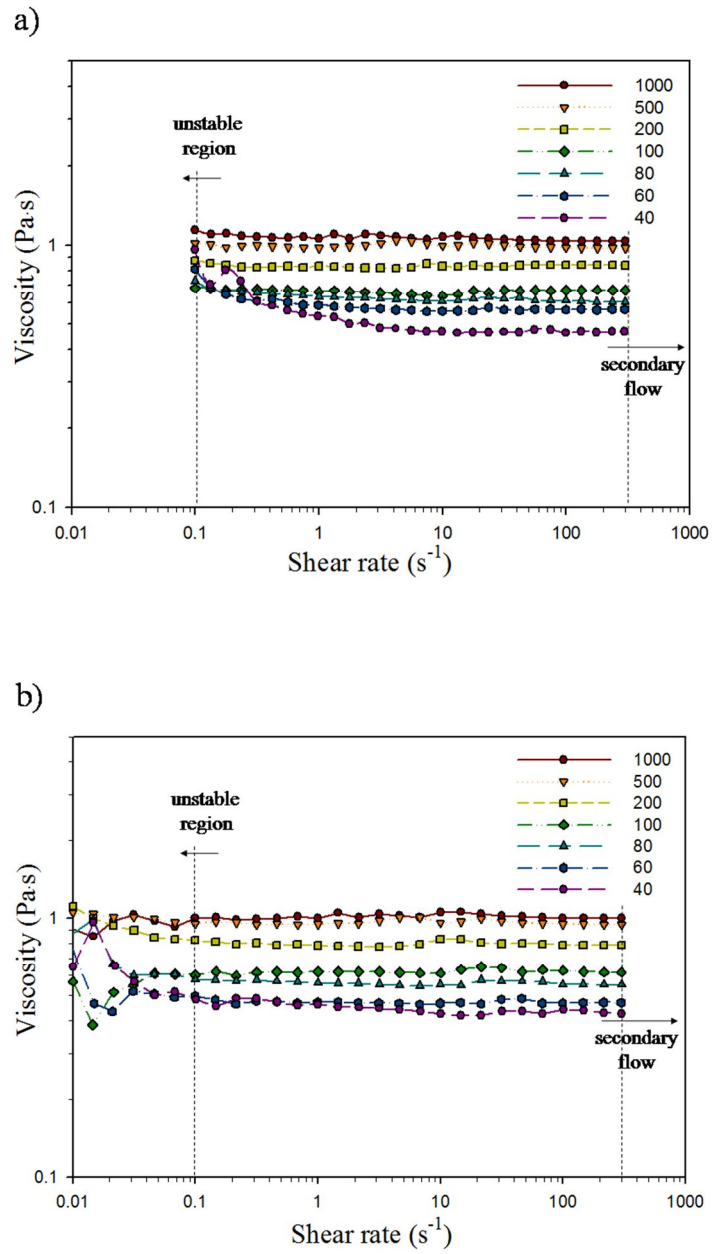


Figure 2.8. Dynamic viscosity measured by the steady shear experiment for various channel heights: (a) smooth surface, (b) hydrophobic surface, and (c) *n-ZnO* Cassie surface.

c)

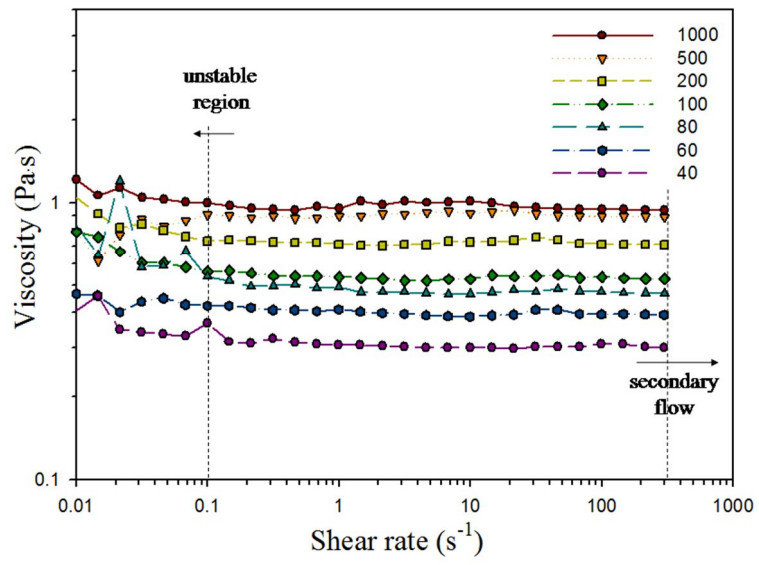


Figure 2.8. (Continued.)

air cushions below the liquid act as frictionless surfaces so that lower dynamic viscosity and the largest liquid slip ($\sim 47 \mu m$) are obtained. A nonlinear relationship exists between the amount of slip and the local shear rate (Fig. 2.10b), which is not explained by the linear Navier slip model. By using molecular dynamics [17], Peter *et al.* claimed that the boundary condition may be nonlinear even though the liquid is still Newtonian.

Liquid slip can have more important role when the characteristic length is scaled down. For example, flow rates through the slippery channel are up to four to five orders of magnitude higher than predicted flow rates through pores of 7 nm diameter MWCNTs [5] since the characteristic length scale of the system is extremely short. In this sense, the liquid slip length needs to be described in terms of the characteristic length to figure out the slip effect from a more quantitative standpoint (Fig. 2.11). All three surfaces showed significant increase in the slip length as the height was scaled down. Among them, the *n-ZnO* nanostructure surface showed the largest increase in the slip length. When the liquid-solid interaction becomes large, CA decreases due to the larger surface area between the liquid and the solid. Adhesion is expressed thermodynamically as $W_{SL} = \gamma_{LV}(1 + \cos\theta)$, where W_{SL} is the work of adhesion and γ_{LV} is the surface tension of the liquid. In the partial wetting condition, i.e., when $\gamma_{LS} + \gamma_{LV} > \gamma_{SV}$, the boundary conditions are very different from the no-slip condition[27]. The liquid slip length can increase significantly as the CA increases. Experimental results are in good agreement with the above explanation, i.e., the liquid slip length increases with the CA. For the *n-ZnO* nanostructure with the CA of 152° , the slip length is larger than those of the hydrophobic and smooth surfaces having relatively low CAs for every channel height. The effect of the slip length on drag reduction can be demonstrated simply as $(\tau_{slip} / \tau_{no-slip}) = 1 / (1 + \delta / h)$, where τ_{slip} and $\tau_{no-slip}$ are shear stresses at the wall when slip and no-slip boundary conditions are applied, respectively [23]. When $h / H = 0.04$ ($40 \mu m$ in height at the shortest in our case), the value of δ / h is 1.2, which represents nearly 55 % reduction of the drag

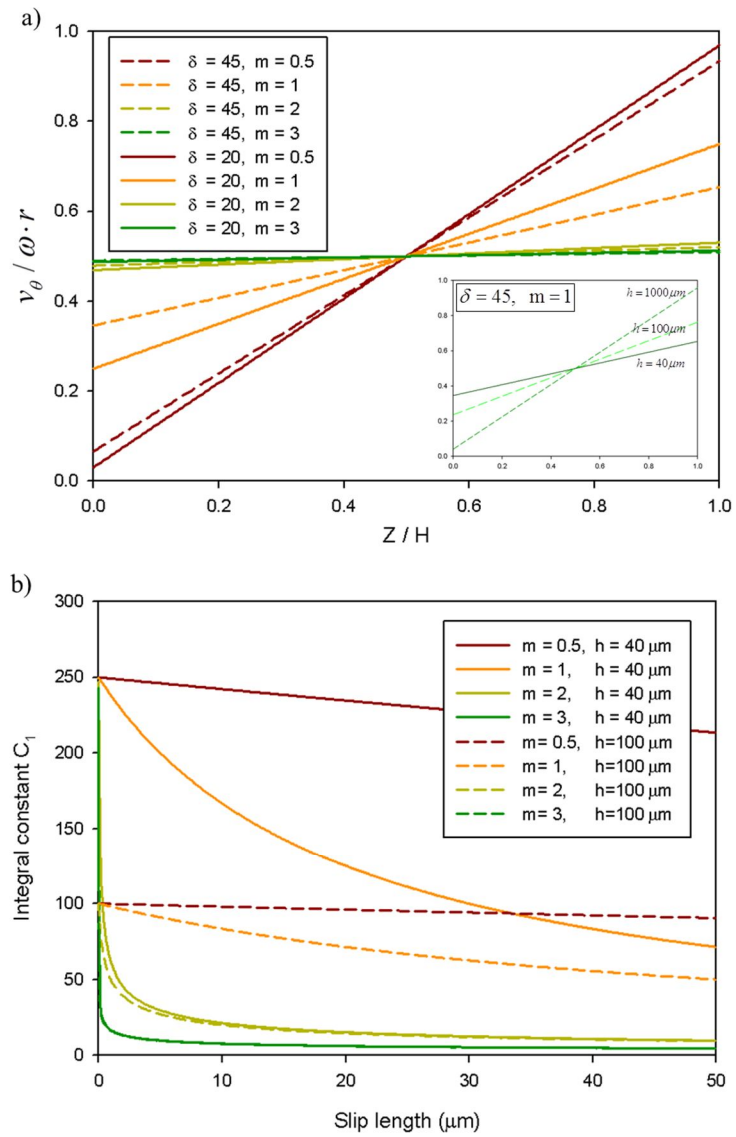


Figure 2.9. (a) Velocity profiles with the linear and non-linear Navier slip exponents. An inset graph shows a height dependence on slip velocity, (b) integral constant C_1 and slip length with the linear and non-linear Navier slip exponents

compared with the shear stress in no-slip condition. This result implies that much higher liquid transport is possible at micro and nanoscales.

It is noticed that the liquid slip is affected significantly by the characteristic length scale and that a large liquid slip results from superhydrophobicity, which is induced by the nanostructure rather than by the minimization of liquid-solid interaction. It is expected that this study can provide meaningful insight into microfluidics and micro and nanoplateforms, particularly when small driving power or energy is required to operate such fluidic systems.

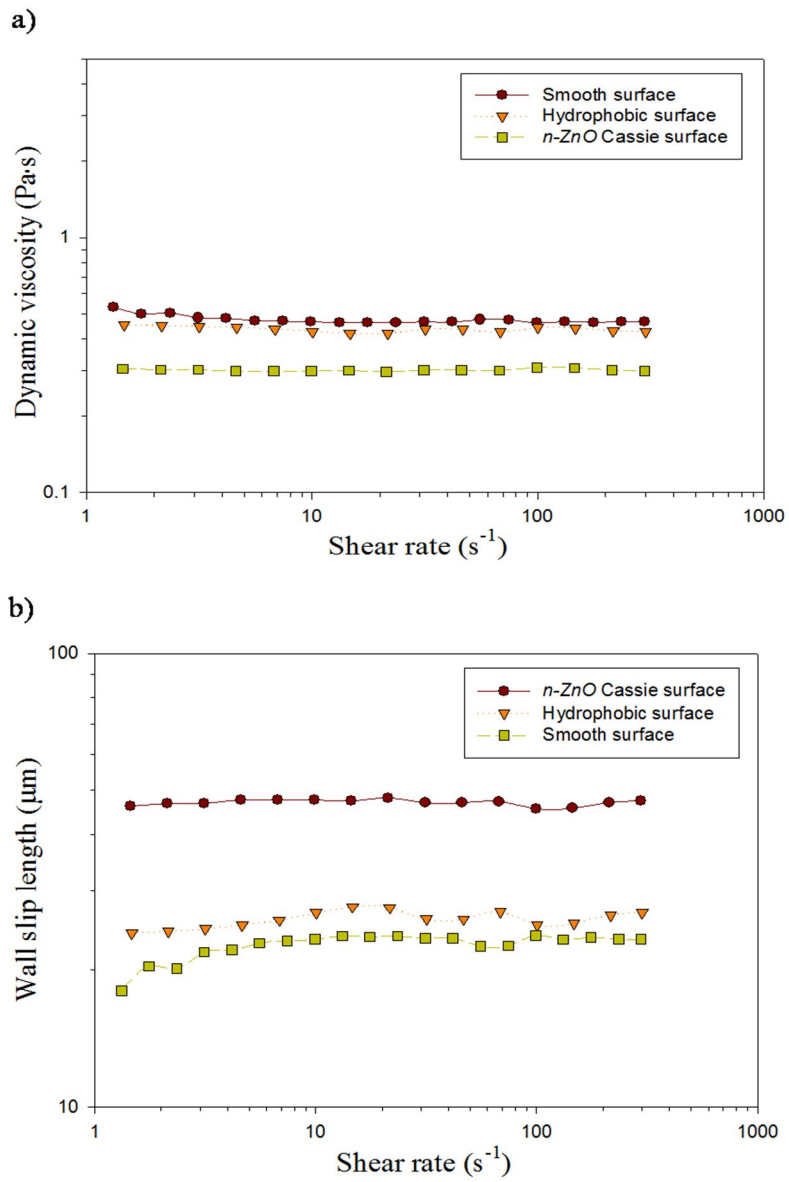


Figure 2.10. (a) Dynamic viscosity and (b) wall slip length measured by the steady shear experiment at 40 μm channel height for smooth, hydrophobic, and *n*-ZnO Cassie surfaces.

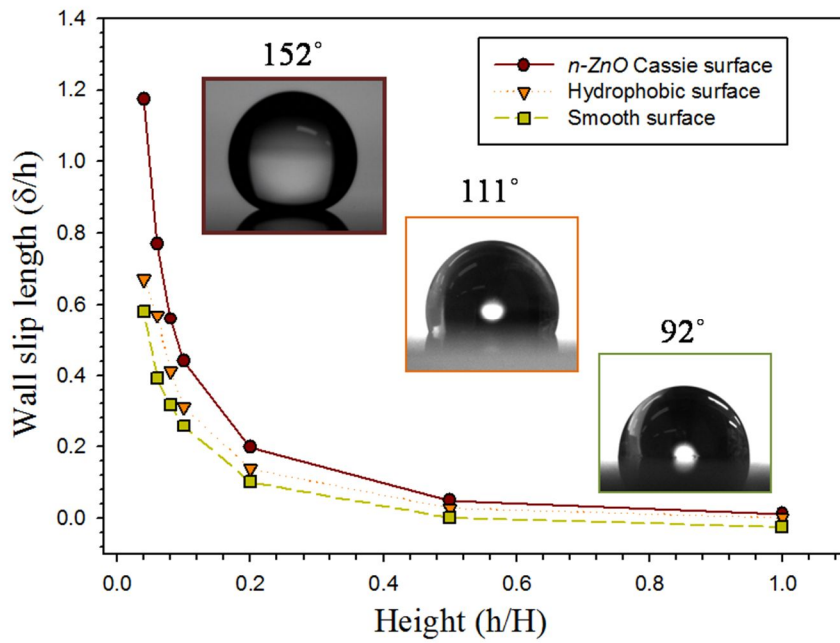


Figure 2.11. Wall slip length measured with respect to the channel height for different surface features.

2.5. Summary

The influence of liquid-solid surface interaction and nanoengineered surface structure on liquid slip was investigated. It was found that the nanostructure fabricated for the dewetted (Cassie) state had more effects on liquid slip than minimization of the liquid-solid surface interaction. It was implied by the results that the molecular slip or nanobubbles generated by interaction minimization were not good enough to provoke large slip and that the Cassie surface should be guaranteed for the large slip. Drag reduction was also increased significantly as the characteristic length was scaled down to micro and nanoscale. The linear and non-linear Navier slip model showed that liquid slip behavior is more obvious when increasing the non-linearity. The large liquid slip can be utilized to transform conventional micro and nanofluidic platforms into highly energy efficient devices with higher transport capability and less driving energy.

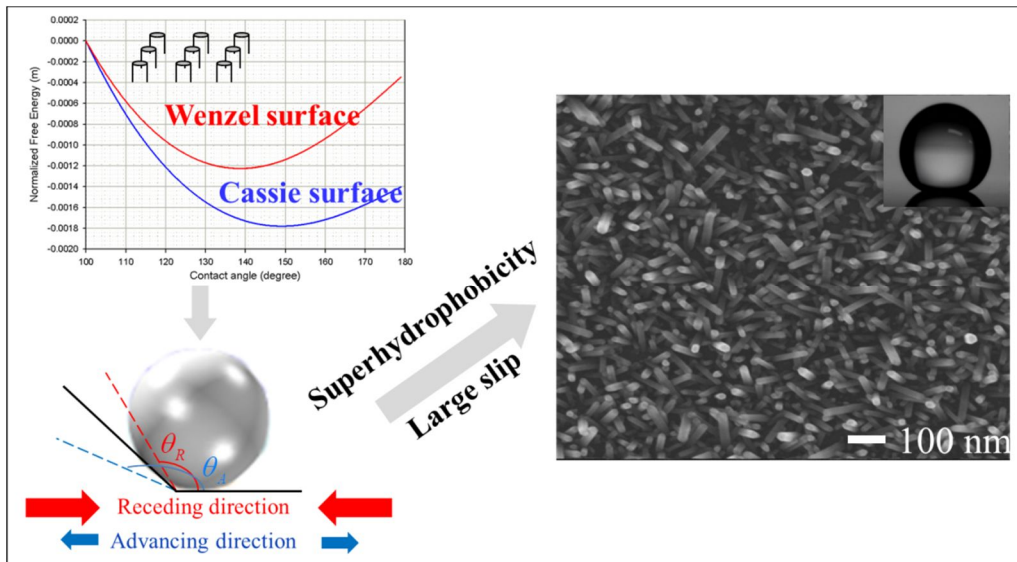
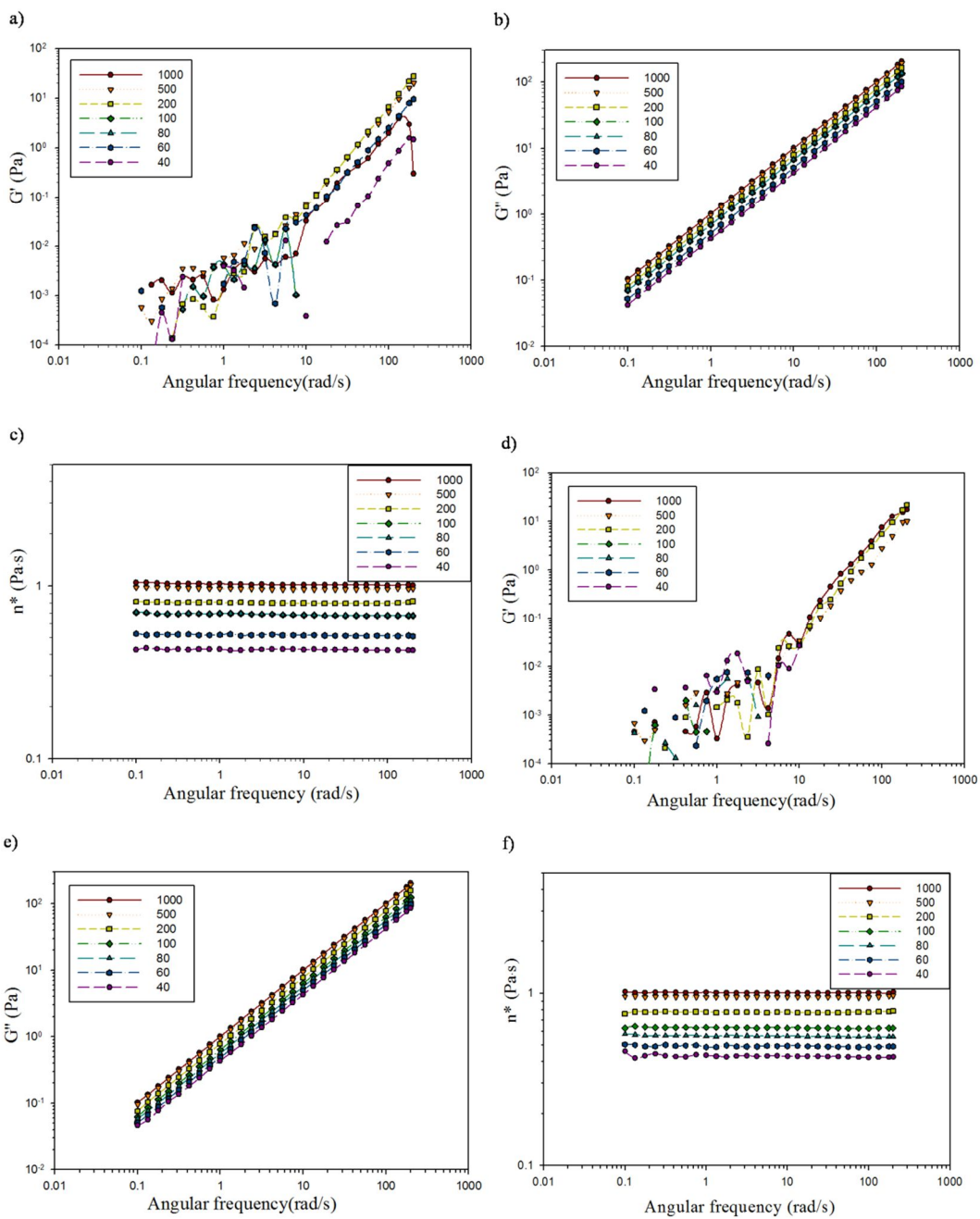


Figure 2.12. Schematics of Superhydrophobicity and liquid slip phenomena caused by the surface free energy.

2.6. Supplementary Information

Supplementary information is provided for the convincing evidence of liquid slip phenomenon. Complex viscosity is calculated using the storage modulus and loss modulus during the oscillatory motion. During the oscillatory motion silicone oil shows a linear increasing in loss modulus which means very viscous and Newtonian behavior, resulting in plateau regions of the complex viscosity. The tendency of the complex viscosity over the smooth, hydrophobic, and *n-ZnO* Cassie surfaces are in agreement with the dynamic viscosity results. The shear stresses are linearly increasing with respect to the shear rate on account of the Newtonian behavior of silicone oil. The shear stress is decreasing with decreasing the channel height because of the reduction of drag adjacent to the wall. *n-ZnO* Cassie surface shows the largest reduction due to the dewetted nature.



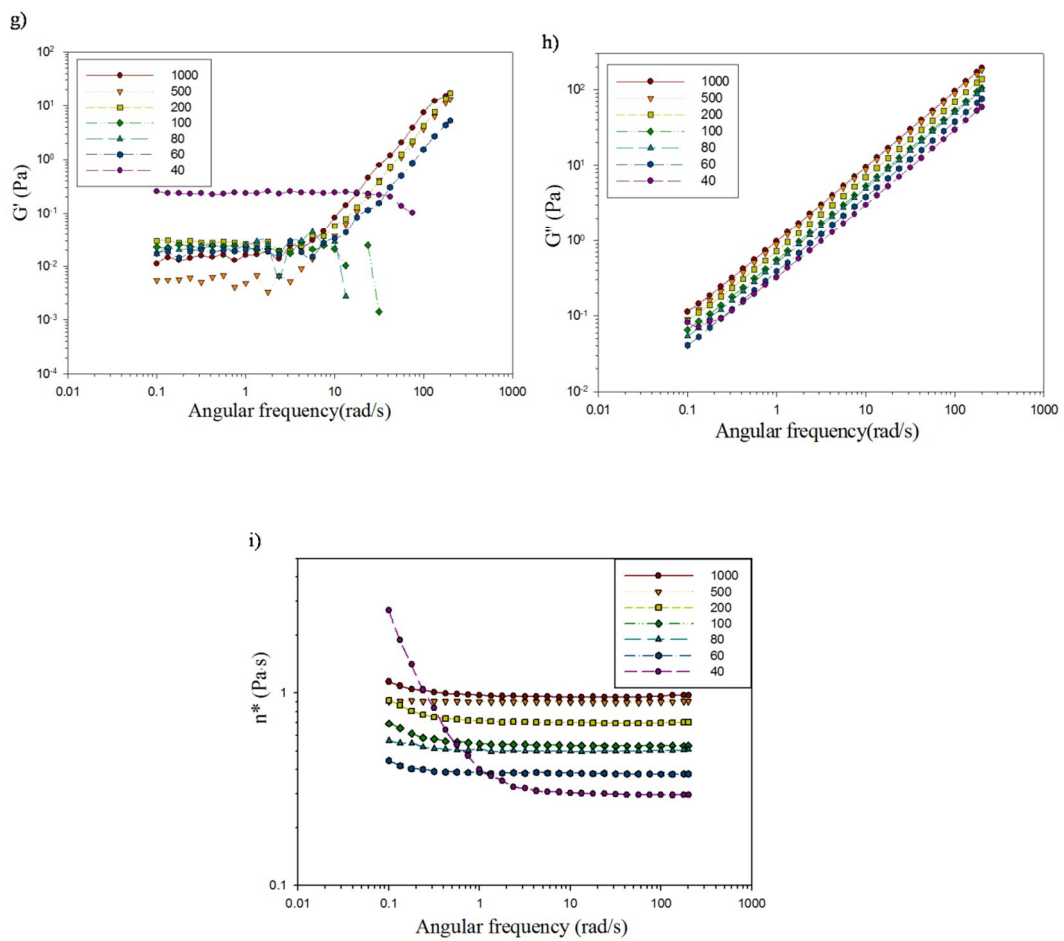


Figure 2.13. Oscillatory data of storage modulus (G'), loss modulus (G''), and complex viscosity (n^*) in frequency sweep modes: (a) ~ (c) smooth surface, (d) ~ (f) hydrophobic surface, and (g) ~(i) n -ZnO Cassie surface.

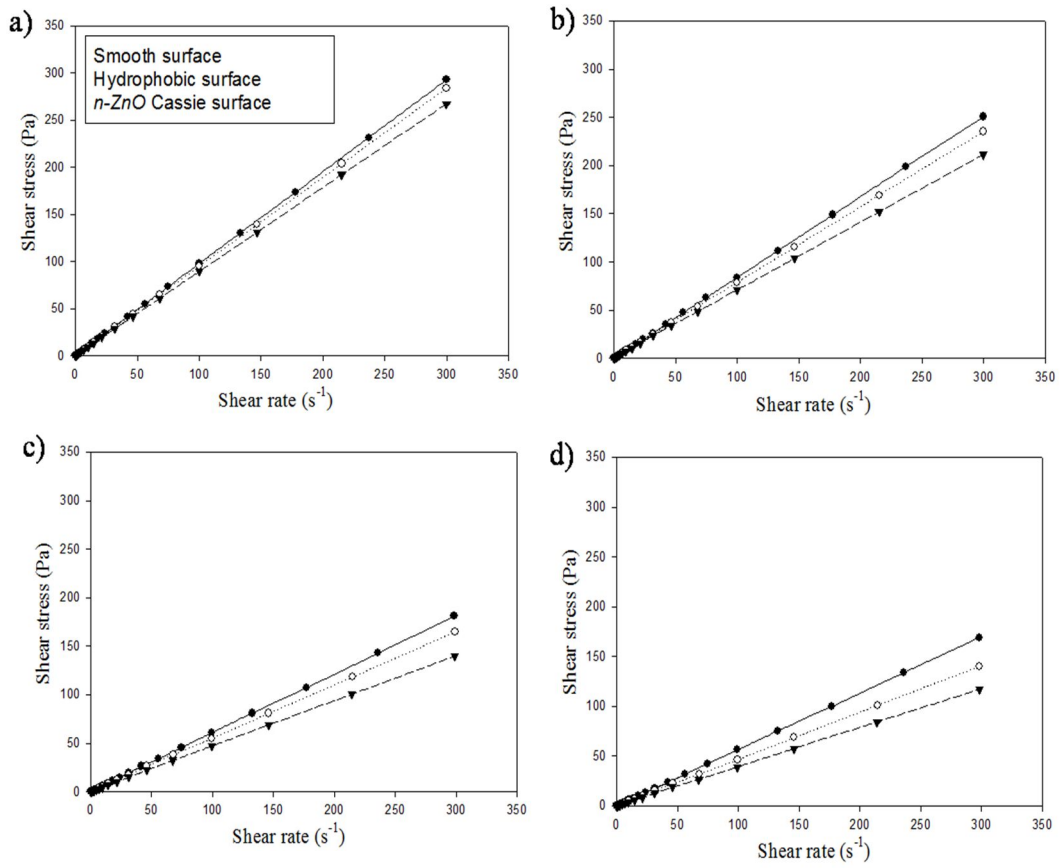


Figure 2.14. Shear stress VS shear rate with respect to the channel height: (a) 500 μm , (b) 200 μm , (c) 80 μm , and (d) 60 μm .

2.7. References

- [1] Rothstein JP. Slip on superhydrophobic surfaces. *Annu Rev Fluid Mech.* 2010;42:89-109.
- [2] Migler KB, Hervet H, Leger L. Slip transition of a polymer melt under shear stress. *Phys Rev Lett.* 1993;70:287-90.
- [3] Zhu Y, Granick S. Rate-dependent slip of Newtonian liquid at smooth surfaces. *Phys Rev Lett.* 2001;87:096105-1-3.
- [4] Sbragaglia M, Prosperetti A. A note on the effective slip properties for microchannel flows with ultrahydrophobic surfaces. *Phys Fluids.* 2007;19:043603-1-8.
- [5] Majumder M, Chopra N, Andrews R, Hinds BJ. Nanoscale hydrodynamics - Enhanced flow in carbon nanotubes. *Nature.* 2005;438:44-.
- [6] Blake TD. Slip between a Liquid and a Solid - Tolstoi,D.M. (1952) Theory Reconsidered. *Colloid Surface.* 1990;47:135-45.
- [7] Cho JHJ, Law BM, Rieutord F. Dipole-dependent slip of Newtonian liquids at smooth solid hydrophobic surfaces. *Phys Rev Lett.* 2004;92.
- [8] Ruckenstein E, Rajora P. On the No-Slip Boundary-Condition of Hydrodynamics. *J Colloid Interf Sci.* 1983;96:488-91.
- [9] Tretheway DC, Meinhart CD. Apparent fluid slip at hydrophobic microchannel walls. *Phys Fluids.* 2002;14:L9-L12.
- [10] de Gennes PG. On fluid/wall slippage. *Langmuir.* 2002;18:3413-4.
- [11] Alexeyev AA, Vinogradova OI. Flow of a liquid in a nonuniformly hydrophobized capillary. *Colloids Surf A.* 1996;108:173-9.
- [12] Schowalter WR. The Behavior of Complex Fluids at Solid Boundaries. *J Non-Newton Fluid.* 1988;29:25-36.
- [13] Dongari N, Sharma A, Durst F. Pressure-driven diffusive gas flows in microchannels: from the Knudsen to the continuum regimes. *Microfluid Nanofluid.* 2009;6:679-92.
- [14] Brenner H. Fluid mechanics revisited. *Physica A.* 2006;370:190-224.
- [15] Choi CH, Westin KJA, Breuer KS. Apparent slip flows in hydrophilic and

- hydrophobic microchannels. *Phys Fluids*. 2003;15:2897-902.
- [16] Whitby M, Cagnon L, Thanou M, Quirke N. Enhanced fluid flow through nanoscale carbon pipes. *Nano Lett*. 2008;8:2632-7.
- [17] Thompson PA, Troian SM. A general boundary condition for liquid flow at solid surfaces. *Nature*. 1997;389:360-2.
- [18] Laun HM, Rady M, Hassager O. Analytical solutions for squeeze flow with partial wall slip. *J Non-Newton Fluid*. 1999;81:1-15.
- [19] Yang SP, Zhu KQ. Analytical solutions for squeeze flow of Bingham fluid with Navier slip condition. *J Non-Newton Fluid*. 2006;138:173-80.
- [20] Cieplak M, Koplik J, Banavar JR. Boundary conditions at a fluid-solid interface. *Phys Rev Lett*. 2001;86:803-6.
- [21] Pit R, Hervet H, Leger L. Direct experimental evidence of slip in hexadecane: Solid interfaces. *Phys Rev Lett*. 2000;85:980-3.
- [22] Watanabe K, Yanuar, Udagawa H. Drag reduction of Newtonian fluid in a circular pipe with a highly water-repellent wall. *J Fluid Mech*. 1999;381:225-38.
- [23] Choi CH, Kim CJ. Large slip of aqueous liquid flow over a nanoengineered superhydrophobic surface. *Phys Rev Lett*. 2006;96.
- [24] Lee C, Choi CH, Kim CJ. Structured surfaces for a giant liquid slip. *Phys Rev Lett*. 2008;101.
- [25] Ybert C, Barentin C, Cottin-Bizonne C, Joseph P, Bocquet L. Achieving large slip with superhydrophobic surfaces: Scaling laws for generic geometries. *Phys Fluids*. 2007;19.
- [26] Baudry J, Charlaix E, Tonck A, Mazuyer D. Experimental evidence for a large slip effect at a nonwetting fluid-solid interface. *Langmuir*. 2001;17:5232-6.
- [27] Barrat JL, Bocquet L. Large slip effect at a nonwetting fluid-solid interface. *Phys Rev Lett*. 1999;82:4671-4.
- [28] Shirtcliffe NJ, McHale G, Newton MI, Chabrol G, Perry CC. Dual-scale roughness produces unusually water-repellent surfaces. *Adv Mater*. 2004;16:1929-+.
- [29] Li W, Amirfazli A. A thermodynamic approach for determining the contact angle hysteresis for superhydrophobic surfaces. *J Colloid Interf Sci*. 2005;292:195-201.

- [30] Han J, Gao W. Surface Wettability of Nanostructured Zinc Oxide Films. *J Electron Mater.* 2009;38:601-8.
- [31] Vayssieres L. Growth of arrayed nanorods and nanowires of ZnO from aqueous solutions. *Adv Mater.* 2003;15:464-6.
- [32] Cottin-Bizonne C, Barrat JL, Bocquet L, Charlaix E. Low-friction flows of liquid at nanopatterned interfaces. *Nat Mater.* 2003;2:237-40.
- [33] Marmur A. Wetting on hydrophobic rough surfaces: To be heterogeneous or not to be? *Langmuir.* 2003;19:8343-8.

III. Superhydrophobicity and Water Droplet Bouncing Phenomena on a Multi-scale Nanostructured Surface

3.1. Introduction

Superhydrophobicity is a distinctive characteristic of surface structure implying extreme water repellency and a contact angle (CA) over 150° . Many researchers have produced biomimetic superhydrophobic surfaces with extremely high water repellency for industrial applications such as self-cleaning windows, windshield, exterior paints, antifouling, roof tiles, and textiles.

One of the simplest ways for introducing superhydrophobicity is to create geometries with vertically aligned pillar textures on a surface, which offers plenty of air pockets between the pillars and maintains the so-called Cassie-Baxter state [1]. Various attempts have been made using nanostructures, such as carbon nanotubes (CNTs) and nanopins. For instance, vertically aligned CNT bundles (ACNT) [2] have shown superhydrophobicity with a CA of 158° , while PAN nanofiber bundles [3] and nanoneedle structures [4] that had much lower densities than ACNT have shown superior superhydrophobicity with CA values of 173° and 178° , respectively. Honeycomb like ACNT [5] with uniform geometry and a very low sliding angle of 3° has also been fabricated. Furthermore, other reports demonstrate that anisotropic dewetting tendency on the surface of a rice leaf can be imitated using the ACNT film and that anisotropic dewetting induced by different roll-off angles with respect to the rolling direction can be manipulated by the microstructural arrangement [6].

Multi-scale structures with microscale and nanoscale regularities, which are similar to downsized fractal structure of microscale structures (*e.g.*, lotus leaf, rose

petal, feather, and butterfly wing), can provide superhydrophobicity by provoking larger CA, smaller contact angle hysteresis (CAH), smaller sliding angle, and higher dynamic bouncing effect due to their structural characteristics. Sun *et al.* fabricated a multi-scale structure of a biomimetic artificial leaf by nanocasting PDMS over the surface of a lotus leaf [7]. Indeed, many other dual-scale hierarchical structures mimicking the lotus leaf topography have been prepared using solvent-induced crystallization of typical polymers [8], solvent etching [9], anodization of fluorinated functional materials [10], 3D microsphere/nanofiber networks [11], self-assembly [12, 13], micropatterning of electrospun mats [14], incorporation of microbeads/nanobeads [15, 16], and nanostructures in a micro-ordered array [17]. The multi-scale structures are full of air pockets due to their structural uniqueness. The air pockets in the hierarchical structure impede the transition from the Cassie-Baxter state to the Wenzel state and improve the morphological stability of a liquid droplet [18]. Consequently, the resulting multi-scale roughness of the hierarchical structure yields extreme superhydrophobicity rather than the single-scale roughness.

From a theoretical perspective, the surface roughness morphology of multi-scale nanostructures consisting of pillars with different height and width is desired not only to maximize CA but also to minimize the free energy barrier (FEB) [18-20]. Furthermore, it makes the superhydrophobic state more stable and thus induces larger self-cleaning effect, higher dynamic bouncing behavior, lower CAH, and smaller sliding angle. The dynamic bouncing effect may depend on the velocity of a dropping liquid, surface roughness morphology, and liquid properties. Compared with references related to the CA, a limited number of studies on the bouncing effect were reported. For example, Jung and Bhushan fabricated various surfaces including flat, nano, micro, and multi-scale structures and proposed a criterion for determining the transition from the Cassie-Baxter regime to the Wenzel regime [21, 22]. In addition, dimensionless numbers such as the Weber number (We), the Reynolds number (Re), and the Capillary number (Ca), have been used as a feasible determinant of whether the liquid droplet would show bouncing, sticking, or spreading behavior [23].

In the current study, two kinds of multi-scale structures were fabricated to

investigate the superhydrophobicity and water bouncing phenomenon: i) incorporation of 20 nm diameter CNT and 250 nm ZnO (CNT/ZnO), and ii) combination of 20 nm diameter ZnO and 150 nm carbon nanofiber (ZnO/CNF). The prepared multi-scale nanostructures [24] were modeled theoretically to predict the CA and CAH through the thermodynamic approach using surface free energy. The numerical results were compared with the experimental results. To the best of our knowledge, this is the first report that elucidates the underlying physics behind the bouncing phenomenon of a water droplet induced by the multi-scale nanostructure with robust theoretical tools such as the free energy barrier (FEB) analysis and the level-set method.

3.2. Theoretical Background

3.2.1. Thermodynamical Approach

The multi-scale hierarchical roughness structure fabricated in this study consisted of two different size pillars, *i.e.*, micropillars and nano-pillars constructed on the base micropillars (Figure 3.3). Thermodynamic analysis was carried out to explain the synergistic effect of the dual-scale roughness structures on CA. For the multi-scale hierarchical system, the corresponding geometrical constitutions and free energy differences are expressed as below [27]:

$$\theta_i \frac{L_i^2}{\sin^2 \theta_i} - \left(L_i^2 \cot \theta_i + (L_i + L_j) \cdot a \sin \theta_p \right) = \theta_j \frac{L_j^2}{\sin^2 \theta_j} - L_j^2 \cot \theta_j \quad (1)$$

$$\Delta F_{i \rightarrow j} / \gamma^{la} = \left(\theta_j \frac{L_j}{\sin \theta_j} - \theta_i \frac{L_i}{\sin \theta_i} \right) + a \cos \theta_y \quad (2)$$

$$\theta_k \frac{L_k^2}{\sin^2 \theta_k} - L_k^2 \cot \theta_k = \theta_j \frac{L_j^2}{\sin^2 \theta_j} - L_j^2 \cot \theta_j \quad (3)$$

$$\Delta F_{j \rightarrow k} / \gamma^{la} = \left(\theta_j \frac{L_j}{\sin \theta_j} - \theta_k \frac{L_k}{\sin \theta_k} \right) + b \quad (4)$$

$$\theta_k \frac{L_k^2}{\sin^2 \theta_k} - L_k^2 \cot \theta_k + (L_k + L_l) \cdot a \sin \theta_p = \theta_l \frac{L_l^2}{\sin^2 \theta_l} - L_l^2 \cot \theta_l \quad (5)$$

$$\Delta F_{k \rightarrow l} / \gamma^{la} = \left(\theta_l \frac{L_l}{\sin \theta_l} - \theta_k \frac{L_k}{\sin \theta_k} \right) + a \cos \theta_Y \quad (6)$$

$$\theta_m \frac{L_m^2}{\sin^2 \theta_m} - L_m^2 \cot \theta_m = \theta_l \frac{L_l^2}{\sin^2 \theta_l} - L_l^2 \cot \theta_l \quad (7)$$

$$\Delta F_{l \rightarrow m} / \gamma^{la} = \left(\theta_l \frac{L_l}{\sin \theta_l} - \theta_m \frac{L_m}{\sin \theta_m} \right) + d \quad (8)$$

where θ_Y is Young's CA, θ_p is the angle between the two nano-pillars, and the subscripts stand for the location of the droplet (Figure 3.4). Here, a , b , and d are the width of the nano-pillar, the interspacing between the nano-pillars, and the interspacing between the micro-pillars, respectively. For a graphite sheet [28] and a flat ZnO film [29], CAs are 98.3° and 100° , respectively. Eqs. 1, 3, 5, and 7 were derived by considering the geometrical constitution of the multi-scale hierarchical nanostructure. When the edge of the meniscus of a water droplet moves from position i to j , the free energy (FE) difference is given by eq. 2. The two FEs at each position characterized by surface tension and arc-length of the meniscus are $F_i = \gamma^{la} l_i^{la} + \gamma^{ls} l_i^{ls} + C$ and $F_j = \gamma^{la} l_j^{la} + \gamma^{sa} l_j^{sa} + C$, where C is the FE portion that remains unchanged during the calculation. The FE differences from position j to k , k to l , and l to m were derived in a similar fashion. Eqs. 2, 4, 6, and 8 were used repeatedly to calculate the FE barriers and the equilibrated CA (ECA).

3.2.2. Numerical Simulation

In a bid to simulate the dynamic behavior of a water droplet the Level-Set method that describes the motion of an interface between air and water is coupled with the momentum equation. Here, we assume that the liquid is incompressible and Newtonian fluid, the classical Navier-Stokes equation is coupled with the Level-Set

equation. The conservation of mass, level set function and the Navier-Stokes function are as follows:

$$\nabla \cdot \mathbf{v} = 0 \quad (9)$$

$$\frac{\partial \phi}{\partial t} + u \nabla \phi = \gamma \nabla \left[\varepsilon \nabla \phi - \phi (1 - \phi) \cdot \mathbf{n} \right] \quad (10)$$

$$\rho \frac{D\mathbf{v}}{Dt} = \rho \mathbf{g} + \mu \nabla^2 \mathbf{v} + \nabla p + F_{st} \quad (11)$$

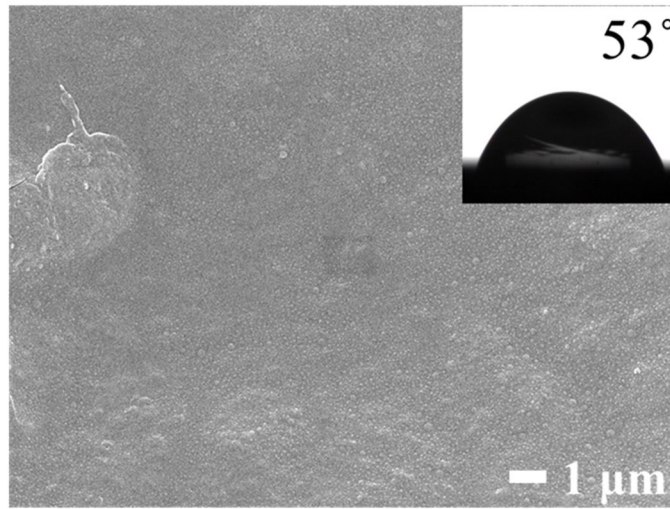
ρ is the density, \mathbf{g} is the gravity, μ is the dynamic viscosity, \mathbf{v} represents the velocity, p denotes the pressure, ϕ defines the interface where ϕ equals 0 in air and 1 in water. γ represents the amount of re-initialization and ε defines the parameter controlling interface thickness. F_{st} is the surface force computed as $F_{st} = \nabla \cdot (\sigma (I - (\mathbf{n}\mathbf{n}^T)) \delta)$ where I , \mathbf{n} , σ , and δ are the identity matrix, normal vector to the interface, surface tension coefficient, and Dirac delta function that is nonzero at the water-air interface, respectively. The density and viscosity jump across the interface so that those are expressed using the level set function as $\rho = \rho_{air} + (\rho_{water} - \rho_{air})\phi$ and $\mu = \mu_{air} + (\mu_{water} - \mu_{air})\phi$. During the simulation for dropping a droplet with volume of 30 μL into an air region, an initial inlet velocity is set at 0.5 m/s, and smoothly reduced to zero after generating one water droplet as manipulating the inlet velocity with respect to elapsed time.

3.3. Experimental Section

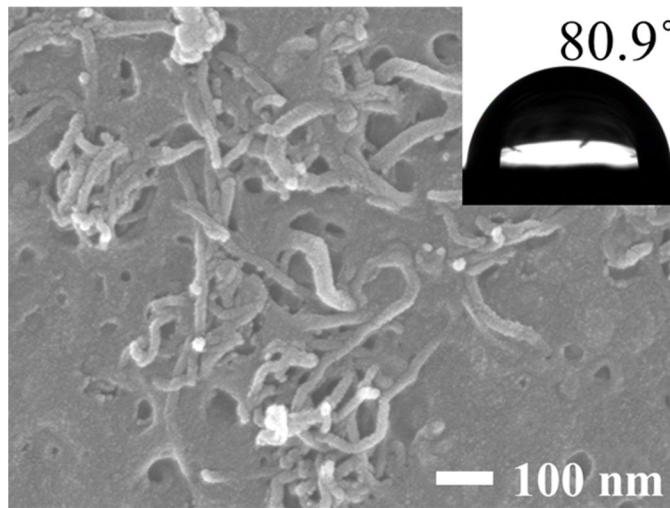
3.3.1. Fabrication of CNT/Polymer Nanocomposites

A pure LCP surface was firstly produced to compare contact angles between the flat and CNT nanostructured surfaces. 1wt % and 3wt % filled CNT/Polymer mixtures were made by extruding method for better dispersion of CNT and then

pressed under high pressure (10 Ton) and high temperature at 190 °C. Here, we used Multi-Wall Carbon Nanotube (MWCNT, Carbon nanotech Co., Korea) and Poly(lactic acid) (PLA, 4032D, Natureworks LLC, USA) as a polymer matrix. Then, the nanocomposites were immersed in tetrahydrofuran (THF) for solvent etching with sonication for 5 min and rinsed out with pure water to generate CNT protrusion for generating nanoscale surface roughness.

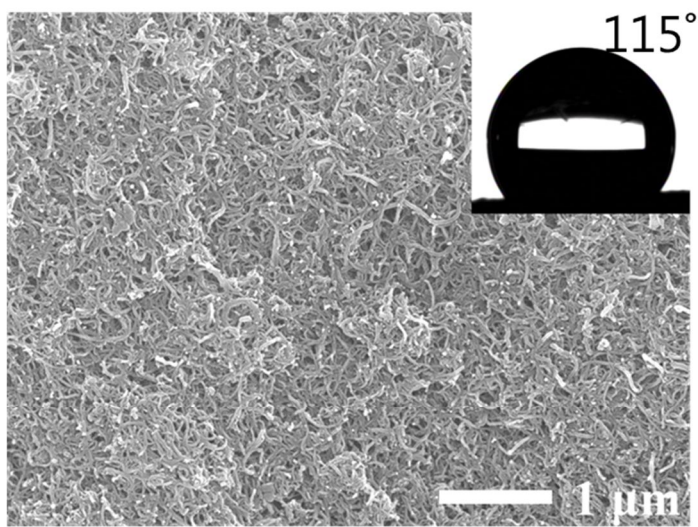


(a)

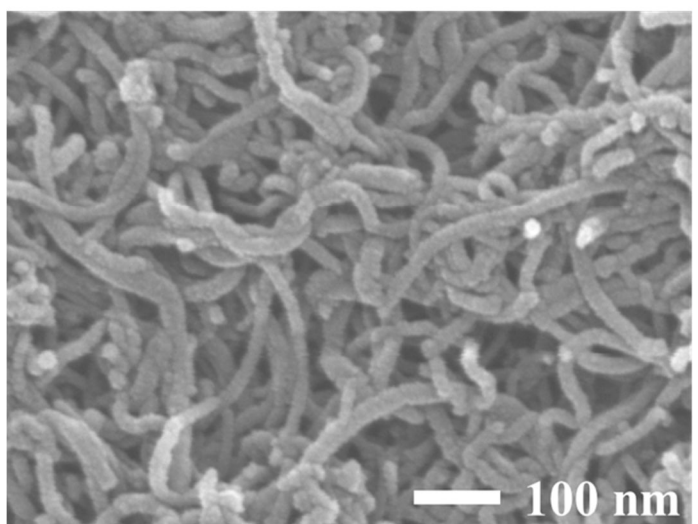


(b)

Figure 3.1. Fabrication of CNT/Polymer nanocomposites. (a) pure PLA, (b) 1wt % filled composite, (c) 3wt % filled composite, and (d) a magnified view of (c).



(c)



(d)

Figure 3.1. (Continued.)

3.3.2. Self-assembly of single-scale Nanostructures

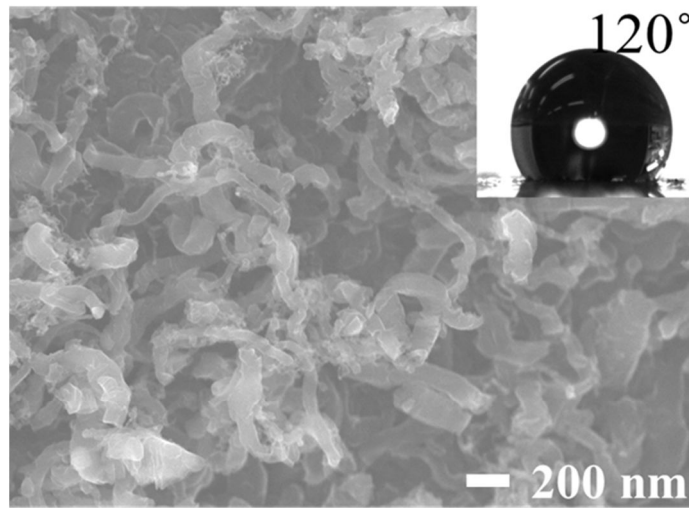
ZnO nanorods were grown on p-type Si (100) substrates using the hydrothermal method [36]. The Si substrates were cleaned by soaking in the solution ($\text{H}_2\text{SO}_4:\text{H}_2\text{O}_2 = 4:1$) at 110 °C for 15 min and then in DI water for 5 min. ZnO seed nuclei for the growth of ZnO nanorods were prepared in 30 mM zinc acetate [$\text{Zn}(\text{C}_2\text{H}_3\text{O}_2)_2$] ethanol solution at 90 °C for 15 min. The solution was then spin coated onto the Si substrates at 1500 rpm for 60 s. Subsequently, the seed coated substrates were thermally annealed at 100 °C for 5 min for removal of the residual solvent. In this stage, the generated ZnO did not grow into the form of nanorods but it rather existed as a nucleus for growth of the ZnO nanorods. For the main growth, the Si substrates were immersed in aqueous solution consisting of 25 mM zinc nitrate hexahydrate [$\text{Zn}(\text{NO}_3)_2 \cdot 6\text{H}_2\text{O}$], 25 mM hexamethylenetetramine [$\text{C}_6\text{H}_{12}\text{N}_4$] (HMT), and DI water. The main growth of the ZnO nanorods occurred at 90 °C for 60 min.

3.3.3. Self-assembly of multi-scale Nanostructures

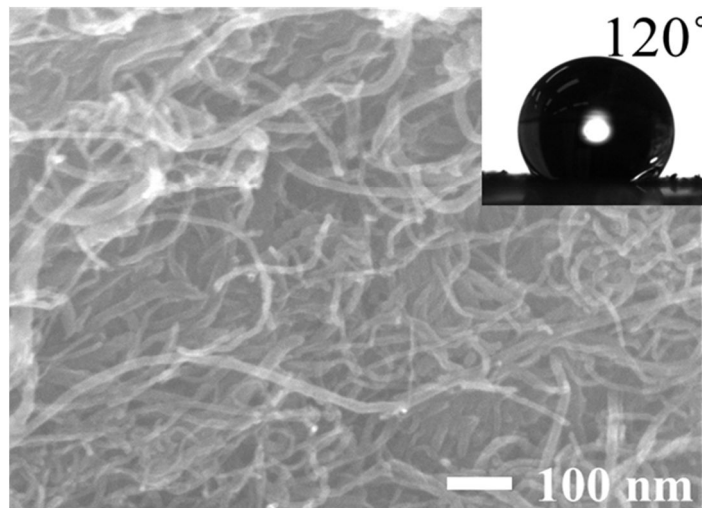
Prepared CNF and CNT were used as a platform for the growth of ZnO nanorods. ZnO seed nuclei for ZnO nanorod growth were prepared in 30 mM zinc acetate [$\text{Zn}(\text{C}_2\text{H}_3\text{O}_2)_2$] ethanol solution at 90 °C for 15 min. The CNF and CNT were then immersed in the seed solution and the seed coated CNF and CNT were annealed at 300 °C for 5 min. After ZnO seed formation, ZnO nanorods were formed by the continuous supply of zinc ions and hydroxyl radicals in the aqueous solution consisting of 25 mM zinc nitrate hexahydrate [$\text{Zn}(\text{NO}_3)_2 \cdot 6\text{H}_2\text{O}$], 25 mM HMT, and DI water. The main growth of the ZnO nanorods was carried out at 90 °C for 30 min for CNF and 60 min for CNT. After the growth procedure, the aqueous solution including the grown ZnO nanorods was filtered using a micro filter paper (pore size, 1 μm). Finally, the CNF and CNT with ZnO nanorods were collected on the micro filter paper and dried at 40 °C for several hours in air.

3.3.4. CA and CAH measurements

The sessile drop method was used to measure a contact angle depending on various single- and multi-scaled surfaces. The angle formed between the liquid/vapor interface and the liquid/solid interface is the contact angle. A contact angle goniometer with high resolution camera and software were employed to capture and analyze the contact angle.

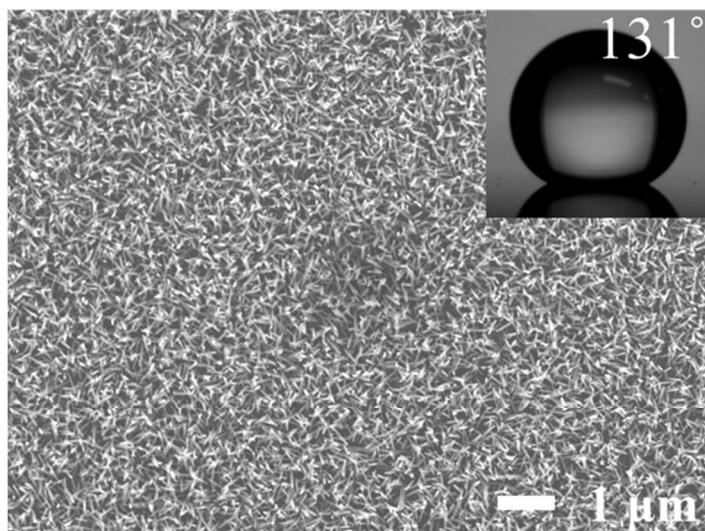


(a)

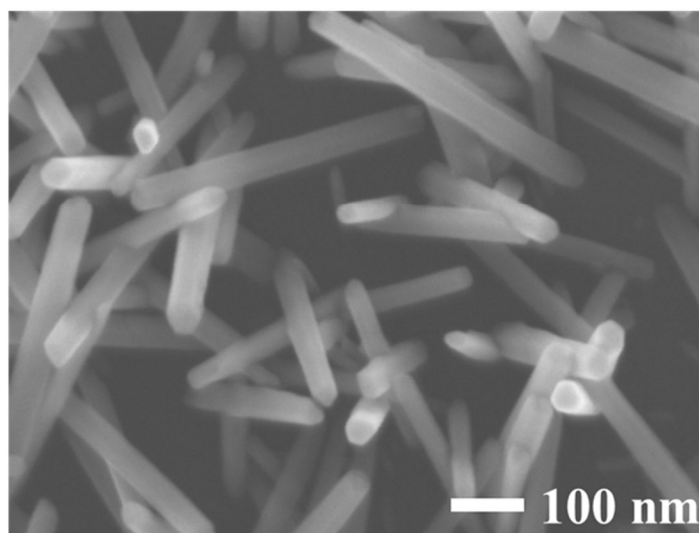


(b)

Figure 3.2. Single-scale surface morphology of (a) CNF forest, (b) CNT forest, (c) ZnO nano-pillars, and (d) enlarged view of the ZnO nano-pillars. Each system displays high hydrophobicity with the contact angle of 120°, 120°, and 131°, respectively.

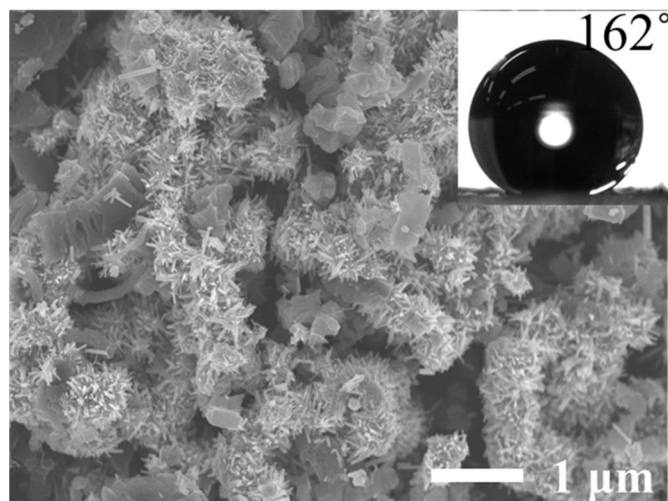


(c)

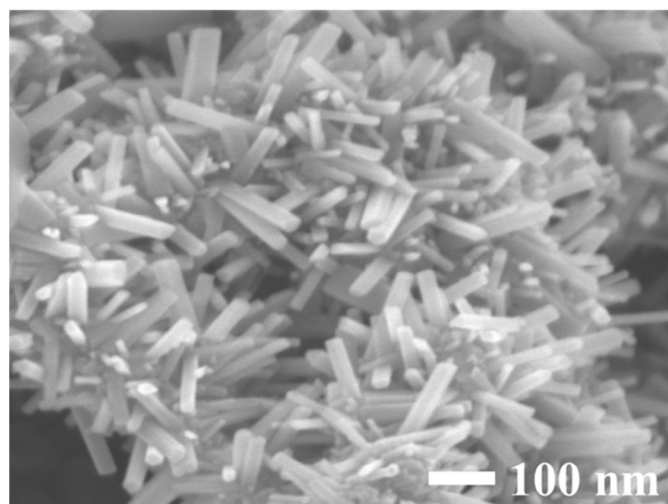


(d)

Figure 3.2. (Continued.)

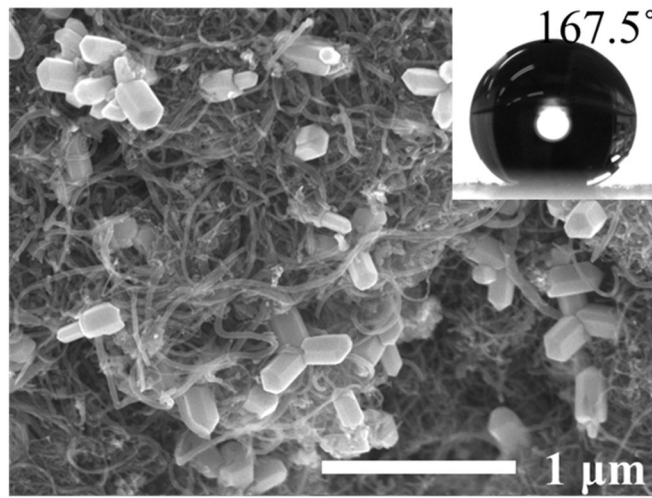


(a)

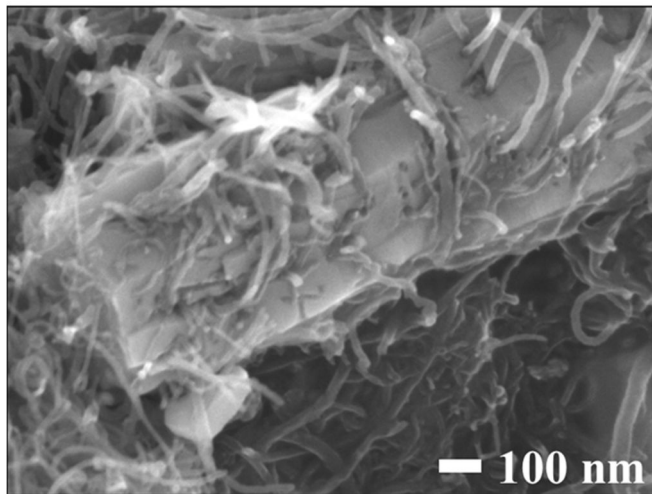


(b)

Figure 3.3. Multi-scale hierarchical nanostructure: (a) ZnO/CNF hierarchical nanostructure showing superhydrophobicity with the contact angle of 162°, (b) enlarged view of the ZnO/CNF in which ZnO nano-pillars are successfully grown onto the CNF, (c) CNT/ZnO hierarchical nanostructure showing higher superhydrophobicity with the contact angle of 167.5°, and (d) enlarged view of the CNT/ZnO in which CNTs are well networked with ZnO.



(c)



(d)

Figure 3.3. (Continued.)

3.4. Results and Discussion

3.4.1. Superhydrophobicity on Various Structures

Many superhydrophobic surfaces in nature show hierarchical structures encompassing several micropattern and nanopattern levels arranged in a tree-like structure. When micropatterns are introduced onto a solid surface, single-scale microroughness structure is generated due to the uniformity and regularity of the patterns, which contributes to a transition from the hydrophilic state to the hydrophobic one. When a solid-air interface exists due to air pockets under a liquid droplet, CA increases because the air pockets act as air cushions, and thereby the Cassie-Baxter regime [1] is generated. It should be noted that a liquid droplet in contact with a surface possessing microroughness may not be able to maintain the Cassie-Baxter state because the single-scale microroughness morphology is more susceptible to liquid intrusion than hierarchical structures [18]. Recent studies prove that hierarchical structures with multi-scale roughness morphology have improved the liquid stability and superhydrophobicity [18-20].

The present study has focused both on the hydrophobic nature of single-scale surface structures and on the dual-scale hierarchical structures that have been produced to introduce superhydrophobicity. For the single-scale surface structures, CNT forest, CNF forest, and ZnO pillars were explored, which had CA values of 120°, 120°, and 131°, respectively (see Figure 3.2). The high hydrophobicity of the CNT and CNF forests is associated with the nanoscale surface roughness of entangled CNTs and CNFs [25]. As well as the CNT forest, nanocomposites with CNTs protruding from the surface also showed high hydrophobicity, indicating that such CNT nanocomposites can offer hydrophobic surfaces by using a simple etching method (see Figure 3.1). However, such forests and nanocomposites do not show superhydrophobicity due to their non-uniform surface roughness, low air-liquid-surface ratio, and thermodynamically unstable feature (*i.e.*, time-dependent transition from the Cassie-Baxter state to the Wenzel state [21]). Vertically aligned ZnO pillars have larger CA

than either the CNT forest or the CNF forest since much space exists between the aligned ZnO pillars and the space forms air pockets supporting a liquid droplet resulting in highly hydrophobic nature of the surface.

To surpass the hydrophobicity limitation of the single-scale structure, hierarchical structures with a dual-scale of CNT/ZnO or ZnO/CNF were created, and the resulting hydrophobicity was investigated with a theoretical model. Hexagonal ZnO structures with a mean diameter of 20 nm have been fabricated on the CNF using the hydrothermal method. They created additional nanoscale surface roughness generating more air pockets, and subsequently a CA of 162° was obtained (Figures 3.3a and 3.3b). The hierarchical structures can lead to a hierarchical FEB structure, which results in the stable superhydrophobic state [18]. On the other hand, the CNT/ZnO hybrid structure has larger mean diameter (ZnO diameter of about 250 nm) than the ZnO/CNF structure (CNF diameter of about 150 nm) and yields a higher CA of 167.5° (*vs.* 162°). In such hierarchical structure, CNTs are networked with the ZnO pillars (Figures 3.3c and 3.3d). Many analytical approaches have been employed to predict the CA of superhydrophobic surfaces with single or multi-scale roughness structures [19-21, 26]. For instance, the fractal formula can be used to analyze the CA of multi-scale hierarchical structures [24] based on the fact that the hierarchical structures mimicking the lotus leaf have characteristics similar to that of the Koch curve in fractal geometry.

From the thermodynamical analysis, it is noticed that the dual-scale hierarchical structure has lower normalized free energy than the single-scale structure (Figure 3.5a). The single-scale structure has the fluctuated high free energy barrier (FEB), indicating that it is not easy to yield high CA (see the inset graph). On the other hand, the dual-scale structure shows the low FEB and the minimum FE is found at the CA over 150° , meaning high CA. The receding and advancing FEBs can give a complementary explanation on the results of the free energy of the single-scale and dual-scale structures (Figure 3.5b). The single-scale structure has monotonous variations in both of receding and advancing FEBs and the receding FEB rises rapidly. However, the dual-scale structure shows large fluctuations in both FEBs and the receding FEB of the

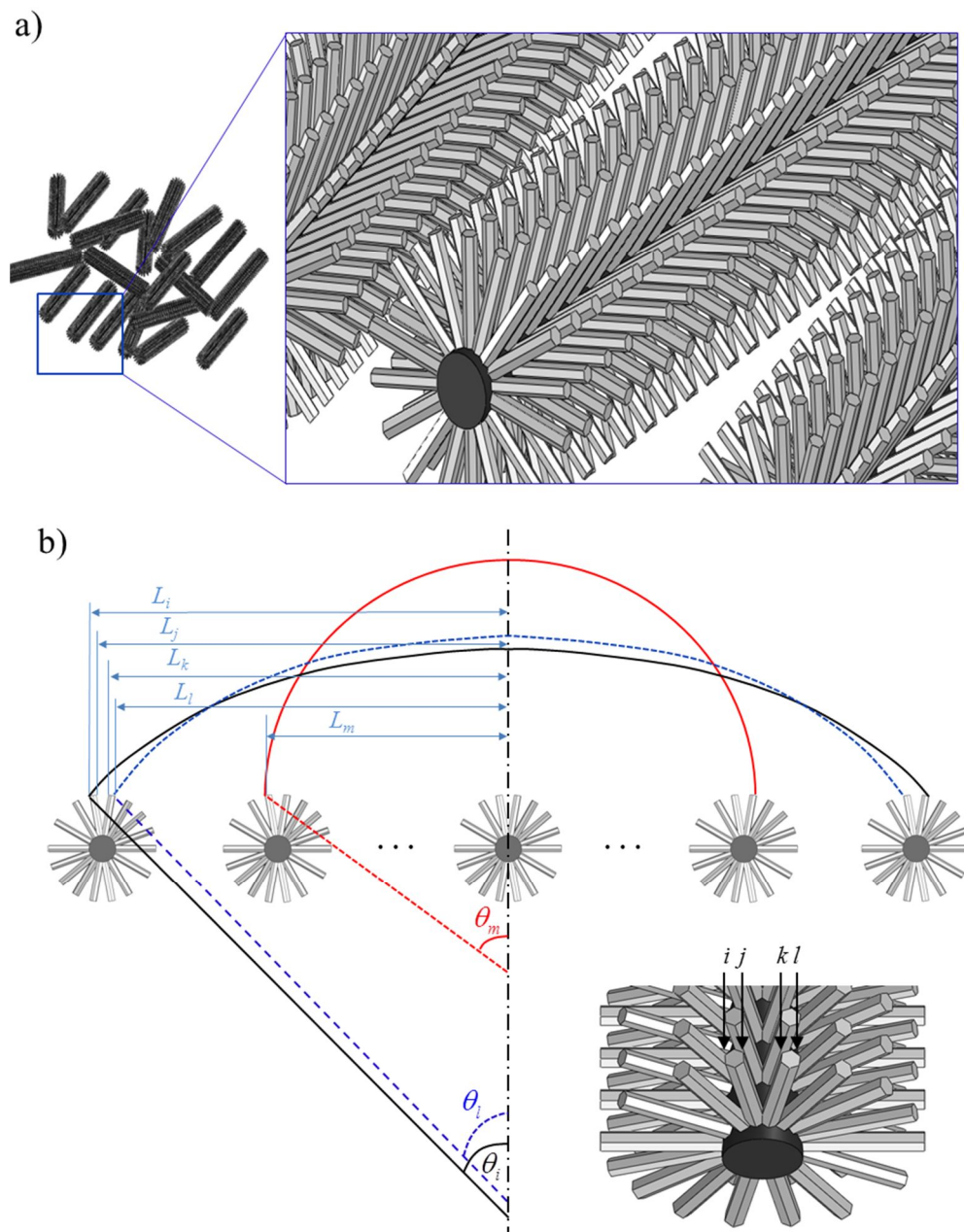


Figure 3.4. (a) Schematic illustration of the multi-scale hierarchical system prepared in this study and (b) Schematic cross-sectional configuration of a liquid droplet on the system.

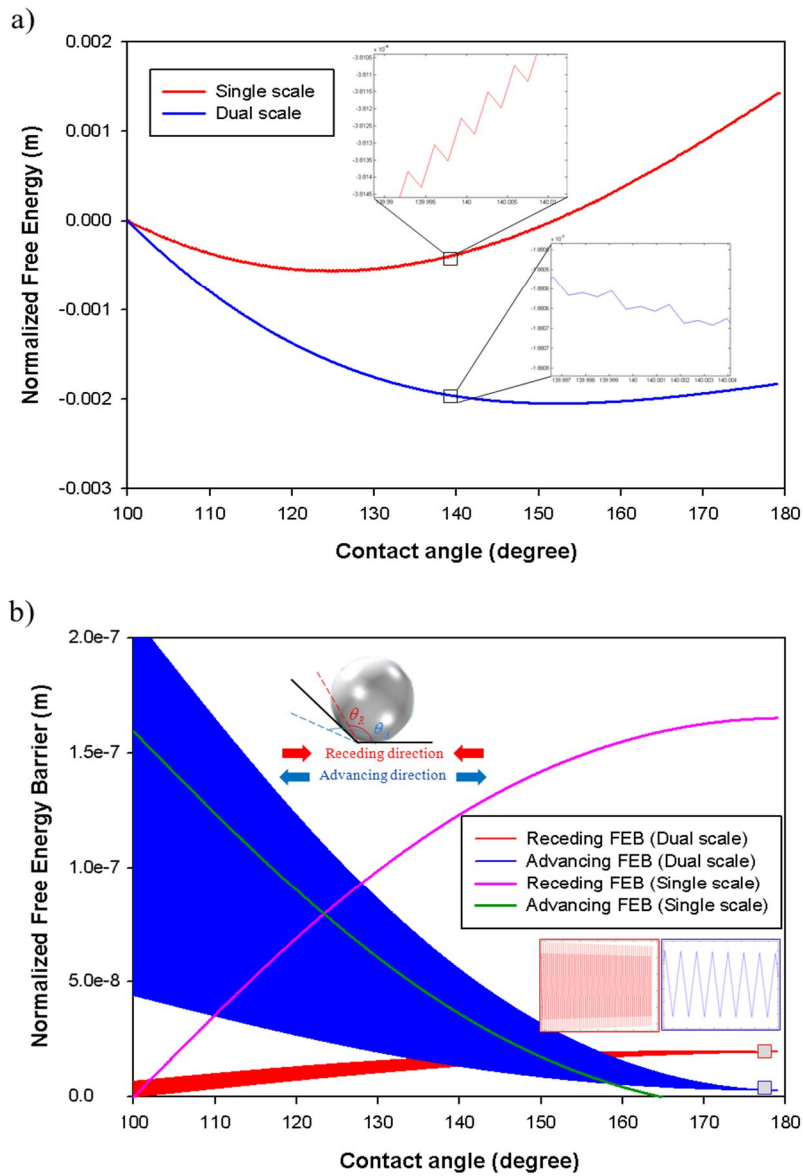


Figure 3.5. (a) Normalized Free Energy (FE) of the single-scale and dual-scale structures. The enlarged graphs show the variation in the local energy barriers indicating metastable and unstable regions. (b) Normalized receding and advancing Free Energy Barriers (FEB) of the single-scale and dual-scale structures. The insets are the enlarged normalized free energy barriers (FEB).

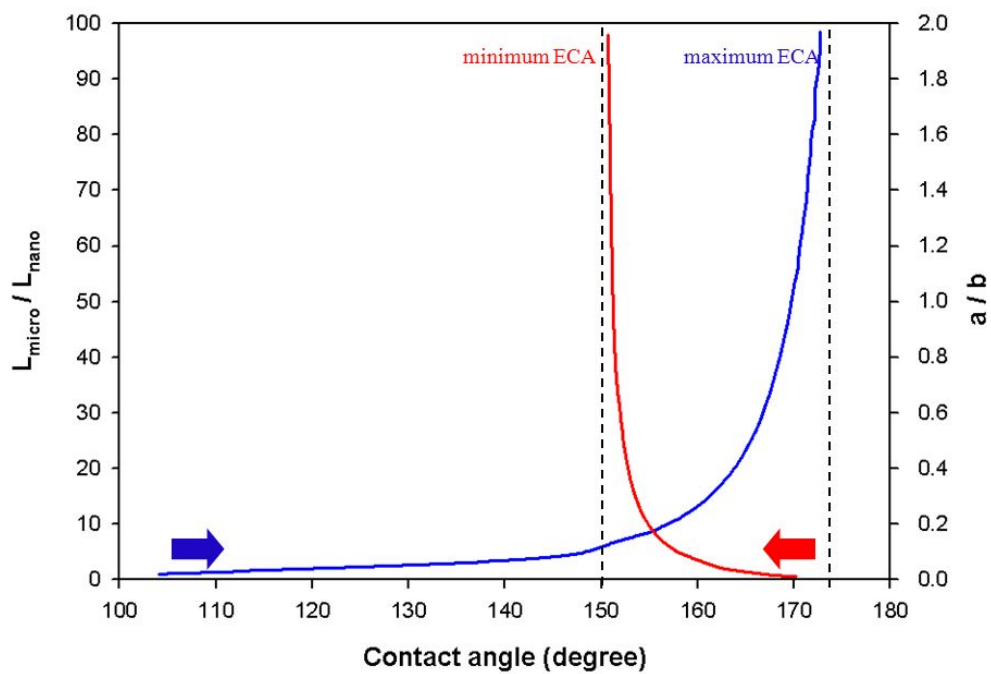


Figure 3.6. Contact angle as a function of the ratio between micro-pillar size and nano-pillar size and the density of nano-pillars on the micro-pillar. The region between the two dashed lines represents ECAs obtainable in this system.

dual-scale structure is much smaller than that of the single-scale structure. Such a small receding FEB is the reason for the increase in the ECA of the dual-scale structure.

The synergistic interaction between nanoscale and microscale structures leads to an increase in the ECA. The multi-scale hierarchical system can solely have superhydrophobic nature with a maximum ECA of 175° and a minimum ECA of 150° (Figure 3.6). When the nanostructure is downsized, the resulting ECA is increased. Both of the nanostructure size and the pillar gap are important for obtaining high ECA. The existence of nanostructure is an indispensable requisite for high ECA. This theoretical interpretation will be helpful in designing superhydrophobic multi-scale hierarchical surfaces in more systematic manner.

3.4.2. Water Droplet Bouncing Phenomenon

When a liquid droplet collides with a solid surface, it can exhibit bouncing, sticking, spreading, or pinning behaviors [30]. These behaviors vary according to the roughness and chemical composition of the solid surface and are also affected by such properties of the droplet as velocity, viscosity, and density [31]. For instance, depending on the droplet velocity, the behavior can be classified into three distinct regimes: non-bouncing regime due to low kinetic energy, bouncing regime following the Cassie-Baxter prediction, and sticky regime in which “touch-down” scenario may be achieved above a critical velocity [32]. Jung and Bhushan stated that the droplet velocity should be smaller than the critical velocity in order to develop a heterogeneous interface and water bouncing (*i.e.*, $V < \text{func}(\gamma_{LV}, H, 1/D)$, where H is the pillar height, and D is the distance between pillars [21]). In all our experiments, each falling droplet had identical kinetic energy because the droplet velocity and droplet volume were fixed. Nevertheless, different dynamic behaviors were observed, including sticking phenomenon in the case of CNT and CNF forests and bouncing behavior over the CNT/ZnO and ZnO/CNF hybrid structures (Figure 3.9). Dimensionless numbers, We ($We = \rho R V^2 / \gamma_{LV}$) and Ca ($Ca = \mu V / \gamma_{LV}$), have been employed by other researchers [23] to understand the correlation among the three regimes aforementioned.

However, these numbers are not appropriate to describe different behavior in the regimes where identical dimensionless numbers are obtained due to the same droplet velocity V and liquid properties (ρ , γ_{LV} , μ), *i.e.*, no variation is expected in the dynamic behavior of the droplet. Therefore, effects of the different surface roughness structures on the liquid bouncing even with the same We and Ca values need to be explained through a new approach like numerical simulation. Such liquid bouncing takes place due to small dissipation of the kinetic energy of the droplet [33]. In this case, the kinetic energy can be transferred to the surface energy, and higher CA induces bouncing off like a solid springback.

The fundamental mechanism of liquid bouncing has yet to be fully understood because many factors are involved in it. In the present study, the threshold of FEB is adopted to explain the energy dissipation and surface energy conservation of a droplet on single-scale and multi-scale nanostructures, and the resulting bouncing phenomenon due to the conserved surface energy is confirmed by the numerical analysis. The kinetic energy of a liquid droplet is converted into the surface energy and dissipation energy when the liquid droplet bounces off the surface. The dissipation energy is determined by the surface geometry. For example, a low FEB can cause the dissipation energy of a droplet to decrease during deformation on the surface, and thus much of the kinetic energy is transferred into the surface energy. In this sense, the bouncing phenomenon on the multi-scale hierarchical nanostructures can occur. On the other hand, the single-scale nanostructure has the similar advancing FEB but much higher receding FEB than the multi-scale hierarchical nanostructure, which causes high energy dissipation and water sticking rather than bouncing (Figure 3.9). This FEB characteristics can also be found as the entire system is downsized. Both of the advancing FEB and receding FEB decrease with the system size (Figure 3.7). The decrease in the FEB threshold makes it easier for a droplet to move towards advancing and receding directions, which decreases the energy dissipation significantly. In addition, CAH can be determined from the difference between the CAs of advancing FEB and receding FEB [27]. This is the maximum CAH where the vibrational energy

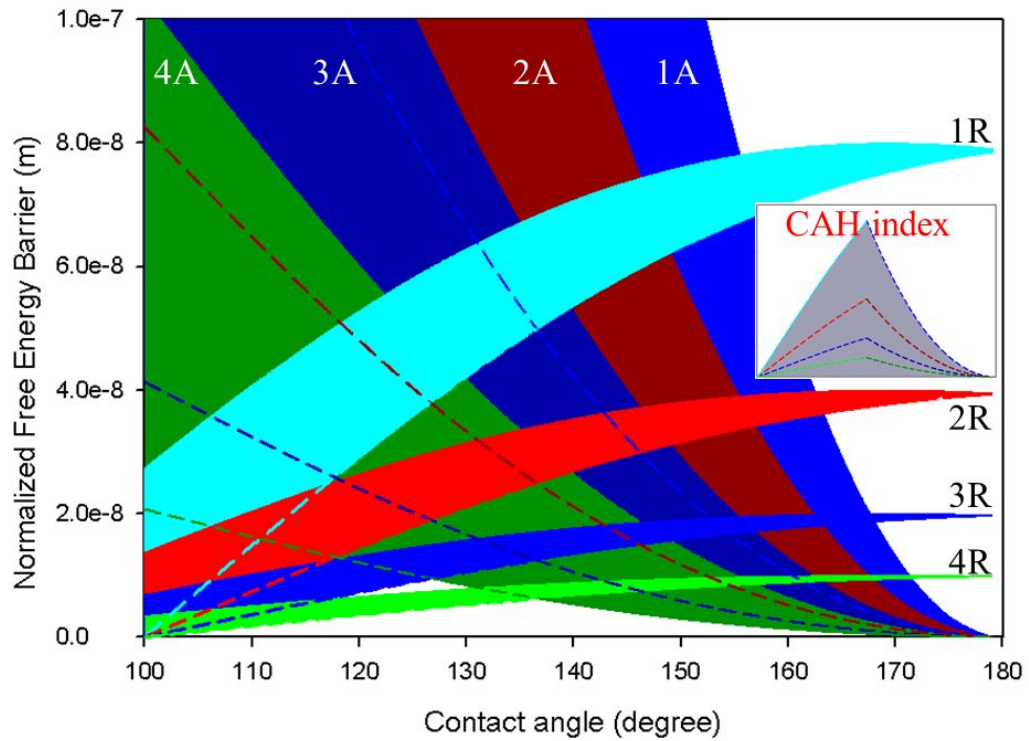


Figure 3.7. Normalized FEB as a function of system sizes; $a:b:d = 80:200:1000 \text{ nm}$ (1A and 1R), $40:100:500 \text{ nm}$ (2A and 2R), $20:50:250 \text{ nm}$ (3A and 3R), and $10:25:125 \text{ nm}$ (4A and 4R). The shaded regions in the inset graph indicate the CAH index proposed in this study.

of a system is ignored. However, since real systems possess non-zero vibrational energy during experiments, the presence of vibrational energy yields low CAH. Furthermore, now that the vibrational energy is not measurable, CAH cannot be determined quantitatively. Please note that the three intersecting curves, *i.e.*, the advancing FEB curve, receding FEB curve, and x-axis form the shaded regions (see the inset graph). Here, we introduce a new physical parameter, “the CAH index” that indicates the area of the shaded region. The CAH index can help one understand the CAH characteristics of a complicated surface structure by providing more quantitative information, even in the case where vibrational energy is not known. The CAH and sliding angles of the dual-scale hierarchical nanostructures are lower than those of the single-scale nanostructures (Figure 3.10). The results demonstrate that the surface morphology can also affect the dynamic motion of a liquid droplet. Additionally, a negligible difference was found in either the CAs or the CAHs measured between before and after the hydrophobic coating. This may be because the superhydrophobicity is determined mainly by the physical surface morphology but not by the chemical composition of the surface, especially in case of the Cassie (composite) state [34].

The liquid droplet bouncing from the hierarchical surface was also demonstrated by FE simulation using the level set method. The simulation procedure was explained in detail in the supplementary information. As illustrated by the experimental and simulation results, the liquid droplet with a CA of 120° does not bounce off, but it undergoes sticking and shaking motions (Figures 3.9a-3.9c). When the CA is small enough, the energy dissipation due to the viscous nature of the liquid droplet becomes large and the energy transfer to the surface energy is minimized. Consequently, sticking occurs rather than bouncing off. On the contrary, the liquid droplet can bounce off as the CA increases since its kinetic energy is conserved by the surface deformation and not dissipated during the impact against the surface (Figures 3.9d-3.9f). These results are also consistent with the results of the thermodynamic analysis presented above. The water droplet behavior is different as inlet velocity of the droplet is varied. When the inlet velocity is higher than free fall motion of the droplet,

it may spread during the colliding with the surface (Figure 3.8a and b).

a)

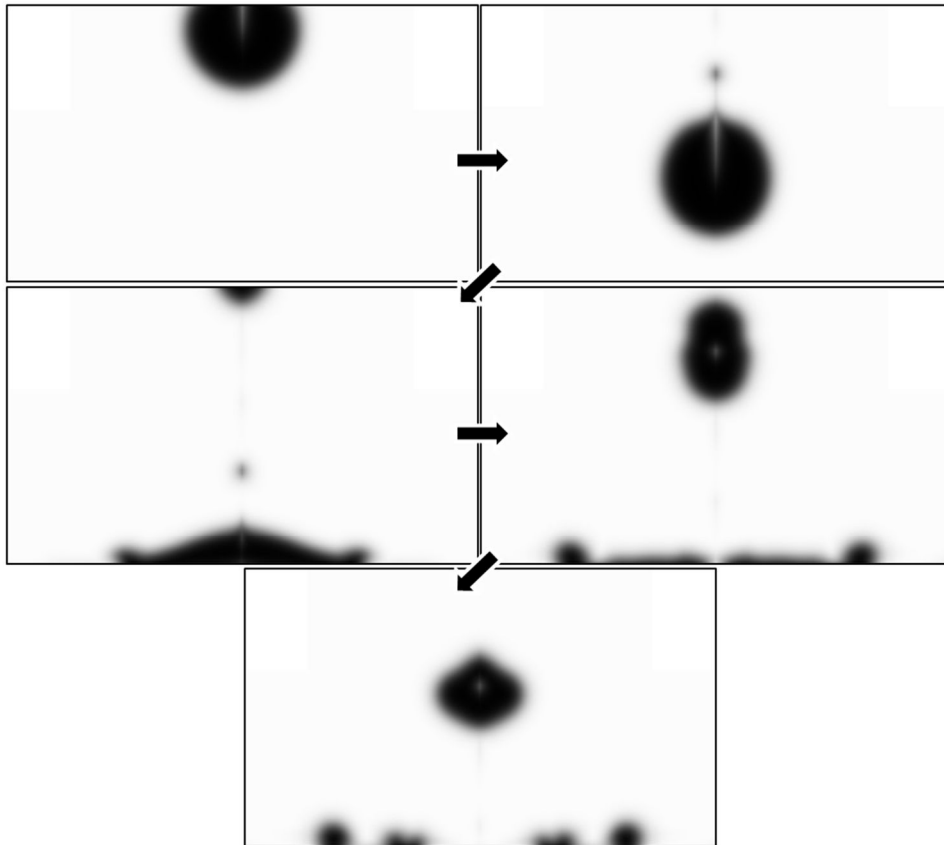


Figure 3.8. Simulation results of distinct dynamic phenomena of a water droplet with different velocity: (a) inlet velocity is 1.25 m/s and (b) inlet velocity is 2.5 m/s.

b)

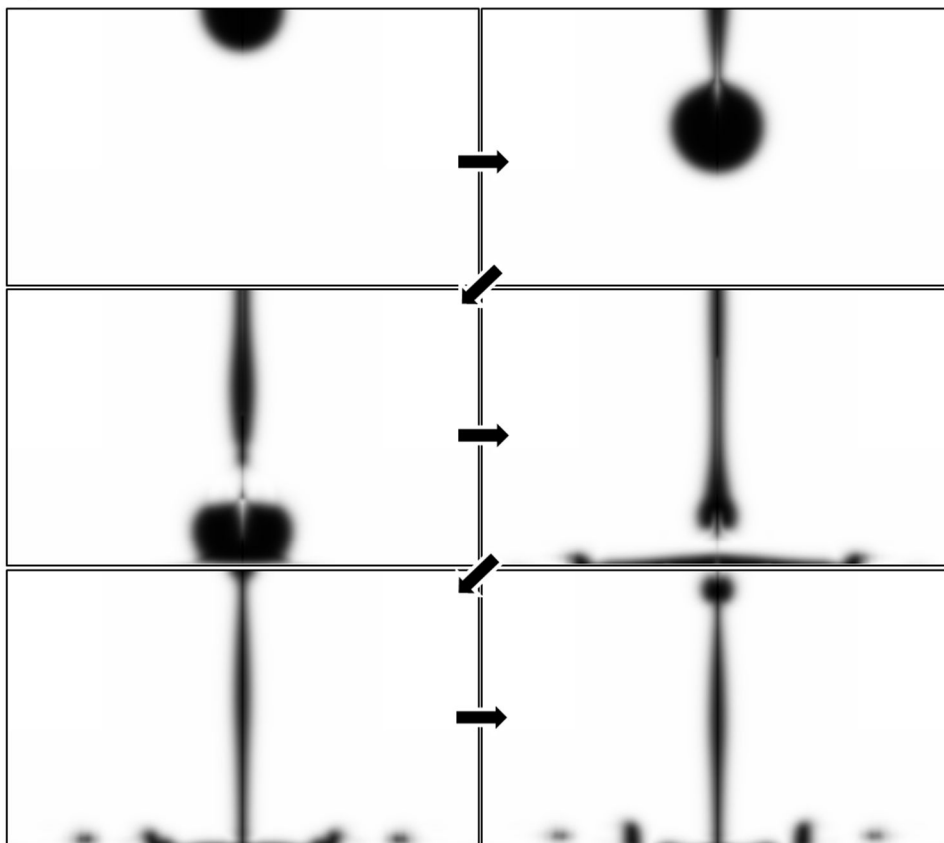


Figure 3.8. (Continued.)

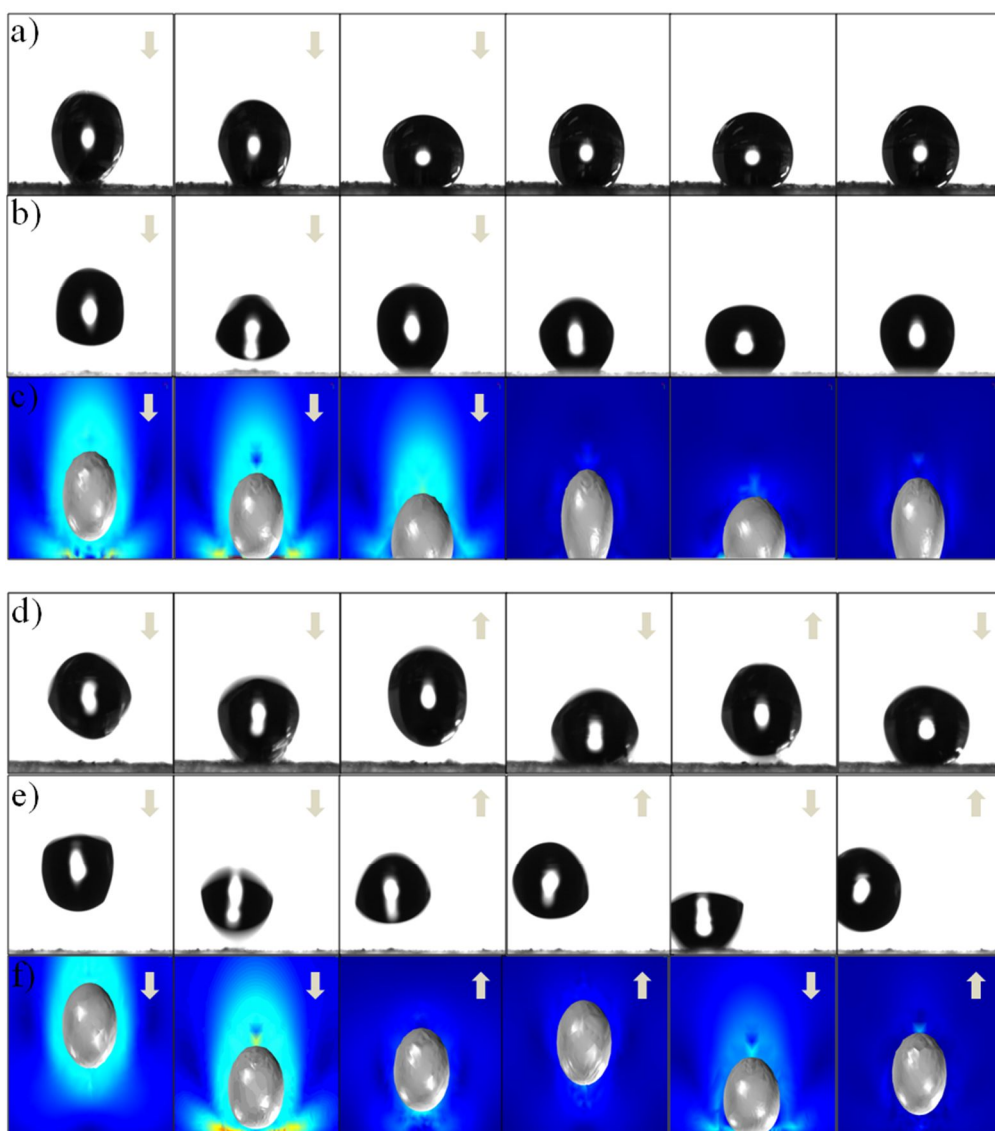


Figure 3.9. Experimental and simulation results of distinct dynamic phenomena of a water droplet: (a) sticking of the droplet on the CNF forest, (b) sticking of the droplet on the CNT forest, (c) simulation results of the sticking droplet with a CA of 120° , (d) bouncing of the droplet over the ZnO/CNF multi-scale hierarchical nanostructure, (e) bouncing of the droplet over the CNT/ZnO multi-scale hierarchical nanostructure, and (f) simulation results of the bouncing droplet with a CA of 165° .

Adhesion, which can explain the bouncing effect quantitatively, is expressed as follows:

$$W_{SL} = \gamma_{LV}(1 + \cos \theta) \quad (12)$$

where W_{SL} is the work of adhesion, and γ_{LV} is the surface tension of the liquid. The work of adhesion increases with decreasing CA. As a result, surfaces with low CA values have better wettability because more energy is dissipated from the inherent kinetic energy during colliding with the solid surface due to the liquid spreading [31].

Overall, the bouncing phenomenon of a liquid droplet can occur when the following conditions are satisfied: i) kinetic energy is transferred to surface energy [35], ii) inherent properties of the liquid droplet, *e.g.*, surface tension, viscosity, and density, are appropriate for the bounce-off regime in the Ca and We correlation [23] and iii) the kinetic energy dissipation is reduced by the superhydrophobic surface with hierarchical structures and stored in the surface deformation instead. A comprehensive understanding of such conditions is critical to materialize various applications such as liquid-repellent windshield, self-cleaning windows and exterior paint, and antifouling agents for roof tiles and textiles.

3.5. Summary

Single nanoscale structures, which show high hydrophobicity with a CA of 120–131°, were constructed with CNT forest, CNF forest, and ZnO pillars. To increase the CA further up to the level of superhydrophobicity, multi-scale hierarchical structures were also prepared with CNT/ZnO and ZnO/CNF, and the resulting superhydrophobicity and dynamic effect (*i.e.*, bouncing effect) were analyzed. It was found that the multi-scale hierarchical structures showed superhydrophobicity with CA values higher than 160° by means of the synergistic interaction of the first-level and the second-level hierarchical structures. The thermodynamic analysis accounted for the

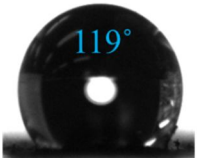
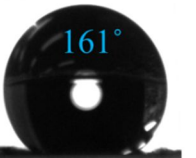
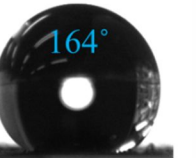
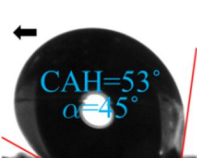
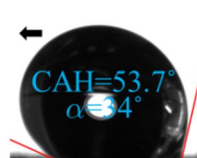
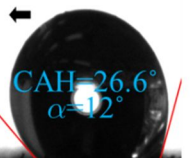
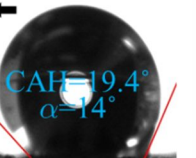
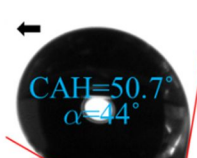
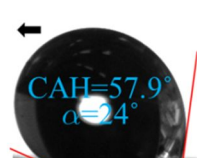
	CNF single-scale nanostructure	CNT single-scale nanostructure	ZnO/CNF dual-scale nanostructure	CNT/ZnO dual-scale nanostructure
Before				
After				
Before				
After				

Figure 3.10. Contact angle (CA), Contact angle Hysteresis (CAH), and sliding angle (α) of single-scale and dual-scale nanostructures before and after SAM treatment.

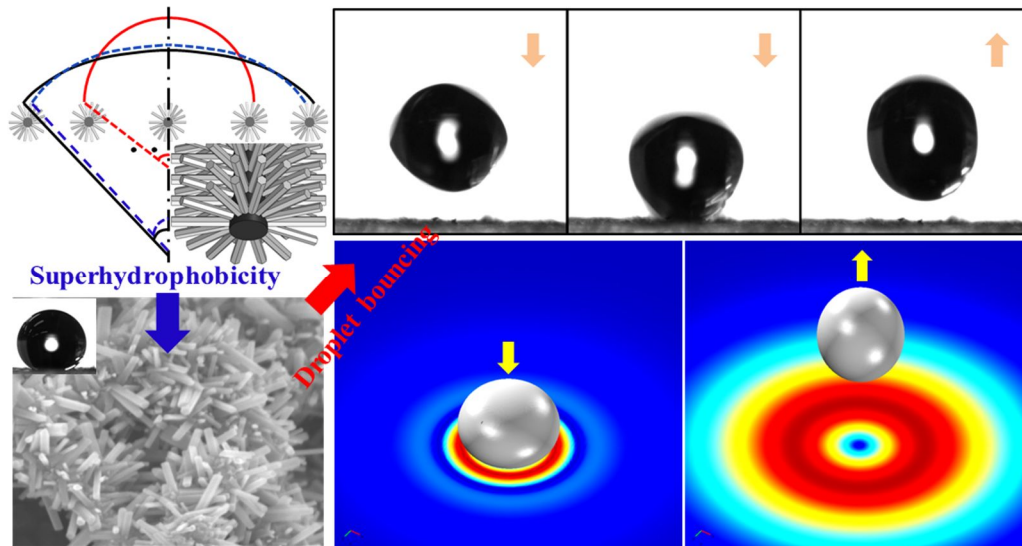


Figure 3.11. Schematics of Superhydrophobicity and water droplet bouncing phenomena caused by the surface free energy.

necessity of the multi-scale hierarchical structures for superhydrophobicity. In contrast to the single-scale structures, the prepared multi-scale hierarchical structures exhibited the bouncing phenomenon of a water droplet. To better understand such a phenomenon theoretically, FEB was analyzed and the FE simulation was carried out by using the level set method. As CA increases, the adhesion work, wettability, and energy dissipation of the droplet decrease. Consequently, the kinetic energy of the droplet can be converted into the surface deformation energy. Overall, the multi-scale hierarchical structure is expected to serve as an indispensable platform to implement not only superhydrophobicity but also extreme water repellency.

3.6. References

- [1] Marmur A. Wetting on hydrophobic rough surfaces: To be heterogeneous or not to be? *Langmuir*. 2003;19:8343-8.
- [2] Li HJ, Wang XB, Song YL, Liu YQ, Li QS, Jiang L, et al. Super-"amphiphobic" aligned carbon nanotube films. *Angew Chem Int Edit*. 2001;40:1743-6.
- [3] Feng L, Li SH, Li HJ, Zhai J, Song YL, Jiang L, et al. Super-hydrophobic surface of aligned polyacrylonitrile nanofibers. *Angew Chem Int Edit*. 2002;41:1221-3.
- [4] Hosono E, Fujihara S, Honma I, Zhou HS. Superhydrophobic perpendicular nanopin film by the bottom-up process. *J Am Chem Soc*. 2005;127:13458-9.
- [5] Li SH, Li HJ, Wang XB, Song YL, Liu YQ, Jiang L, et al. Super-hydrophobicity of large-area honeycomb-like aligned carbon nanotubes. *J Phys Chem B*. 2002;106:9274-6.
- [6] Gleiche M, Chi LF, Fuchs H. Nanoscopic channel lattices with controlled anisotropic wetting. *Nature*. 2000;403:173-5.
- [7] Sun MH, Luo CX, Xu LP, Ji H, Qi OY, Yu DP, et al. Artificial lotus leaf by nanocasting. *Langmuir*. 2005;21:8978-81.
- [8] Zhao N, Weng LH, Zhang XY, Xie QD, Zhang XL, Xu J. A lotus-leaf-like superhydrophobic surface prepared by solvent-induced crystallization. *Chemphyschem*.

2006;7:824-7.

[9] Zhai L, Cebeci FC, Cohen RE, Rubner MF. Stable superhydrophobic coatings from polyelectrolyte multilayers. *Nano Lett.* 2004;4:1349-53.

[10] Kim H, Noh K, Choi C, Khamwannah J, Villwock D, Jin S. Extreme Superomniphobicity of Multiwalled 8 nm TiO₂ Nanotubes. *Langmuir.* 2011;27:10191-6.

[11] Jiang L, Zhao Y, Zhai J. A lotus-leaf-like superhydrophobic surface: A porous microsphere/nanofiber composite film prepared by electrohydrodynamics. *Angew Chem Int Edit.* 2004;43:4338-41.

[12] Bhushan B, Jung YC, Niemietz A, Koch K. Lotus-Like Biomimetic Hierarchical Structures Developed by the Self-Assembly of Tubular Plant Waxes. *Langmuir.* 2009;25:1659-66.

[13] Bhushan B, Her EK. Fabrication of Superhydrophobic Surfaces with High and Low Adhesion Inspired from Rose Petal. *Langmuir.* 2010;26:8207-17.

[14] Sharma CS, Sharma A, Madou M. Multiscale Carbon Structures Fabricated by Direct Micropatterning of Electrospun Mats of SU-8 Photoresist Nanofibers. *Langmuir.* 2010;26:2218-22.

[15] Cui Z, Yin L, Wang QJ, Ding JF, Chen QM. A facile dip-coating process for preparing highly durable superhydrophobic surface with multi-scale structures on paint films. *J Colloid Interf Sci.* 2009;337:531-7.

[16] Karunakaran RG, Lu CH, Zhang ZH, Yang S. Highly Transparent Superhydrophobic Surfaces from the Coassembly of Nanoparticles. *Langmuir.* 2011;27:4594-602.

[17] Zhang L, Resasco DE. Single-Walled Carbon Nanotube Pillars: A Superhydrophobic Surface. *Langmuir.* 2009;25:4792-8.

[18] Liu HH, Zhang HY, Li W. Thermodynamic Analysis on Wetting Behavior of Hierarchical Structured Superhydrophobic Surfaces. *Langmuir.* 2011;27:6260-7.

[19] Nosonovsky M. Multiscale roughness and stability of superhydrophobic biomimetic interfaces. *Langmuir.* 2007;23:3157-61.

[20] Nosonovsky M, Bhushan B. Multiscale effects and capillary interactions in

functional biomimetic surfaces for energy conversion and green engineering. *Philos T R Soc A*. 2009;367:1511-39.

[21] Jung YC, Bhushan B. Dynamic effects of bouncing water droplets on superhydrophobic surfaces. *Langmuir*. 2008;24:6262-9.

[22] Jung YC, Bhushan B. Dynamic Effects Induced Transition of Droplets on Biomimetic Superhydrophobic Surfaces. *Langmuir*. 2009;25:9208-18.

[23] Nosonovsky M, Bhushan B. *Multiscale Dissipative Mechanisms and Hierarchical Surfaces*: Springer; 2008.

[24] Feng L, Li SH, Li YS, Li HJ, Zhang LJ, Zhai J, et al. Super-hydrophobic surfaces: From natural to artificial. *Adv Mater*. 2002;14:1857-60.

[25] Luo C, Zuo XL, Wang L, Wang EG, Song SP, Wang J, et al. Flexible Carbon Nanotube-Polymer Composite Films with High Conductivity and Superhydrophobicity Made by Solution Process. *Nano Lett*. 2008;8:4454-8.

[26] Jeong HE, Lee SH, Kim JK, Suh KY. Nanoengineered multiscale hierarchical structures with tailored wetting properties. *Langmuir*. 2006;22:1640-5.

[27] Li W, Amirfazli A. A thermodynamic approach for determining the contact angle hysteresis for superhydrophobic surfaces. *J Colloid Interf Sci*. 2005;292:195-201.

[28] Wang SR, Zhang Y, Abidi N, Cabrales L. Wettability and Surface Free Energy of Graphene Films. *Langmuir*. 2009;25:11078-81.

[29] Han J, Gao W. Surface Wettability of Nanostructured Zinc Oxide Films. *J Electron Mater*. 2009;38:601-8.

[30] Reyssat M, Pepin A, Marty F, Chen Y, Quere D. Bouncing transitions on microtextured materials. *Europhys Lett*. 2006;74:306-12.

[31] Okumura K, Chevy F, Richard D, Quere D, Clanet C. Water spring: A model for bouncing drops. *Europhys Lett*. 2003;62:237-43.

[32] Bartolo D, Bouamrine F, Verneuil E, Buguin A, Silberzan P, Moulinet S. Bouncing or sticky droplets: Impalement transitions on superhydrophobic micropatterned surfaces. *Europhys Lett*. 2006;74:299-305.

[33] Richard D, Quere D. Bouncing water drops. *Europhys Lett*. 2000;50:769-75.

[34] Lee DJ, Cho KY, Jang S, Song YS, Youn JR. Liquid slip on a nanostructured

surface. Langmuir. 2012.

[35] Callies M, Quere D. On water repellency. Soft Matter. 2005;1:55-61.

[36] Vayssieres L. Growth of arrayed nanorods and nanowires of ZnO from aqueous solutions. Adv Mater. 2003;15:464-6.

IV. Multiplex Particle Focusing Phenomenon via the Dean-coupled Elasto-inertial Effect of Viscoelastic Fluid

4.1. Introduction

A microfluidic platform has recently emerged as an efficient tool for separating systems in biology and environmentalology such as purification of contaminated water, bifurcation of flow stream, and separation of biological particles, parasites and infected cells from blood. Microfluidic based separating systems have been shown to be very competitive and useful comparing to conventional methods since the systems use a little volume of samples on the order of microliters and require no expensive or complex apparatus, and have advantages in shorter analysis time, high sensitivity, portability, real-time analysis, and easy disposability.

The separation technique was firstly developed by using filtration [1-3], electrophoresis [4], dielectrophoresis [5], and hydrodynamic chromatography [6-8]. However, these methods work in batch mode rather than continuous flow mode and require precise injection of fluid volume, which are undesirable for fast analysis and detection. More cost effective and faster method is to use continuous flow under the hydrodynamic pressure generating a lateral displacement of suspended particles toward the transverse direction of the main flow. Two methods are present for the lateral displacement: active and passive methods. For the active methods ultrasound, centrifugation, gravitation, optical manipulation, and acoustic wave are normally used as a source to manipulate the particles. However, these methods require external field,

manipulating device, and integration technique into microchips. For the passive methods the formation of an equilibrium position by using hydrodynamics of the fluid in a confined channel is a classical approach for manipulating particle dynamics.

An emerging idea is to fully harness the intrinsic properties of fluid itself to control particles. Especially polymer solutions show distinct behaviors such as shear thinning, shear thickening, yield stress, and die swelling induced by the intrinsic properties of the solution. It was revealed that in a confined microchannel diluted polymer solution shows the first normal stress difference in a cross-section that affects the lateral displacement of particles [9, 10]. Interestingly blood is also one of the most common fluids with intrinsically viscoelastic properties since blood has a high hematocrit ratio in which full of red blood cells behave as viscoelastic fluids [11-13]. It has recently found that an algal cell itself releases viscoelastic substances under a specific condition. Therefore the investigation of intrinsic properties of employed fluids is essential for exploiting the study of biophysics.

When it comes to the lateral migration of particles via the viscoelastic fluids it is driven by the imbalance of the compressive nonlinear elastic force, which is described in terms of the first and second normal stress differences, $N_1(\dot{\gamma}) = \sigma_{xx} - \sigma_{yy}$ and $N_2(\dot{\gamma}) = \sigma_{yy} - \sigma_{zz}$. For Poiseuille flow, lateral particle migration is towards the center of the channel, resulting from the minimum shear rate [14]. The lateral migration speed of the suspended particle in a viscoelastic medium is described as follows [9].

$$V \sim -\frac{a^2}{6\pi\eta} \frac{\partial N_1}{\partial \dot{\gamma}} \frac{\partial \dot{\gamma}}{\partial y} \quad (1)$$

The channel length should be sufficiently long enough to make an equilibrium position based on the fact that the migration speed is mainly governed by the first normal stress difference. Yang *et al.* [10] have harnessed the viscoelastic focusing to separate two different sized polystyrene beads demonstrating the particle focusing is an account of the incorporation of the inertial force and elastic force. Furthermore, red blood cell separation from whole blood has been carried out using the “elasto-inertial effect” in

the viscoelastic fluid.

Dean vortices have been used in microfluidic systems primarily for applications in fluid mixing. Ian *et al.* demonstrated that the dean drag force in a curved microchannel generates favored equilibrium positions that larger particles occupy space near an inner microchannel wall and smaller particles near an outer wall. They used the relationship between the dean drag force and inertial lift force, F_L / F_D , in that the ratio depends on the particle size producing that large particles do not change their position and small particles move toward the outer wall due to increased drag force. However their system does not introduce any intrinsic properties of the fluid, meaning no elastic force is added, since a Newtonian fluid like deionized water was used as a medium.

We present a novel concept for the separation of particles using the incorporation of elasto-inertial effect and dean effect termed as “Dean-coupled Elasto-inertial effect”. The elastic force is induced by the nature of a viscoelastic medium and the dean drag force is contributed by the curved channel geometry. The cooperation of the two forces produces an extraordinary particle focusing region. Numerical analysis of viscoelastic fluid proceeds in order to explain theoretical background and a mechanism for the lateral migration which follows the relationship between the elastic and dean drag forces with respect to particle size.

4.2. Theoretical Background

4.2.1. Elasto-inertial Particle Focusing

Particle migration caused under Poiseuille flow was firstly observed by Segré and Silberberg in a macroscopic channel. Recently, researches for the particle manipulation are actively conducted with the aid of the development of microfluidics, which is deeply associated with inertial microfluidics in that the combination of shear-gradient lift force, F_{LW} , and wall-repulsion lift force, F_{LS} . The two main forces

generate an equilibrium position in a microchannel so that particles are focused in a certain position of a cross-section of the channel. The lift force was theoretically predicted as $F_L = f_L(Re, x/h) \cdot \rho U^2 a^4 / H^2$, such that particles are forced and migrated with the assistance of the migration velocity, Reynolds number, particle diameter, and channel dimensions. Due to this, particles are migrated to an annulus centered at a position of ~ 0.6 times in a circular pipe and focused to four faces in a square channel [15].

Additional force, such as the elastic force, can be introduced as viscoelastic fluid is used as a medium [14, 16-18]. The elasticity, inherently present in dilute polymer solutions, can yield particle focusing in the midplane of the channel. The particles have different spatial distribution depending on their size and rheological properties of the suspending medium. The primary nonlinear elastic force affecting the lateral migration is the first normal stress difference, $N_1 = \sigma_{xx} - \sigma_{yy}$, since the value of the first normal stress difference is normally much greater than the second normal stress difference [9, 10, 19]. The migration velocity of particles in a viscoelastic medium is equated as $V \sim -(a^2 / 6\pi\eta)(\partial N_1 / \partial \dot{\gamma})(\partial \dot{\gamma} / \partial y)$ by counterbalancing both of the elastic force, $F_e \sim a^3 (\partial N_1(\dot{\gamma}) / \partial y)$, and the Stokes drag force, $F_\eta = 6\pi\eta(\dot{\gamma})aV$ [9]. The magnitude of the elasticity is represented by using the Elasticity number, El , which is expressed as below [20].

$$El = \frac{Wi}{Re} = \frac{\lambda \eta_c (w+h)}{\rho w^2 h} \quad (2)$$

The first normal stress difference is associated with the Weissenberg number, $Wi = \lambda \dot{\gamma}_c$, which is zero when the fluid is purely viscous, meaning no elasticity, and increases with increasing fluid elasticity. Here, an Oldroyd-B model was used to simulate the elasticity of the fluid and the first normal stress difference was depicted with respect to the Weissenberg number. The results show that the lowest regions are

located at the center and four corners in a square channel which are the same results proposed by Yang *et al.*

4.2.2. Dean Flow Induced Particle Migration

In general fluid motion in a curved channel is different on account of the curvature of the channel comparing to the motion in a straight channel. The fluid within the curved channel should satisfy mass balance between inner-wall and outer-wall regions. This induces a pressure gradient in the radial direction which subsequently generates the formation of two counter rotating vortices at the channel. This secondary flow is characterized by the Dean number as follows:

$$De = Re_c \cdot \sqrt{\frac{D_h}{2 \cdot R}} \quad (3)$$

Where Re_c is the channel Reynolds number, D_h is the hydrodynamic channel height, and R is the radius of curvature of the spiral channel. De increases with increasing flow rate and with decreasing the radius of curvature. The special case for harnessing the dean flow effectively in a microchannel is fluid mixing [21]. The fluid mixing is primarily governed by molecular diffusion which is enhanced by the low Reynolds number and high Péclet number. Multivortex micromixing was achieved by simply introducing a curvature, change in width of microchannel, and synergistic combination of dean vortices and expansion vortices [22].

D. D. Carlo extensively investigated the mechanism of continuous inertial focusing, ordering and separating systems using a Newtonian fluid, in that the additional force

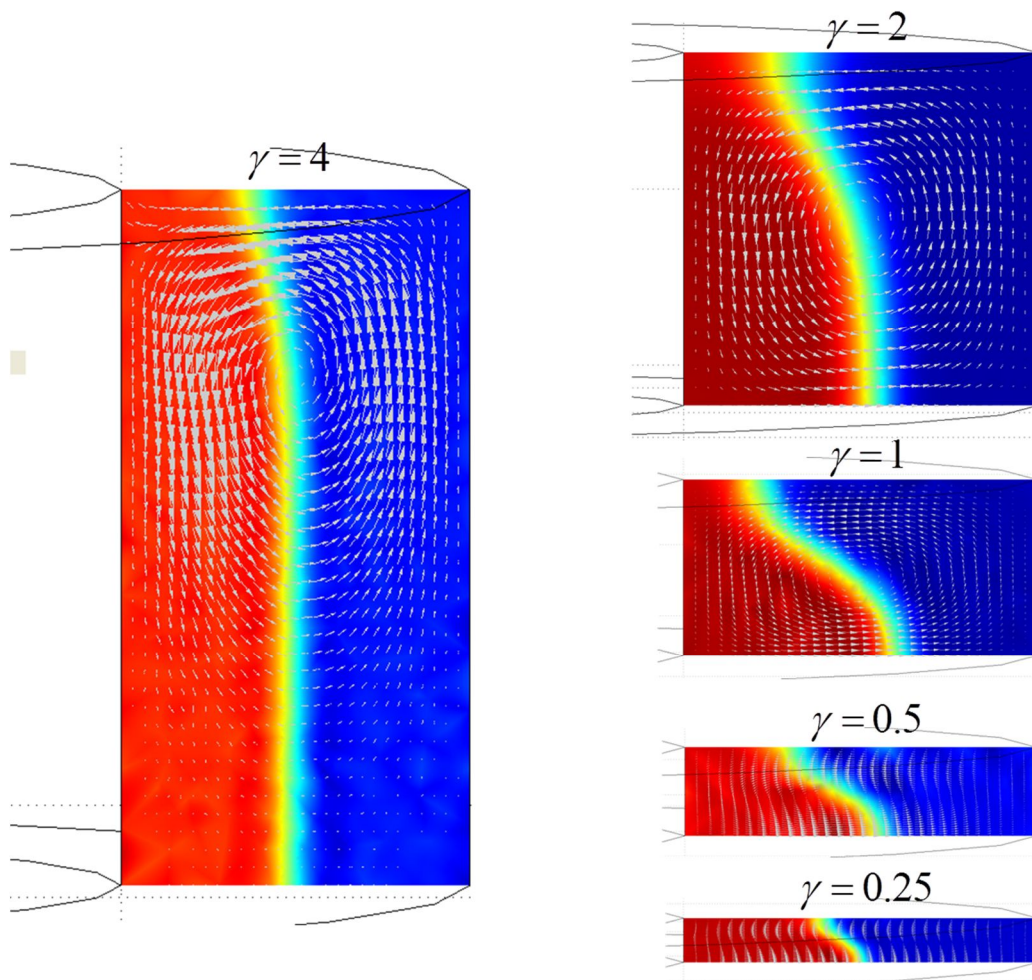


Figure 4.1. Dean flow and velocity profile with respect to channel aspect ratio in a curved spiral channel.

from dean flow does not create particle focusing, rather reduced the number of four equilibrium positions to two or one equilibrium positions [23]. The study presented the balance between the inertial lift force, F_Z , and the dean drag force, $F_D \sim \rho U_m^2 a D_h^2 r^{-1}$, which determines the preferred location of particles in a curved channel. The scaling law between F_Z and F_D determines a dominant focusing factor in the curved channel that as dean flow is dominant, meaning $F_D \gg F_Z$, there is no focusing, and focusing is favored as $F_Z \gg F_D$ so that inertial lift force alone will be observed as following the scaling law.

$$\frac{F_z}{F_D} \sim \frac{1}{\delta} \left(\frac{a}{D_h} \right)^3 R_c^n, \quad (n < 0) \quad (4)$$

In this equation the ratio of particle size and channel dimension, a/D_h , has a strong effect on determining the focusing behavior due to the third-power dependence so that small particles with large channel dimension would not be focused. Preferential focusing of particles can only be achieved when the particle and channel ratio (a_p/D_h) is larger than 0.07 [24-26]. And the dean drag force becomes more dominant with increasing channel Reynolds number, R_c therefore there is an upper limit on R_c above which all particle sizes will be defocused by the dean vortices.

4.2.3. Dean-coupled Elasto-inertial Particle Separation

The dean force assisted inertial microfluidics system demonstrates that the defocusing of particle occurs as increasing F_D and R_c by employing the equation 3. In our system one additional force called the elastic force, F_e , is introduced besides F_D and F_Z . This elastic force is proportional to the variation of the first normal stress difference and shows third-power dependency with the suspended particle size: $F_e \approx a^3 \nabla N_1$ [9, 27]. The elastic force is indeed an appealing method to focus particles at the center of the channel without any external forces and complex geometry,

however, small particles with $(a_p / D_h) \approx 0.04$ was not successfully focused due to not enough length of the straight microchannel [10]. The present spiral microchannel has approximately 50 cm of arc-length which is 10 to 25 times longer than the straight microchannel, which can generate the effective elastic force and dean drag force for sufficient particle migration regardless of the particle size, even under the particle size of $(a_p / D_h) < 0.02$. The combination of FD and Fe is shown in a curved spiral channel (Fig. 4.2). Typically the dean drag force operates within the channel creating secondary flows: counter-clockwise direction in an upper half cross-section and clockwise direction in a lower half cross-section. The elastic force due to the first normal stress difference also generates a centered equilibrium position [10, 20, 28]. The competition between F_D and Fe becomes a deterministic factor for the focusing position of particles. That is, the particles can be focused at the center when Fe becomes large, here when the PEO concentration becomes high. Furthermore as R_c is increasing F_D is also increasing according to the equation 3. Therefore the large Reynolds number and elasticity generate the particle focusing band termed as “Dean-coupled Elasto-Inertial Focusing Band”. The horizontal lateral migration of the particle becomes different because F_D is also different in regard to the particle size.

The Dean number is typically characterized by the channel Reynolds number, R_c , hydrodynamic diameter, and channel radius as equation 2. Another Reynolds number called as the particle Reynolds number is defined which includes parameters describing the perturbed channel flow due to suspended particles. The suspended particles also perturb the flow in a curved spiral channel so that the particle Dean number is defined as following.

$$De_p = Re_p \sqrt{D_h / 2R} = Re_c \left(\frac{a}{D_h} \right)^2 \left(\frac{D_h}{2R} \right)^{1/2} \quad (5)$$

Therefore the dean drag force becomes different with respect to particle diameters resulting in different lateral migration, which essentially manipulate particle focusing position.

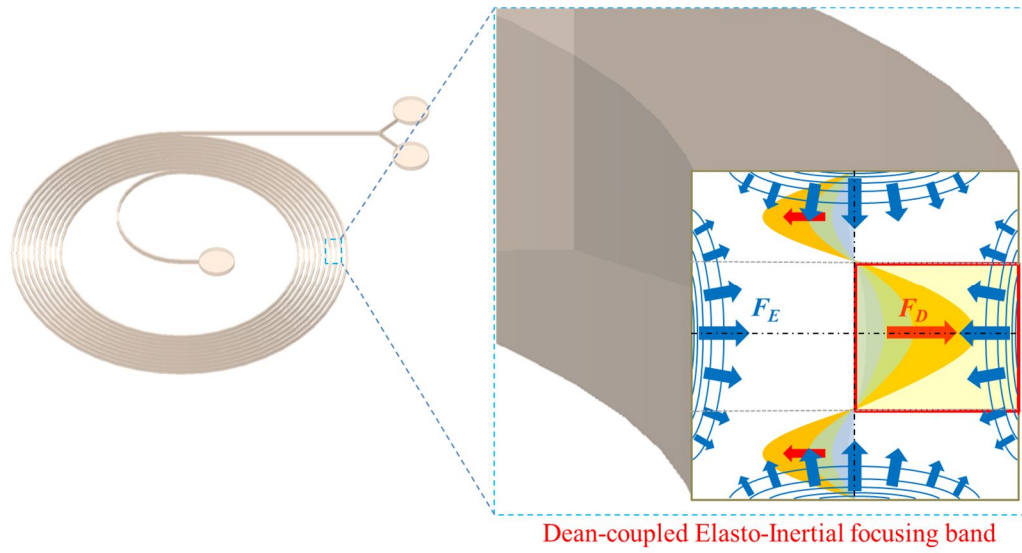


Figure 4.2. Schematic diagram of the “Dean-coupled Elasto-inertial focusing” proposed in this system.

Particle focusing via the viscoelastic medium in a microchannel was firstly observed by Leshansky *et al.* in which the system yielded particle focusing in the midplane of the shallow microfluidics channel with 45 μm height and 1000 μm width [9]. It is noted that the channel ratio is important to guarantee the midplane focusing of the particles not only to consider the elasticity induced midplane focusing but also to determine the particle focusing region due to the dean force. The narrow height facilitates the midplane particle focusing so that a spiral microchannel with 25 μm height and 100 μm width was employed in this experiment. Once the particles are focused in the midplane, horizontal migration of the particle is determined by the competition of F_D and F_E . The elasticity dominant fluid was successfully achieved by using polyethylene oxide (PEO) solution, $M_W = 2,000,000$ and 1000 ppm [10]. In this experiment PEO solution with $M_W = 1,000,000$ and 3000 ppm which guarantees enough elasticity for effective particle focusing is used.

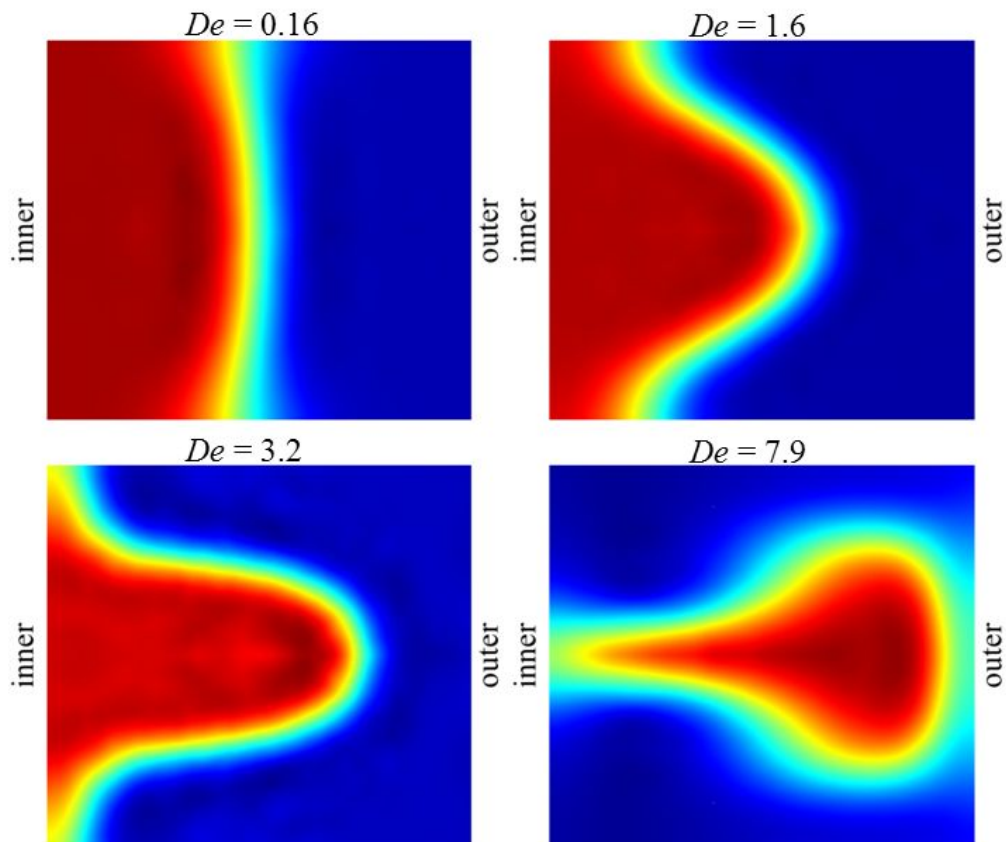


Figure 4.3. The effect of dean drag force with respect to the Dean number in a curved channel.

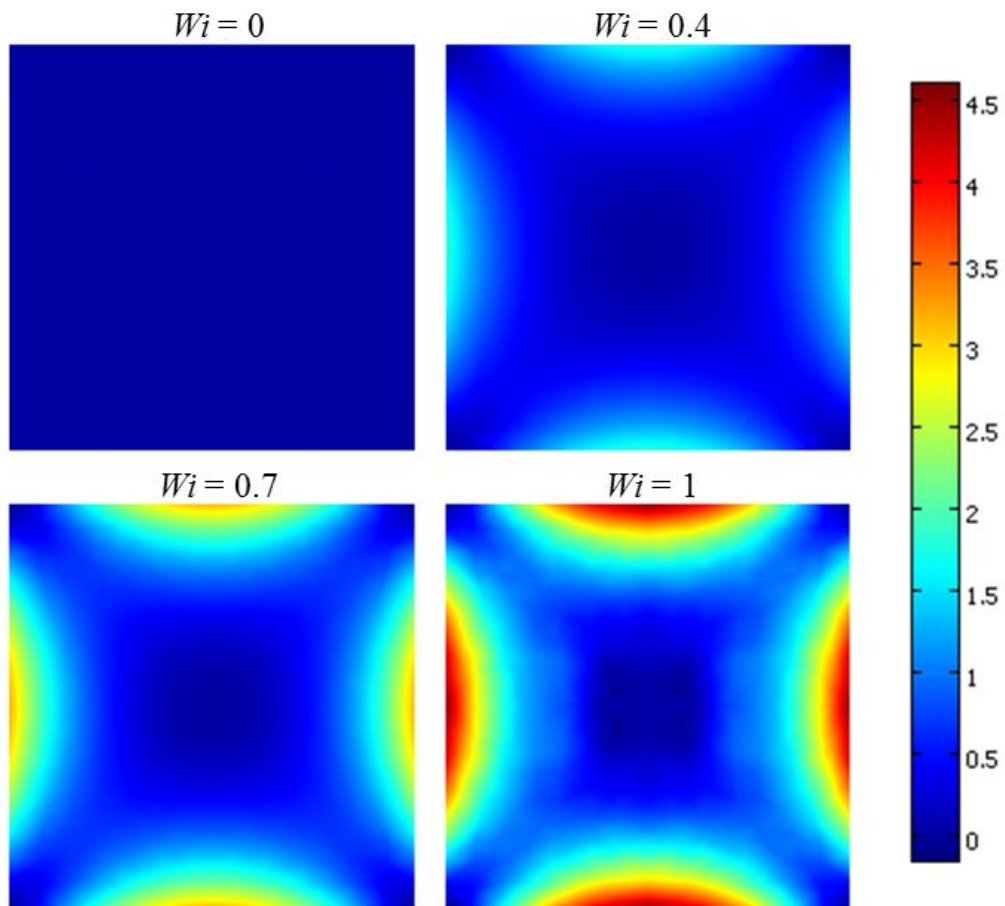


Figure 4.4. The first normal stress differences depending on the Weissenberg number in a square channel.

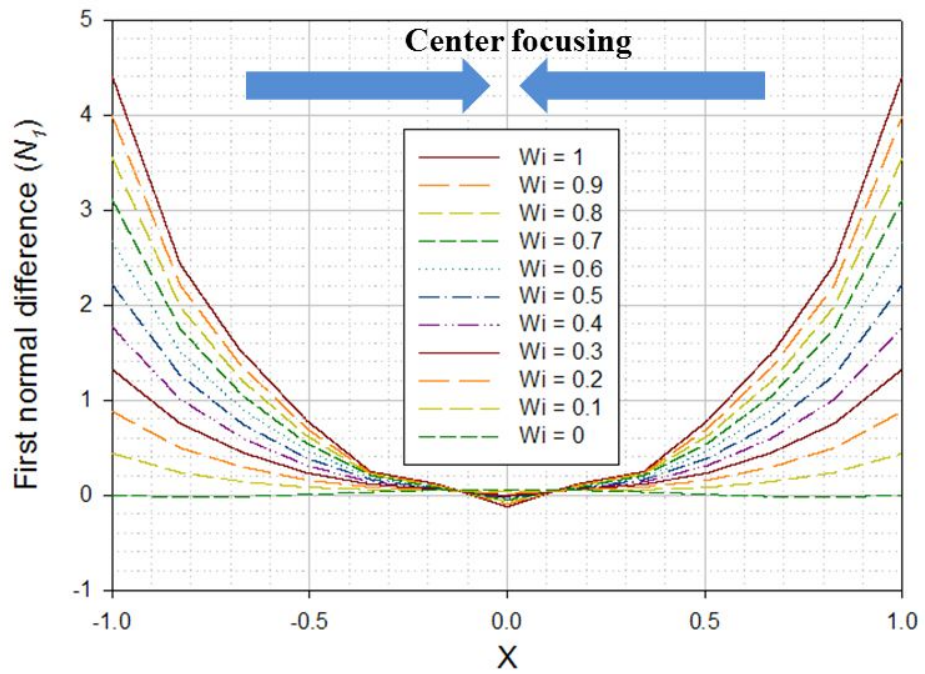


Figure 4.5. The distribution of the first normal stress difference with respect to the Weissenberg number along the horizontal direction in a square channel.

4.3. Results and Discussion

4.3.1. 3D Simulation Results of Elastic and Dean Forces

The two leading forces in a viscoelastic medium described by the Oldroyd-B model are simulated. For a square straight channel when the Weissenberg number is zero, meaning no elasticity, the first normal stress difference becomes zero (Fig. 4.4 and 4.5). The simulation results elucidate that the elasticity increases with increasing the Weissenberg number and eventually shows the lowest regions at the center and four corners. The symmetry of the first normal stress difference breaks as the channel becomes asymmetric like a curved spiral channel in our case. The system is nondimensionalized by using the Reynolds number, the Weissenberg number, and the total viscosity, $\eta = \eta_s + \eta_p$ (η_s :solvent viscosity, η_p :polymer viscosity) expressed as below:

$$\nabla \cdot u = 0 \quad (6)$$

$$Re(u \cdot \nabla)u = \nabla \cdot \left(-pI + (\eta_s / \eta) \left[\nabla u + (\nabla u)^T \right] + T \right) \quad (7)$$

$$T + Wi \left((u \cdot \nabla)T - \left[(\nabla u) \cdot T + T \cdot (\nabla u)^T \right] \right) = (\eta_p / \eta) \left[\nabla u + (\nabla u)^T \right] \quad (8)$$

The extra stress contribution follows the Oldroyd-B constitutive relation and the upper convective derivative operator as follow:

$$T + \lambda \overset{\nabla}{T} = 2\eta_p \dot{\gamma} \quad (9)$$

$$\overset{\nabla}{T} = \frac{\partial T}{\partial t} + (u \cdot \nabla)T - \left[(\nabla u) \cdot T + T \cdot (\nabla u)^T \right] \quad (10)$$

where λ and η_p determine the characteristics of the diluted polymer solution.

Using these governing and constitutive equations the viscoelastic fluid in a three dimensional curved spiral with an aspect ratio of 4:1 was simulated. It shows that high magnitude of the first normal stress difference appears near an inner wall in the spiral channel not like the four-fold symmetry in a straight channel (Fig. 4.6 and 4.7). The asymmetric force caused by the first normal stress difference leads the equilibrium position to be off-centered. Additionally the effect of De_p incurs that larger particles experience more lateral migration due to the increased dean drag force, whereas smaller particles show little lateral displacement (Fig. 4.3).

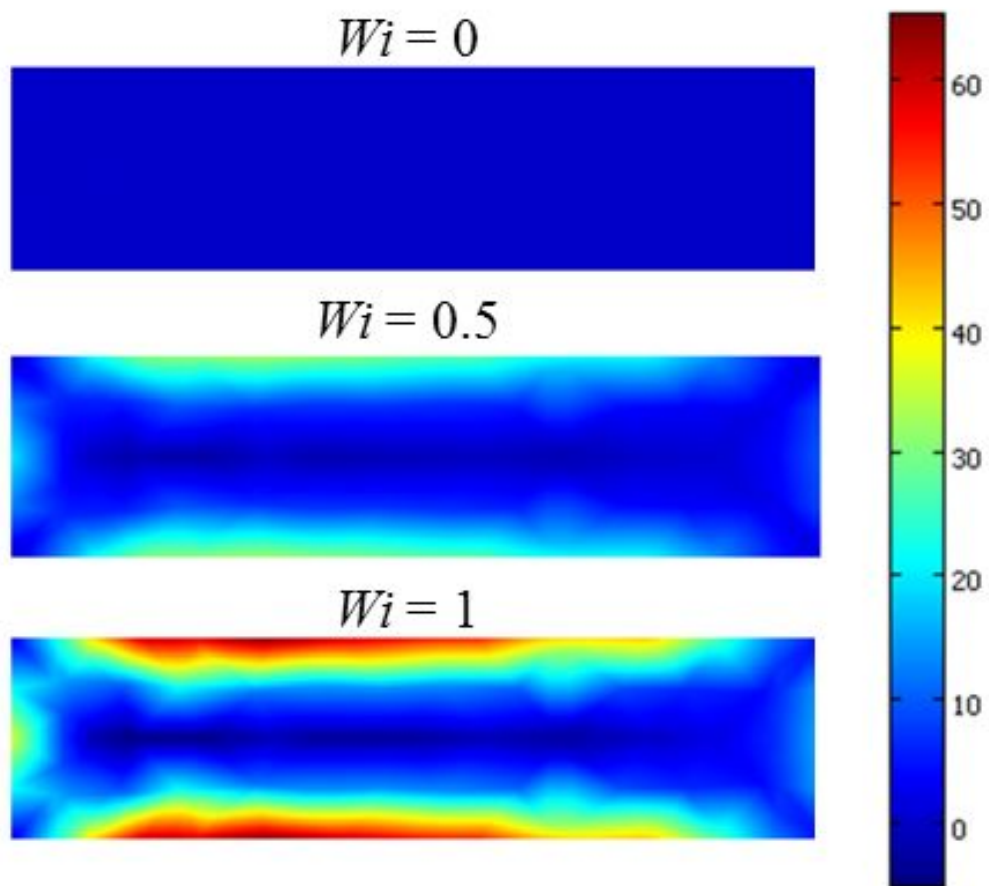


Figure 4.6. The first normal stress difference with respect to the Weissenberg number in a curved spiral channel.

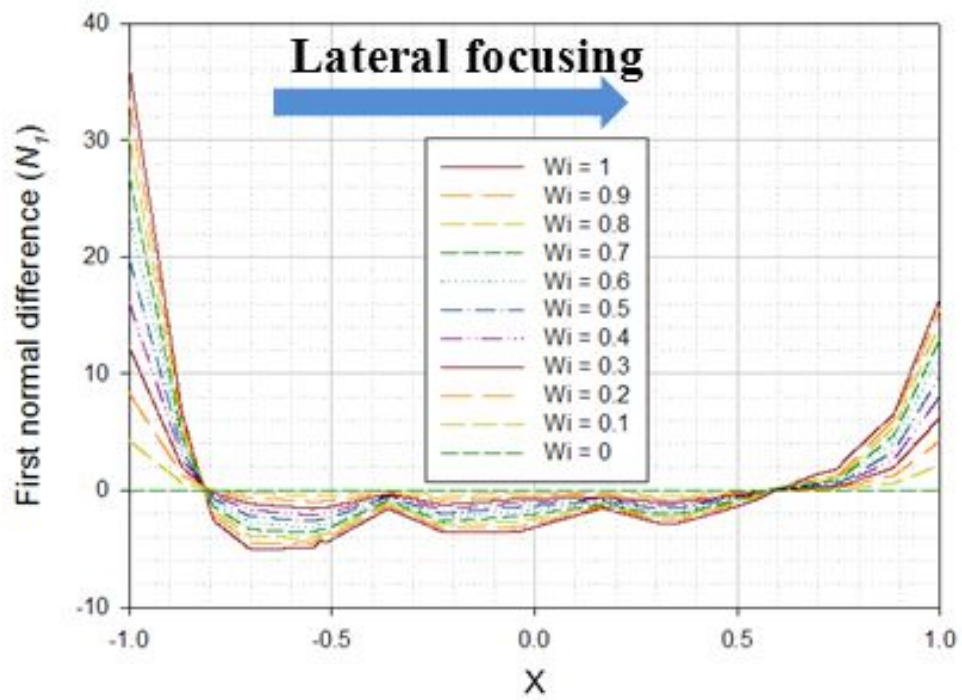


Figure 4.7. The distribution of the first normal stress difference with respect to the Weissenberg number along the horizontal direction in a curved spiral channel.

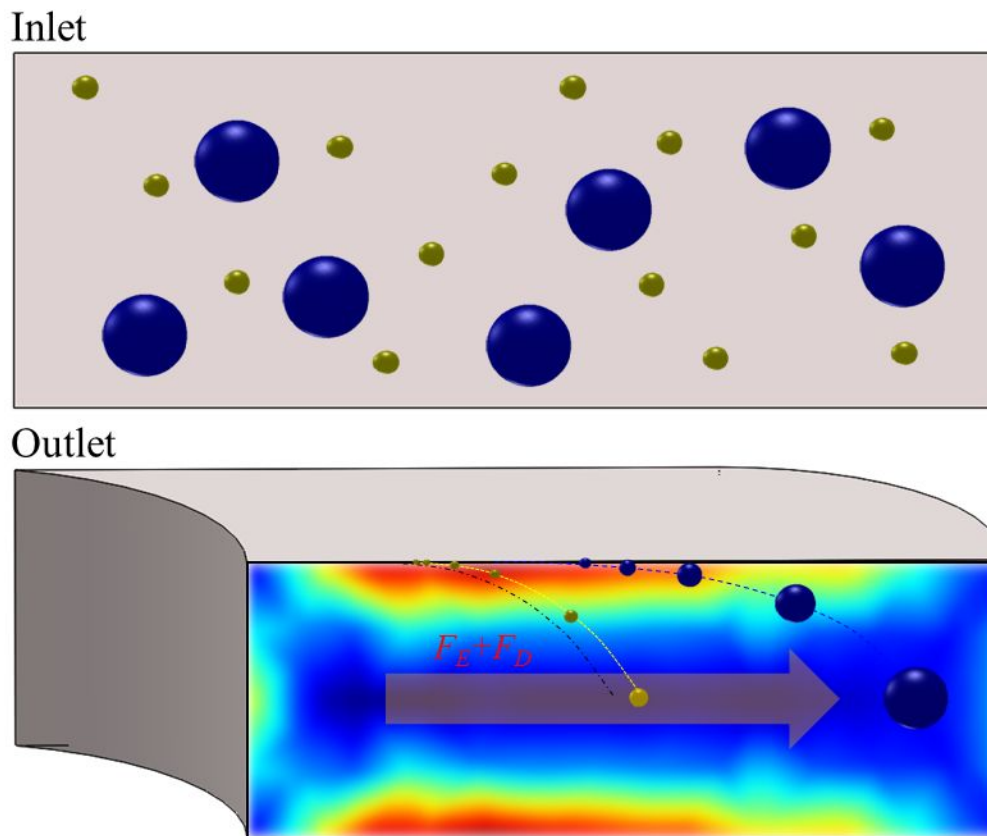


Figure 4.8. A schematic representation of size-dependent particle migration due to the competition of the dean drag force and the elastic force.

4.3.2. Continuous Single-line Particle Focusing

The first normal stress difference does not occur in a Newtonian medium since there is no elastic nature in the Newtonian fluid, thus only the dean drag force and inertial lift force arise. When the density of a particle is larger than the medium particles submerge so that larger particles can be collected in an outer wall and smaller particles collected in an inner wall with the aid of the characteristic velocity distribution on the cross-sectional plane normal to the main flow [29]. As the density of a particle is similar with the medium the ratio of forces F_Z / F_D is determining factor in which a particle of given size is a deterministic factor, which generate different equilibrium positions that larger particles has larger F_Z / F_D , inducing lateral migration towards the inner wall [24, 30]. However, this principle is only valid in some narrow cases where $a_p / H \geq 0.07$ so that no equilibrium position occurs when a particle size is much smaller than a microchannel or the balance of F_Z / F_D breaks the criterion. No particle focusing observed when a Newtonian fluid is used as a medium with the polystyrene particles of 1.5 μm , 5 μm , and 10 μm (Fig. 4.9). However, all particles were successfully focused with using a PEO viscoelastic medium and the larger particles go close to the outer wall. The extraordinary particle dynamics according to the particle size is associated with the combination of the elastic force inducing the midplane particle focusing and the dean drag force reducing the particle focusing region. That is, the combination of the F_D and F_E is essential to outperform the ability of particle focusing and separation.

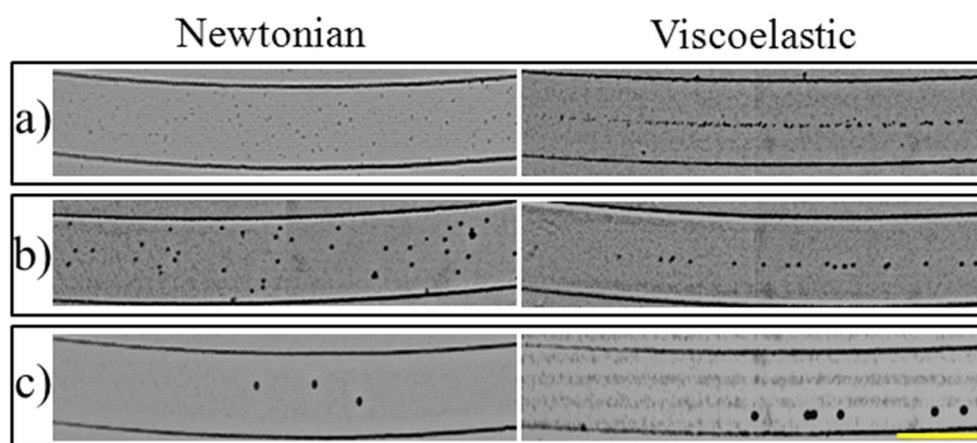


Figure 4.9. Particle dynamics in both of the Newtonian and viscoelastic fluids. The snapshots show the tenth turn of the spiral channel with (a) 1.5 μm PS, (b) 5 μm PS, and (c) 10 μm PS.

a)

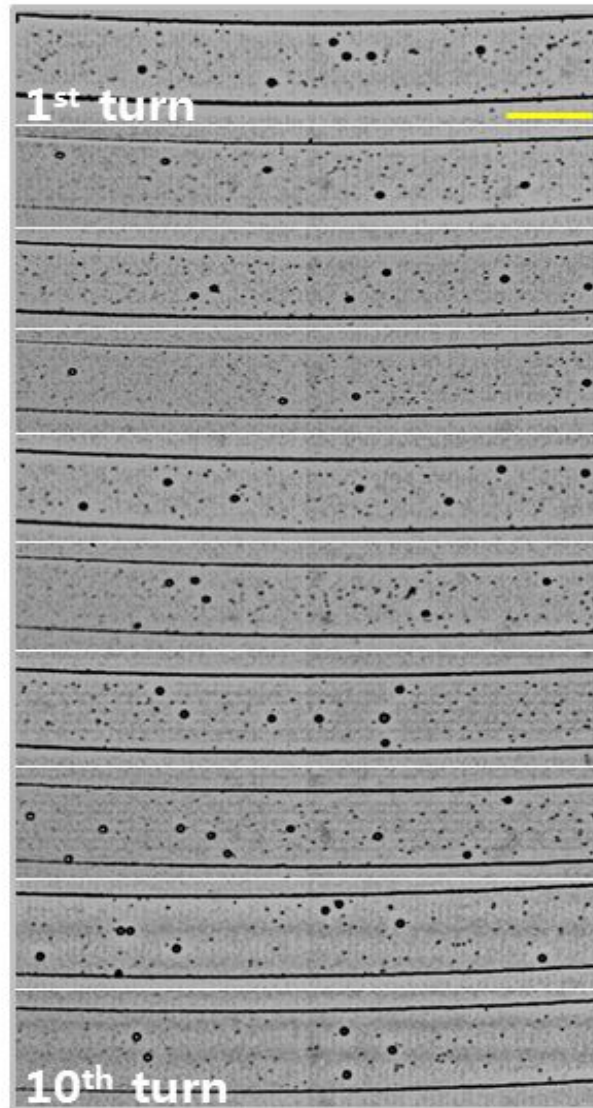


Figure 4.10. Particle migration with respect to the Newtonian and viscoelastic fluids: (a) No focusing of the particles, (b) probability distribution function of 1 μm PS, (c) 10 μm PS in the Newtonian fluid. (d) Focusing of the particles, (e) probability distribution function of 1 μm PS, and (f) 10 μm PS in the viscoelastic fluid.

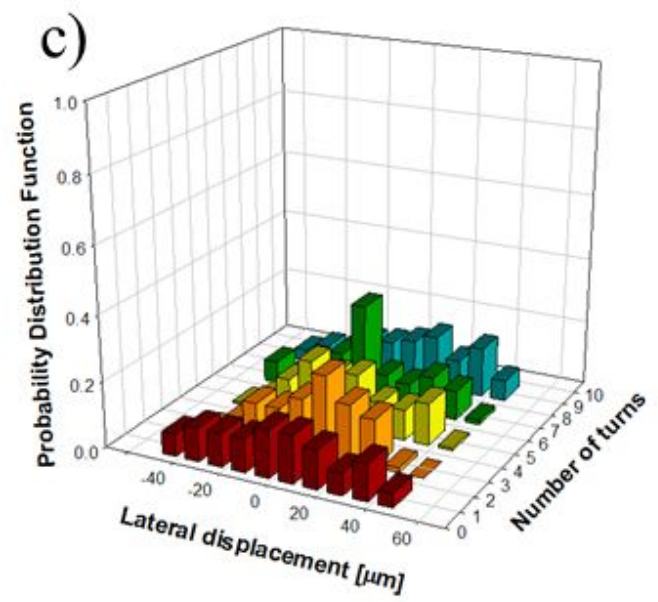
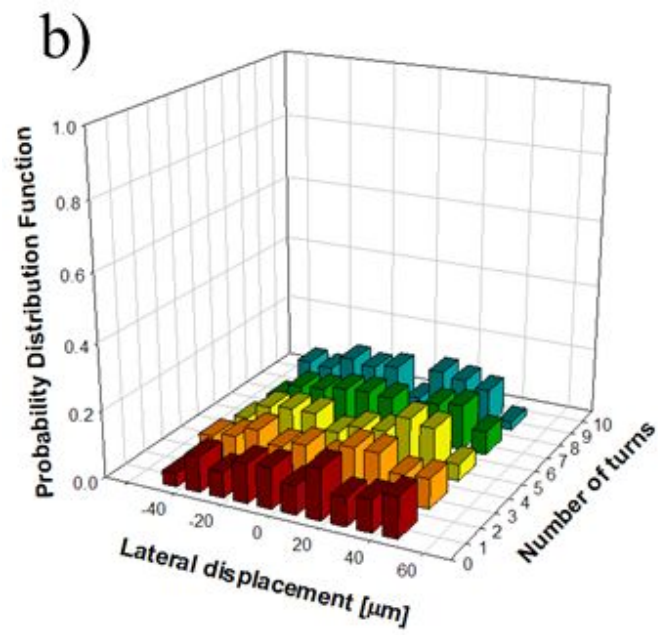


Figure 4.10. (Continued.)

d)

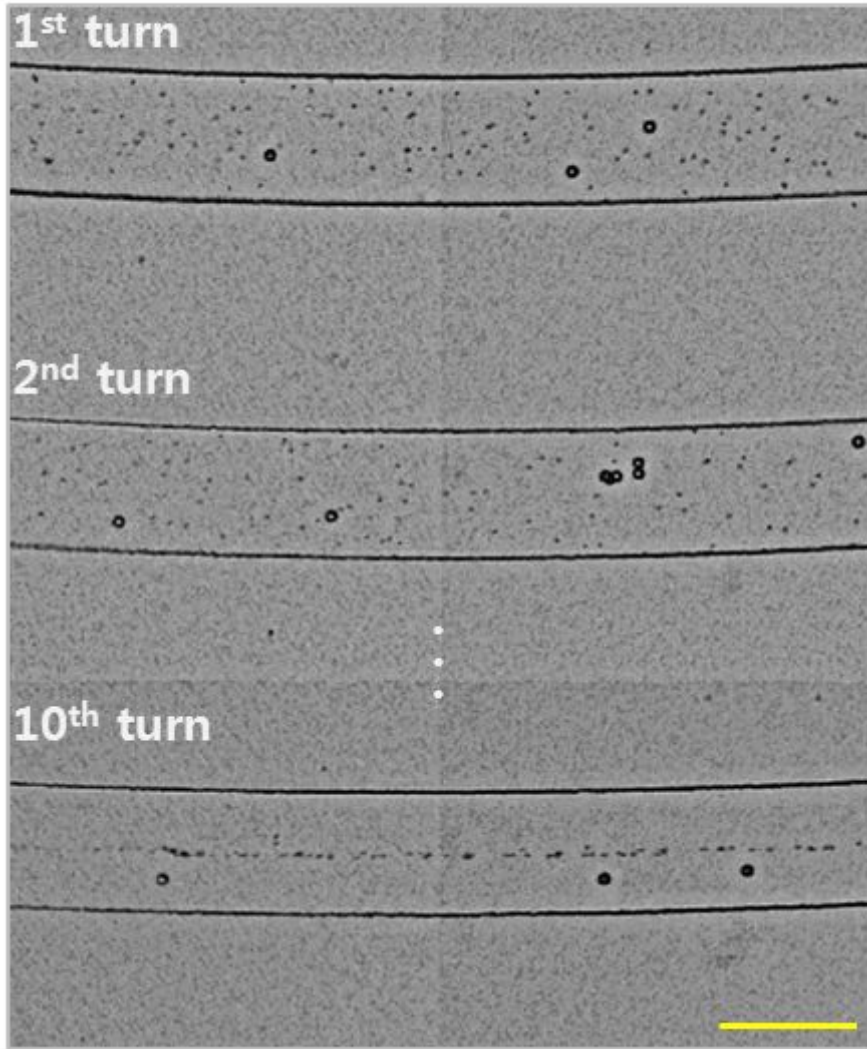


Figure 4.10. (Continued.)

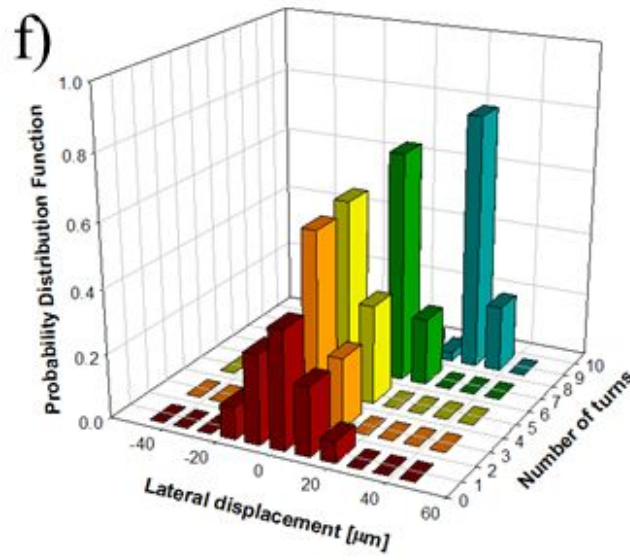
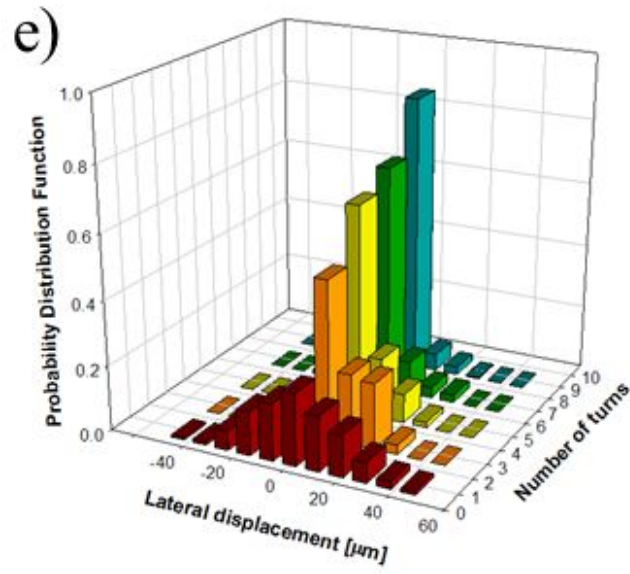


Figure 4.10. (Continued.)

4.3.3. Size-selective Multiplex Particle Focusing

It has been found that single-line particle focusing is successfully achieved by using a viscoelastic medium through the combination of F_D and F_E . We also examined the multiplex particle focusing using both of small and large particles with the diameters of 1.5 μm and 10 μm . It is generally expected that particle to particle interaction would be increased as particle concentration is increasing which in turn induces the perturbation of the flow and prohibits the particle focusing. Many cell and particle focusing microfluidic systems operate under the condition of dilute suspension, $\phi < 0.1\% \sim 0.2\%$, which holds the assumption that the particle to particle interaction is negligible. However the present system overcomes the diluteness condition. At an inlet both of small and large particles flow randomly and the randomness is still present at a second turn of the spiral channel. As the particles go through a tenth turn both particles have equilibrium positions showing 1.5 μm PS is at the center line and 10 μm is close to an outer wall (Fig. 4.10d~4.10f). It is worthy to note that both particles are not focused in a Newtonian medium even though the particles go through a tenth turn (Fig. 4.10a~4.10c). It becomes clear that the combination of F_D and F_E can play an important role for the separation of different sized particles simultaneously.

This system proposes an easy way to operate the microfluidic system without any external forces, but just by flowing the viscoelastic fluid in a curved spiral channel is enough to collect the different sized particles in different outlets. At an outlet the two particles are entrained parallel that both particles bifurcate to each side where 1.5 μm PS is collected at an upper outlet and 10 μm PS is collected at a lower outlet (Fig 4.11a~4.11d). There is no overlap of lateral displacement between 1.5 μm PS and 10 μm PS which guarantees high separating efficiency (Fig 4.11e). This mechanism will be very promising to separate each blood cell and plasma without expensive and complex apparatus since the average sizes of a platelet and red blood cell are 1 ~ 2 μm and 8 ~ 10 μm , respectively which are applicable to the present system. In a bid to separate the particles FBR in regard to various aspect ratios was introduced and the

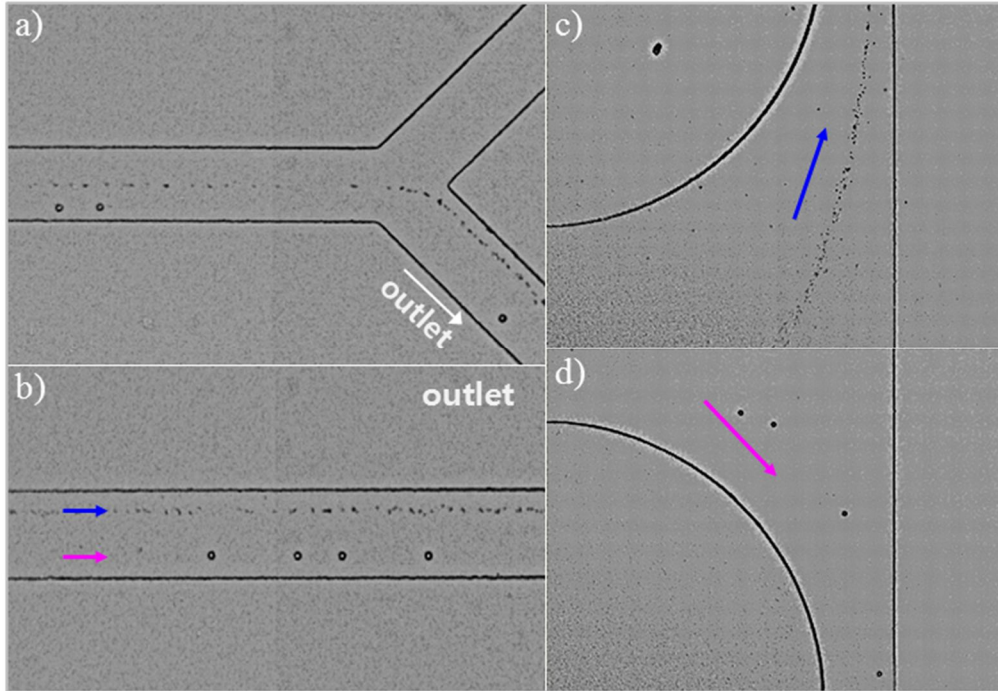


Figure 4.11. Size-selective multiplex particle focusing with the diameter of $1.5\ \mu\text{m}$ and $10\ \mu\text{m}$ Polystyrene particles: (a) parallel entrained particles at the bifurcation, (b) at an outlet, (c) at an upper outlet, (d) at a lower outlet, and (e) probability distribution function.

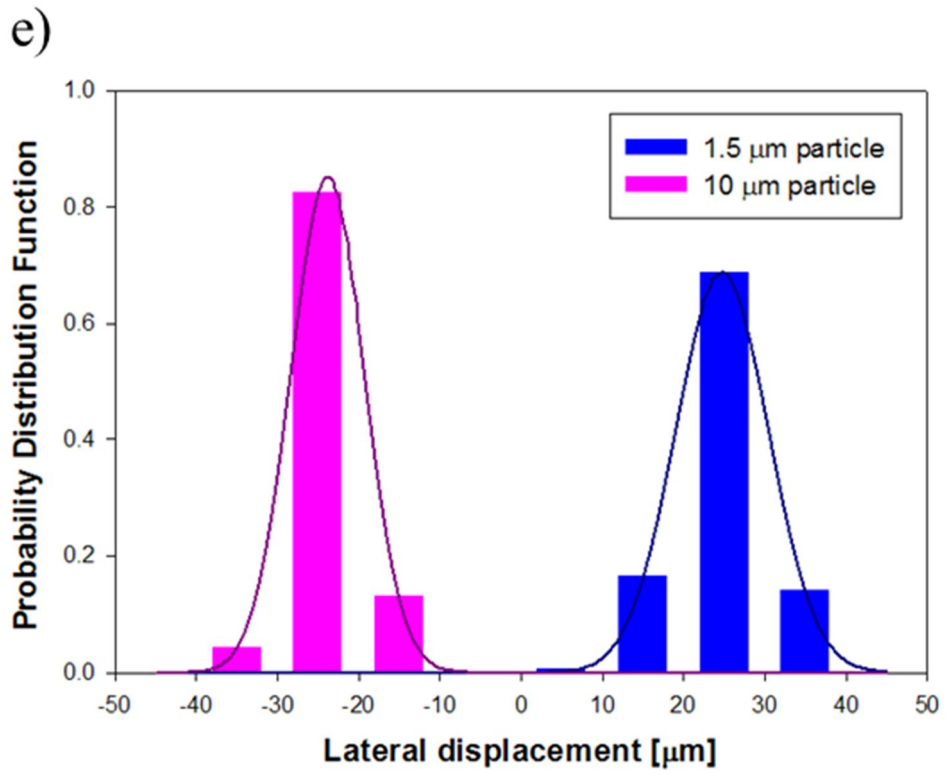


Figure 4.11. (Continued.)

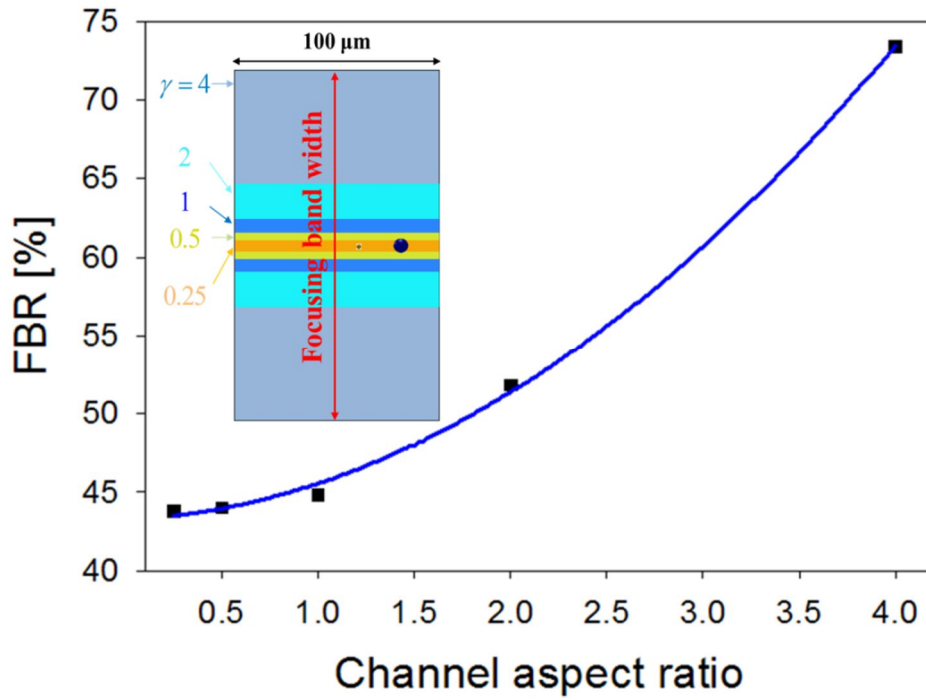


Figure 4.12. Focusing Band Ratio (FBR) with respect to the channel aspect ratio.

results show that particles were effectively focused in the midplane of the channel as the aspect ratio was below 0.5 in which the FBR is comparable to the suspended particle sizes. Typically the suspended particles in a confined channel move to not only horizontal direction but also vertical direction under the condition that the density of the particles is almost similar with the medium. Therefore, the aspect ratio of the microchannel should be suitably determined to fix the particles at the mid-plane of the cross-section. One example shows that as aspect ratio is increased the fluidic shear is modulated, resulting in preferential equilibrium positions of the particles. The enhanced shear-modulated inertial migration system is due to large lift forces generated through the high aspect ratio channels even at low Reynolds number. In our proposed system the elastic force compresses the suspended particles towards the mid-plane of the cross-section, resulting in narrow particle focusing band (FB) width. The FB is varied with the aspect ratio of the channel and Focusing Band Ratio (FBR) is introduced as follows:

$$\text{FBR} [\%] = \frac{\text{Band width}}{\text{Height}} \times 100 \quad (11)$$

Low FBR implies the particles are focused at the mid-plane of the channel that the particles can only move towards the horizontal direction which is advantageous to collect the particles with different lateral migrations by using the dean drag force. The FBR is decreased with decreasing the channel aspect ratio and it reaches the minimum values below the aspect ratio of 0.5. Therefore, our proposed system with the aspect ratio of 0.25 is good for focusing the suspended particle with the diameter of 1.5 μm and 10 μm PS. This implies that the microfluidic channel with a proper aspect ratio can improve the efficiency of particle focusing on the condition that the elastic force and the dean drag force is accordingly combined.

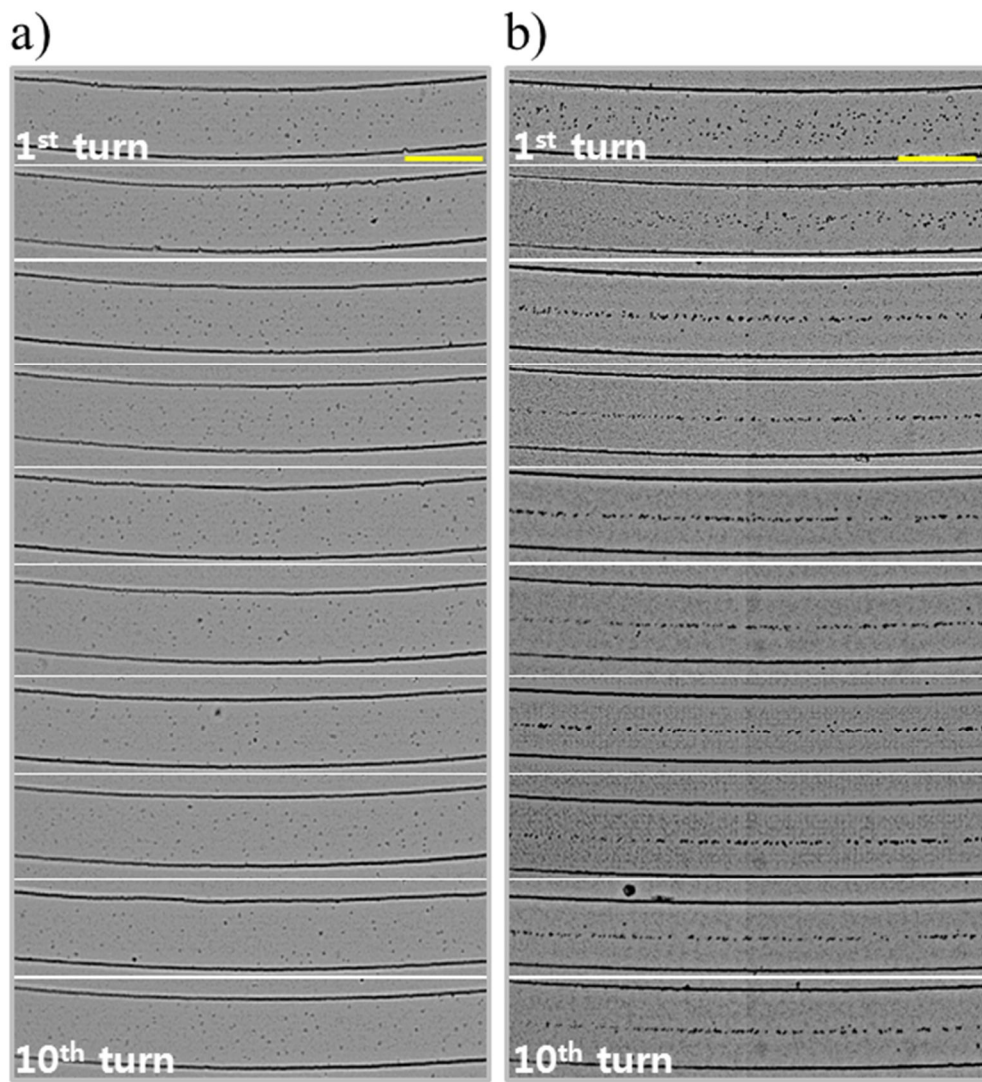


Figure 4.13. The behavior of particle migration with the diameter of 1.5 μm in the (a) Newtonian flow and (b) viscoelastic fluid.

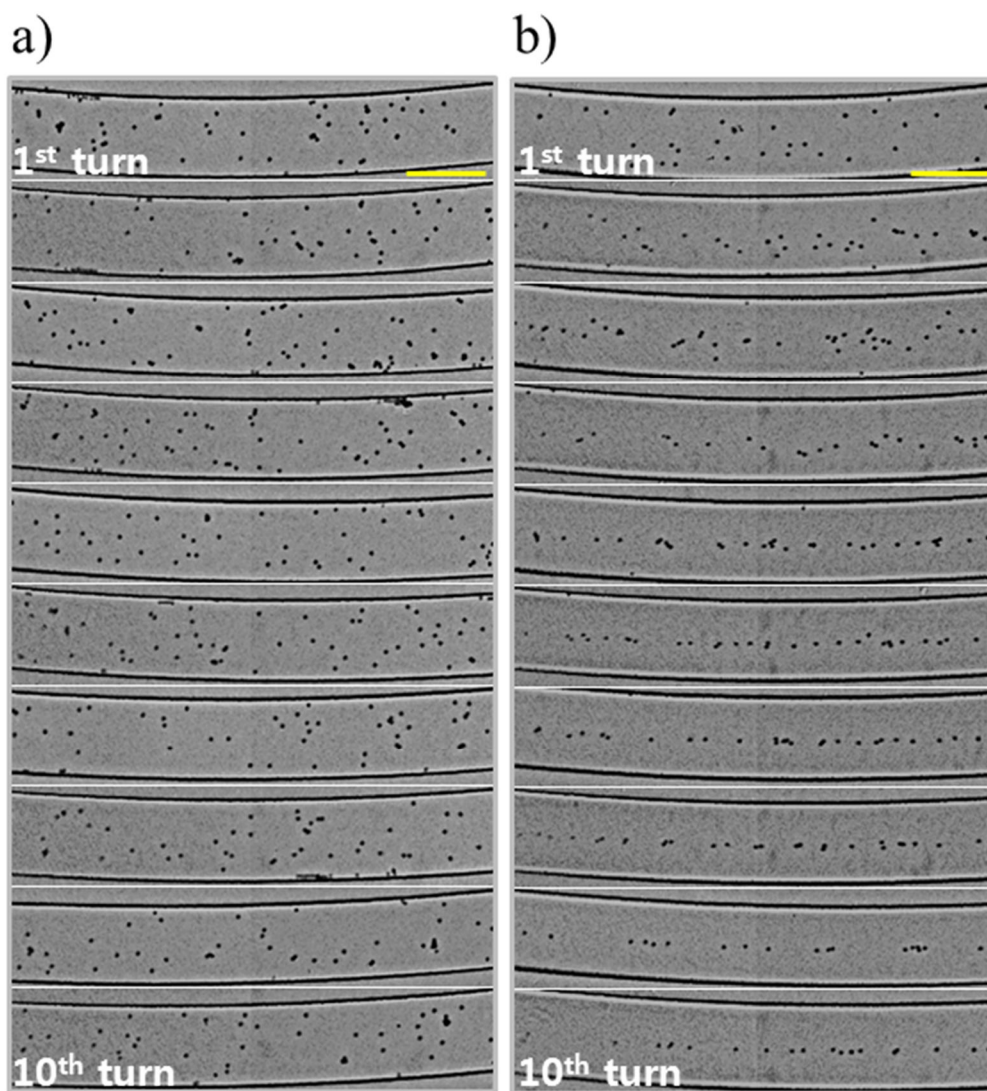


Figure 4.14. The behavior of particle migration with the diameter of 5 μm in the (a) Newtonian flow and (b) viscoelastic fluid.

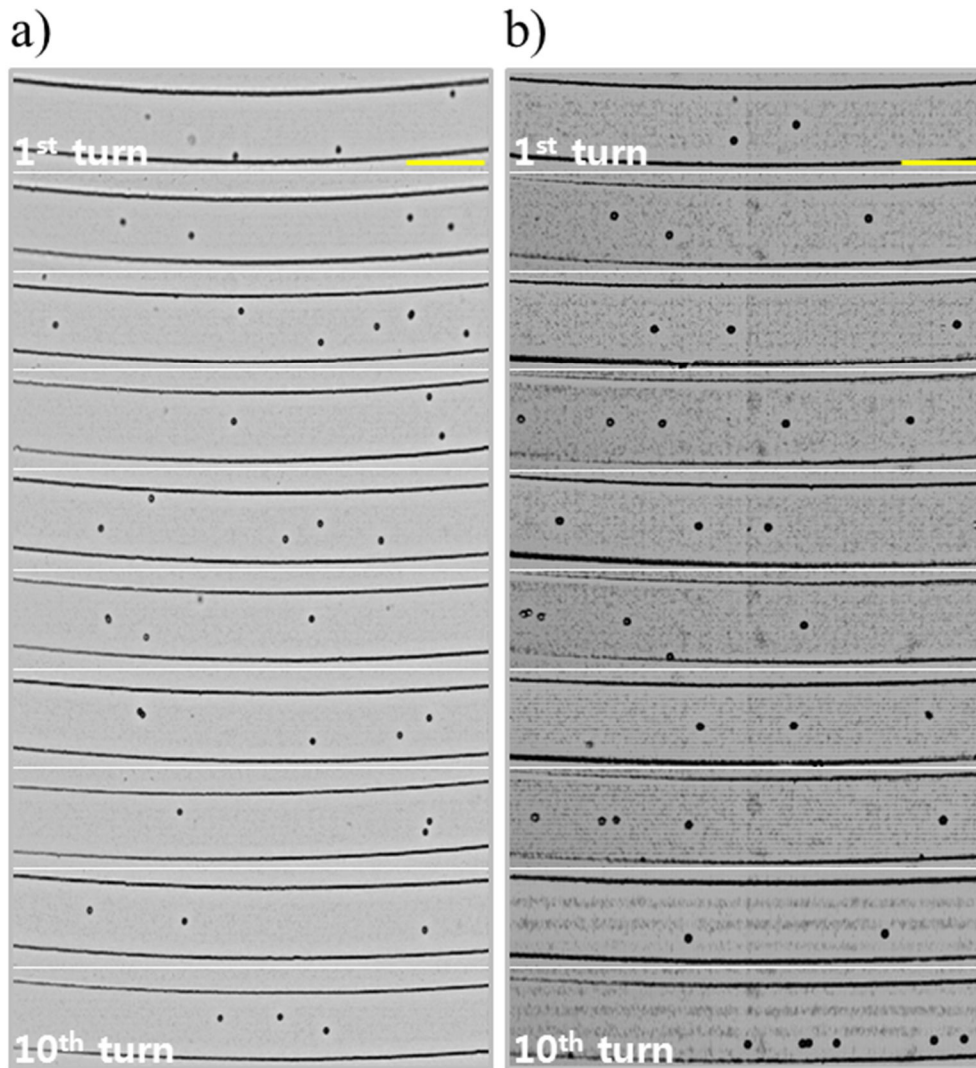


Figure 4.15. The behavior of particle migration with the diameter of 10 μm in the (a) Newtonian flow and (b) viscoelastic fluid.

4.3.4. Particle Migration with a Wall Slip System

A liquid wall-slip has been reported in microfluidic systems in which the characteristic length scales are on the order of micron and the flows are considered as laminar. The slip is typically developed by using geometric parameters of the fluidic channels. Textured hydrophobic surfaces affect liquid slip and the slip length increases with increasing the pitch of pillars on the channel. The textured surfaces can maintain a dewetted (Cassie) state so that water cannot penetrate into the pillars. We previously produced an *n-ZnO* assembled Cassie surface onto a glass substrate. However, it is difficult to produce Cassie surfaces inside the microchannel since the fabrication process cannot be handled with the simple photo- and soft-lithography. Nevertheless, it is worthy to understand the particle dynamics under the slip case because slip certainly happens in real microfluidic systems. Therefore, numerical simulation is investigated to consider the slip behavior inside the channel with the manipulation of boundary conditions of the channel wall. The geometric constitution is not realistically considered on the subdomain of a microchannel to represent the Cassie surface due to meshing and solving problem. To solve the realistic Cassie system two-phase flow consisting of air and liquid should be conducted with the nanostructured geometry. The boundary condition of the channel walls is changed according to the value of slip length as an alternative way.

It is interesting particles are focused at the center and four corners of the channel on account of the first normal stress differences. The velocity field shows that secondary flow happens as viscoelastic fluid is used as a medium (Figure 4.16). As partial slip is applied at the upper wall the fluid behavior becomes different. It is previously noted that slip length was 45 μm in a Couette flow of the microfluidic system. Therefore, the slip velocity was calculated by using the slip length assuming velocity profile is linearly increasing. The ratio of slip velocity and inlet velocity was 0.4. The results show that first normal stress difference becomes asymmetric due to the slip wall and the velocity profiles also changed. The focusing line is raised from the center and the particles are estimated to be focused at two upper corners and off-

centered upper region (Figure 4.17). As slip velocity becomes as large as the inlet velocity it shows more prominent asymmetry of the first normal stress difference. The velocity field shows that particles can be focused at the center region (Figure 4.18). This shows an extreme case because slip cannot be equal to the inlet velocity which presents a frictionless system. It is found that liquid slip affects the viscoelastic focusing of particles.

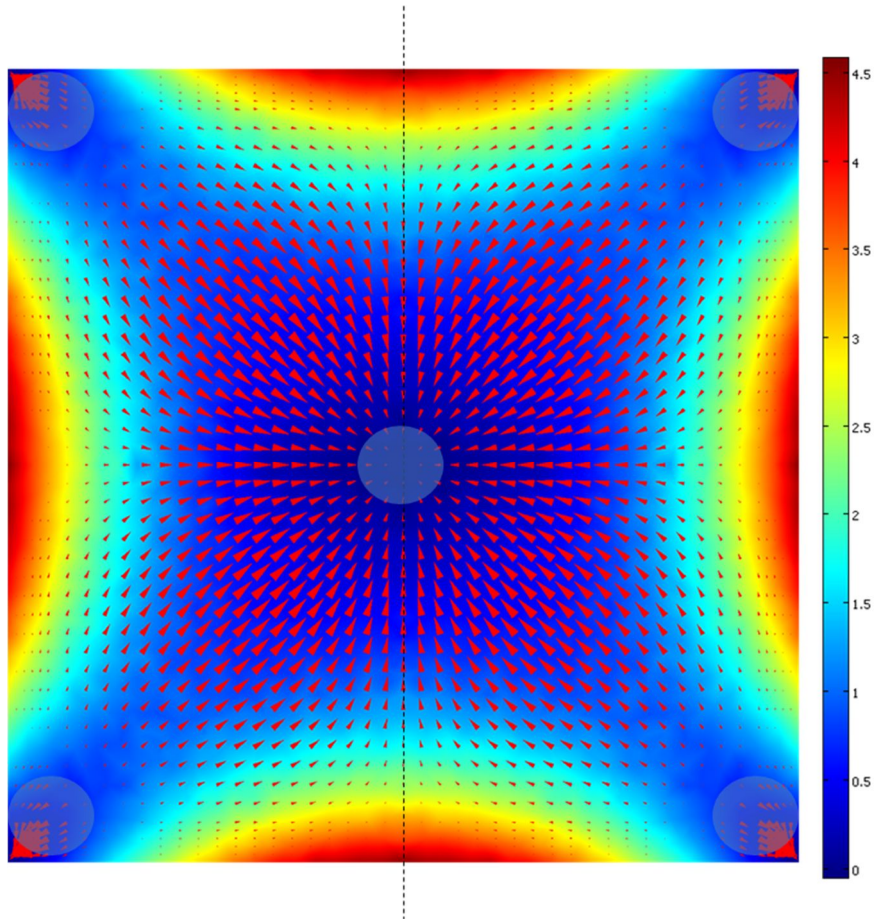


Figure 4.16. First normal stress difference and velocity field with estimated particle focusing regions under no-slip condition.

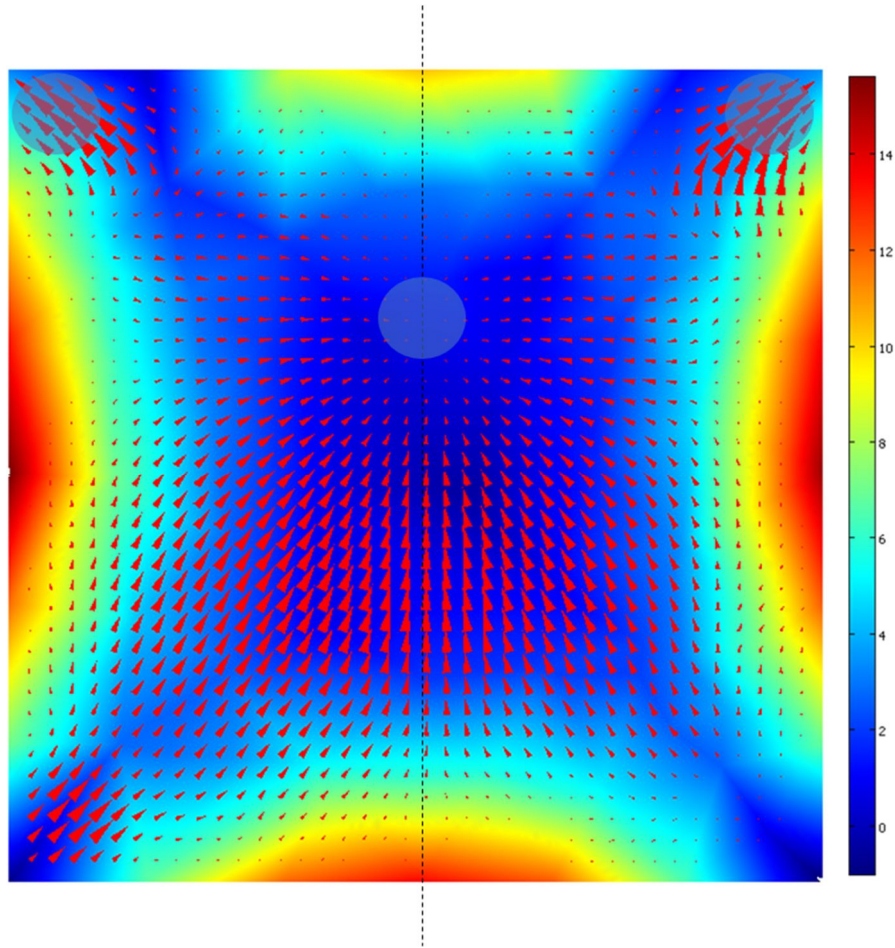


Figure 4.17. First normal stress difference and velocity field with estimated particle focusing regions under partial slip condition of $V_{slip}/V_{inlet} \sim 0.4$.

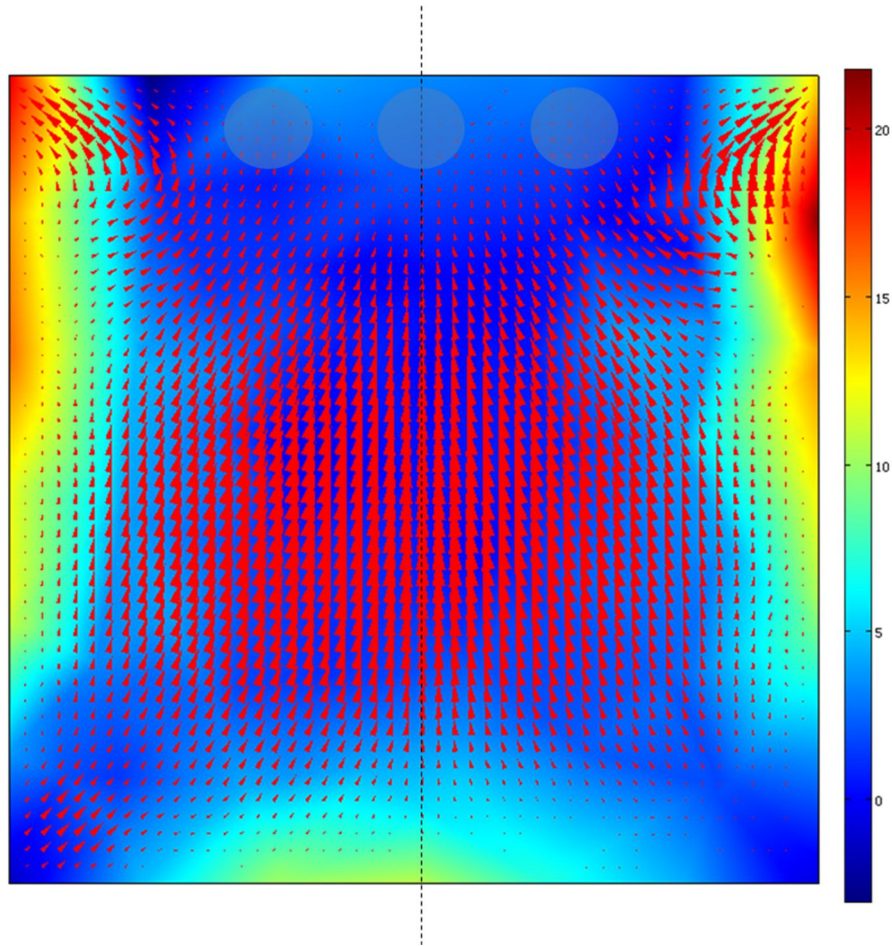


Figure 4.18. First normal stress difference and velocity field with estimated particle focusing regions under partial slip condition of $V_{slip}/V_{inlet} \sim 1$.

4.4. Summary

The particle separation was successfully achieved on account of the elastic force driven by the rheological properties of a viscoelastic medium and the dean drag force by a curved spiral microchannel. In a bid to separate the particles FBR in regard to various aspect ratios was introduced and the results show that particles were effectively focused in the midplane of the channel as the aspect ratio was below 0.5 in which the FBR is comparable to the suspended particle sizes. Furthermore the elastic force and the dean drag force are dependent on the particle size. That is, the competition of the elastic force and dean drag force determines size dependent particle separation. Therefore the two forces were numerically analyzed to explain the size dependent particle separation. As a particle size becomes large a particle tends to move at the center due to the increased elastic force, however, the dean drag force leads the particle to move toward an outer wall. The particle position is determined at the equilibrium position between the elastic force and dean drag force. Overall, the particle migration towards the outer wall in a focusing band is increased as the particle size becomes large since the increase in the dean drag force is greater than the increase in the elastic force. This system can produce size dependent multiplex particle focusing which is very promising technique for the separation of biological particles and bifurcation of flow stream.

4.5. References

- [1] Fuh CB, Giddings JC. Separation of submicron pharmaceutical emulsions with centrifugal split-flow thin (SPLITT) fractionation. *J Microcolumn Sep.* 1997;9:205-11.
- [2] Gale BK, Caldwell KD, Frazier AB. Geometric scaling effects in electrical field flow fractionation. 2. Experimental results. *Anal Chem.* 2002;74:1024-30.
- [3] Giddings JC. Field-Flow Fractionation - Analysis of Macromolecular, Colloidal, and Particulate Materials. *Science.* 1993;260:1456-65.

- [4] Hwang WM, Lee CY, Boo DW, Choi JG. Separation of nanoparticles in different sizes and compositions by capillary electrophoresis. *B Kor Chem Soc.* 2003;24:684-6.
- [5] Durr M, Kentsch J, Muller T, Schnelle T, Stelzle M. Microdevices for manipulation and accumulation of micro- and nanoparticles by dielectrophoresis. *Electrophoresis.* 2003;24:722-31.
- [6] Blom MT, Chmela E, Oosterbroek RE, Tijssen R, van den Berg A. On-chip hydrodynamic chromatography separation and detection of nanoparticles and biomolecules. *Anal Chem.* 2003;75:6761-8.
- [7] Giddings JC. Eddy Diffusion in Chromatography. *Nature.* 1959;184:357-8.
- [8] Guttman CM, Dimarzio EA. Separation by Flow .2. Application to Gel Permeation Chromatography. *Macromolecules.* 1970;3:681-&.
- [9] Leshansky AM, Bransky A, Korin N, Dinnar U. Tunable nonlinear viscoelastic "focusing" in a microfluidic device. *Phys Rev Lett.* 2007;98.
- [10] Yang S, Kim JY, Lee SJ, Lee SS, Kim JM. Sheathless elasto-inertial particle focusing and continuous separation in a straight rectangular microchannel. *Lab Chip.* 2011;11:266-73.
- [11] Chien S, King RG, Skalak R, Usami S, Copley AL. Viscoelastic Properties of Human-Blood and Red-Cell Suspensions. *Biorheology.* 1975;12:341-6.
- [12] Hur SC, Tse HTK, Di Carlo D. Sheathless inertial cell ordering for extreme throughput flow cytometry. *Lab Chip.* 2010;10:274-80.
- [13] Schneditz D, Rainer F, Kenner T. Viscoelastic Properties of Whole-Blood - Influence of Fast Sedimenting Red-Blood-Cell Aggregates. *Biorheology.* 1987;24:13-22.
- [14] Ho BP, Leal LG. Migration of Rigid Spheres in a 2-Dimensional Unidirectional Shear-Flow of a 2nd-Order Fluid. *J Fluid Mech.* 1976;7:783-99.
- [15] Di Carlo D. Inertial microfluidics. *Lab Chip.* 2009;9:3038-46.
- [16] Gan HY, Lam YC, Nguyen NT. Polymer-based device for efficient mixing of viscoelastic fluids. *Appl Phys Lett.* 2006;88.
- [17] Groisman A, Steinberg V. Elastic turbulence in a polymer solution flow. *Nature.* 2000;405:53-5.

- [18] Groisman A, Steinberg V. Efficient mixing at low Reynolds numbers using polymer additives. *Nature*. 2001;410:905-8.
- [19] Ho BP, Leal LG. Migration of Rigid Spheres in a 2-Dimensional Unidirectional Shear-Flow of a 2nd-Order Fluid. *J Fluid Mech*. 1976;76:783-99.
- [20] Nam J, Lim H, Kim D, Jung H, Shin S. Continuous separation of microparticles in a microfluidic channel via the elasto-inertial effect of non-Newtonian fluid. *Lab Chip*. 2012;12:1347-54.
- [21] Sudarsan AP, Ugaz VM. Fluid mixing in planar spiral microchannels. *Lab Chip*. 2006;6:74-82.
- [22] Sudarsan AP, Ugaz VM. Multivortex micromixing. *P Natl Acad Sci USA*. 2006;103:7228-33.
- [23] Di Carlo D, Irimia D, Tompkins RG, Toner M. Continuous inertial focusing, ordering, and separation of particles in microchannels. *P Natl Acad Sci USA*. 2007;104:18892-7.
- [24] Bhagat AAS, Kuntaegowdanahalli SS, Papautsky I. Continuous particle separation in spiral microchannels using dean flows and differential migration. *Lab Chip*. 2008;8:1906-14.
- [25] Bhagat AAS, Kuntaegowdanahalli SS, Kaval N, Seliskar CJ, Papautsky I. Inertial microfluidics for sheath-less high-throughput flow cytometry. *Biomed Microdevices*. 2010;12:187-95.
- [26] Di Carlo D, Edd JF, Humphry KJ, Stone HA, Toner M. Particle Segregation and Dynamics in Confined Flows. *Phys Rev Lett*. 2009;102.
- [27] Hur SC, Henderson-MacLennan NK, McCabe ERB, Di Carlo D. Deformability-based cell classification and enrichment using inertial microfluidics. *Lab Chip*. 2011;11:912-20.
- [28] Yang S, Lee SS, Ahn SW, Kang K, Shim W, Lee G, et al. Deformability-selective particle entrainment and separation in a rectangular microchannel using medium viscoelasticity. *Soft Matter*. 2012;8:5011-9.
- [29] Yoon DH, Ha JB, Bahk YK, Arakawa T, Shoji S, Go JS. Size-selective separation of micro beads by utilizing secondary flow in a curved rectangular microchannel. *Lab*

Chip. 2009;9:87-90.

[30] Kuntaegowdanahalli SS, Bhagat AAS, Kumar G, Papautsky I. Inertial microfluidics for continuous particle separation in spiral microchannels. Lab Chip. 2009;9:2973-80.

V. Concluding Remarks

This study provides comprehensive information for physical phenomena in a micro-scale system such as liquid slip, superhydrophobicity, and a focusing of confined particles. The extraordinary features of the three phenomena are closely connected with each other and are fully associated with the micro-tuning of fluids and surface structures. That is, superhydrophobicity on account of the micro-tuned surface geometry can induce large liquid slip, resulting in significant drag reduction in a microfluidic system which is very promising way to reduce driving forces of the system. An attractive idea comes from the fact that the particle focusing in a confined microchannel results from the balance of drag forces such as Stokes and Dean drag forces.

We argue that the micro/nano or multi-scaled surface structure is more advantageous than the manipulation of liquid-solid surface interaction in a bid to produce the superhydrophobicity and water repellency except the structure may be susceptible to external forces. Therefore, the influence of liquid-solid surface interaction and surface structure on liquid slip was investigated. The experimental results show that the nanostructure fabricated for the dewetted state had more effects on liquid slip than minimization of the liquid-solid surface interaction. It is obvious that the Cassie surface generated by the surface structure should be guaranteed for the large liquid slip and the molecular slip or nanobubbles generated by interaction minimization were not good enough to provoke the large liquid slip. The large liquid slip produces drag reduction which was found to be increased significantly as the characteristic length was scaled down to micro and nanoscale. The analytical models of linear and non-linear Navier slip in a present Couette flow system were proposed and the results show that liquid slip behavior is more obvious when increasing the non-linearity. It is worthy to note that the large liquid slip can be utilized to transform conventional micro- and nano-fluidic platforms into highly energy efficient devices with higher transport capability and less driving energy.

The nanostructured surfaces show the superhydrophobic nature and water droplet bouncing phenomenon as well as the large liquid slip since the dewetted Cassie condition for low receding free energy barrier is guaranteed. For the comparison of superhydrophobicity between single- and multi-scaled nanostructures, various single- and multi-scaled nanostructures are produced. Single nanoscale structures were constructed with CNT forest, CNF forest, and ZnO pillars. To increase the CA further up to the level of superhydrophobicity, multi-scale hierarchical structures were also prepared with CNT/ZnO and ZnO/CNF, and the resulting superhydrophobicity and dynamic effect (*i.e.*, bouncing effect) were analyzed. From the results we show that the multi-scale hierarchical structures produce superhydrophobicity with CA values higher than 160° by means of the synergistic interaction of the first-level and the second-level hierarchical structures. The thermodynamic approach was employed to understand and analyze the superhydrophobicity on the multi-scale hierarchical structures. It was also very interesting that in contrast to the single-scale structures, the multi-scale hierarchical structures exhibited the bouncing phenomenon of a water droplet. To better understand the water droplet bouncing theoretically, Free energy barrier was analyzed and the FE simulation was carried out by using the level set method. It was found that as CA increases, the adhesion work, wettability, and energy dissipation of the droplet decrease. Consequently, the kinetic energy of the droplet can be converted into the surface deformation energy. We are convinced that the multi-scale hierarchical structure is expected to serve as an indispensable platform to implement not only superhydrophobicity but also extreme water repellency.

The balance of forces in a confined microchannel is important to make an equilibrium position of a suspended particle. It was addressed the drag forces become influential as the system becomes small. Therefore, the forces exerted to the suspended particle need to be investigated. In this curved microfluidic channel particle separation was successfully achieved on account of the elastic force driven by the rheological properties of a viscoelastic medium and the dean drag force by a curved spiral microchannel.

In a bid to separate the particles the microchannels with various aspect ratios

were investigated and the Focusing Band Ratio (FBR) was proposed to understand the effective focusing of the particles in the midplane of the cross-section. And we figured out the elastic and dean drag forces are dependent on the particle size. That is, the competition of the elastic force and dean drag force determines size dependent particle separation. Therefore the two forces were numerically analyzed to explain the size dependent particle separation. As a particle size becomes large a particle tends to move at the center due to the increased elastic force, however, the dean drag force leads the particle to move toward an outer wall. The particle position is determined at the equilibrium position between the elastic force and dean drag force. Overall, the particle migration towards the outer wall in a focusing band is increased as the particle size becomes large since the increase in the dean drag force is greater than the increase in the elastic force. This system can produce size-selective multiplex particle focusing which is very promising technique for the separation of biological particles and bifurcation of flow stream.

We believe that the understanding of the features investigated here is very useful and valuable to explore undiscovered physical phenomena in a micro-scale platform yet.

Korean Abstract

본 연구에서는 미시(Micro-scale) 시스템에서 일어나는 유체 슬립 현상, 초소수성, 그리고 입자 포획 현상과 같은 물리적인 현상에 대한 이해를 다루고 있다. 이와 같은 세 가지의 특징적인 현상은 서로 밀접하게 연관을 이루고 있으며 시스템에서 이용하고 있는 미세 유체와 표면 특성에 기인한 것이다. 예를 들어, 초소수성은 표면의 마이크로나 나노 사이즈의 거칠기와 같은 형상에 의하여 발생하며 이는 유체 슬립 현상의 발생과 밀접한 연관이 있다. 또한 유체 슬립 현상은 마이크로 시스템에서 유체를 구동하는 힘을 획기적으로 낮출 수 있는 이점을 제공해 준다. 이와 같은 유체의 슬립 현상을 내비어(Navier) 슬립이라고 부른다. 유체의 슬립 현상은 유체와 고체 간의 물리화학적인 성질에 의하여 좌우된다. 따라서 본 연구에서는 유체의 슬립을 규명할 수 있는 나노 거칠기의 표면을 산화 아연을 이용한 자기 조립법을 통하여 제작하였다. 표면의 화학적 특성을 변화시킴으로써 유체의 슬립 현상에 영향을 크게 미치는 인자가 어떤 것인지에 대한 연구도 진행하였다. 그 결과, 나노 거칠기의 표면이 캐시(Cassie) 조건을 형성하게 되어 유체의 슬립에 더욱 큰 영향을 미치는 것을 알 수 있었으며 슬립 모델의 비선형도가 올라갈수록 슬립의 효과가 커지는 것을 알 수 있었다.

2장에서는 단일구조와 다중구조를 갖는 나노표면에서 발생하는 초소수성에 대한 효과가 연구되었다. 초소수성은 물방울이 표면에서 맺히지 않고 쉽게 떨어지는 특성이 있기 때문에 창문, 외장재, 도료 등의 분야에서 많이 연구되고 있다. 본 연구에서는 초소수성의 세 가지 특징인 높은 접촉각, 낮은 접촉각 히스테리시스, 그리고 물방울 튼 현상에 대하여 이론적으로 연구하였다. 단일구조와 다중구조의 나노표면을 만들기 위하여 탄소나노튜브와 탄소나노섬유 자체의 단일구조, 탄소나노튜브와 산화 아연, 그리고 탄소나노섬유와 산화아연이 혼합된 형태의 다중구조를 자기조립법을 이용하여 제작하였다. 그 결과 다중구조 나노표면에서는 160도가 넘는 높은 접촉각과 낮은 접촉각 히스테리시스가 나타나는 것을 알 수 있었다. 이는 나노

구조 사이에 존재하는 공기 층으로 인하여 캐시 조건이 형성되기 때문이다. 접촉각에 대한 이론적 연구를 위하여 열역학적 모델을 통한 자유 에너지와 자유 에너지 장벽 이론이 사용되었으며 물방울 튼 현상을 모사하기 위하여 유한요소법이 사용되었다. 다중구조의 나노표면에서는 높은 접촉각뿐만 아니라 낮은 자유 에너지 장벽이 존재함을 알 수 있었고 이는 나노표면에서의 초소수성 상태를 더욱 안정하게 만들기 때문에 물방울이 표면과 부딪힐 때 물방울 내의 역학적 에너지가 소산되지 않고 유지되어 물방울 튼 효과를 용이하게 만드는 결과를 보였다.

3장에서는 ‘탄성-관성 효과’와 함께 추가적으로 발생하는 딘(Dean) 효과를 고려하여 ‘딘 혼합(Dean-coupled) 탄성-관성 효과’라는 새로운 개념을 소개하였다. 층류 유동 하에서 점탄성 유체를 사용하게 되면 일반적으로 ‘탄성-관성 효과’가 발생하게 되며 이는 입자를 채널의 중앙으로 몰리게 한다. 본 연구에서는 굴곡을 갖는 나선형 마이크로채널을 제작하여 추가적인 이차 힘을 발생시켰으며 이를 이용하여 입자의 포획 및 분리를 시도하였다. 탄성 힘은 점탄성 물질 자체의 성질에 의존하는 것이고 딘 효과에 의한 이차 힘은 채널의 굴곡에 따른 것이므로 점탄성 물질과 채널 형상을 조절하면 ‘딘 혼합 탄성-관성 효과’에 의한 입자의 분리를 유도할 수 있다. 딘 효과 및 탄성 효과에 의한 힘을 비교하기 위하여 유한요소법을 사용하였으며 채널의 종횡비에 따른 힘의 변화를 연구하였다. 그 결과, 이 두 힘의 경쟁에 의하여 입자의 이동 거리가 다르게 발생하는 것을 알 수 있었다. 본 연구에서 제시한 플랫폼을 이용하면 입자의 크기에 따른 다중 포획 현상이 가능하며 이를 이용하여 크기가 다른 입자간 혹은 세포간 분리가 가능할 것으로 기대된다.

주요어; 유체 슬립, 나노구조, 캐시 표면, 초소수성, 초소수성 표면, 다중 구조 나노표면, 물방울 변형, 입자 포획, 마이크로플루이딕스, 관성 힘, 딥 힘, 입자 분리, 입자 이동, 점탄성 유체, 유한 요소 해석, 계면 효과

학번: 2009-30896